Dipl.-Ing. Gregor Plohl

Polymeric time scales for viscoelastic flow modelling

DOCTORAL THESIS

written to obtain the academic degree of a
Doctor of Engineering Sciences

Graz University of Technology

Supervisor
Univ.-Prof. Dr.-Ing. habil. Günter Brenn

Institute of Fluid Mechanics and Heat Transfer

Faculty of Mechanical Engineering and Economic Sciences

Graz, January 2019

Statutory Declaration

I declare that I have authored this thesis independently, that I have not used other than the declared sources/resources, and that I have explicitly marked all material which has been quoted either literally or by content from the used sources.

Graz, _____ _____

Date Signature

Eidesstattliche Erklärung[1]

Ich erkläre an Eides statt, dass ich die vorliegende Arbeit selbstständig verfasst, andere als die angegebenen Quellen/Hilfsmittel nicht benutzt, und die den benutzten Quellen wörtlich und inhaltlich entnommenen Stellen als solche kenntlich gemacht habe.

Graz, am _____ _____

Datum Unterschrift

[1] Beschluss der Curricula-Kommission für Bachelor-, Master- und Diplomstudien vom 10.11.2008; Genehmigung des Senates am 1.12.2008

Acknowledgement

The present thesis could not have been completed without the support of many important individuals. At this place I would like to offer my deepest regards and gratitude to all of them.
First and foremost, I would like to thank my doctoral supervisor Univ.-Prof. Dr.-Ing. habil. Günter Brenn. I am greatly thankful for his guidance, support and patience from the start to the end of my PhD study. With his great expertise and encouragement I was able to solve numerous problems faced in the course of the research.
Special thanks to Ao.Univ.-Prof. Dr.phil Volker Ribitsch for the invested time and for the fruitful discussions on my experimental results. His critical reading, the enriching comments and suggestions helped me to finalize the present thesis.
I thank all my colleagues at the Institute of Fluid Mechanics and Heat Transfer (ISW) for their help and support. I truly enjoyed to be a part of this institute. The experiments could not be successfully performed without the technical assistance of the team from the institute's workshop.
The rheological properties of the polymer test liquids were measured at the Institute of Chemistry of the University of Graz. Hereby, I would like to thank Ao.Univ.-Prof. Dr.phil Anton Huber for kindly allowing us to use their equipment, and Helga Reischl for her assistance during the experiments.

I would also like to thank my parents for their support throughout my education.

Finally, I would also like to thank my family; Petra, Zala and Lan. Their continuous love and support are my unlimited source of motivation, encouragement and inspiration. I dedicate this thesis to them.

Abstract

In the present thesis a method for measuring the deformation retardation time λ_2 of viscoelastic liquids is developed. The method is based on the oscillating drop technique. In this study small-amplitude damped shape oscillations of viscoelastic drops in air are considered. The underlying linear theory provides the characteristic equation of the drop from which λ_2 can be determined.

An acoustic levitation technique is used to levitate the individual drops. The drop shape oscillation of the fundamental mode $m = 2$ is excited by ultrasound modulation. Once the excitation is stopped, the drop exhibits damped oscillations which are recorded by a high-speed camera. From the acquired recordings the equilibrium drop radius and the complex angular frequency are determined.

Next, the numerical method for determining a pair of liquid properties - the unknown deformation retardation time λ_2 and any other known liquid property - from the complex characteristic equation is presented. In the present work the pairs (λ_2, η_0) and (λ_2, λ_1) were chosen, where η_0 is the zero-shear-rate viscosity and λ_1 is the stress relaxation time. The characteristic equation involves the spherical Bessel functions of the first kind which produce a manifold of solutions. From the set of solutions the correct pair is identified by comparison of the calculated values of η_0 or λ_1 with the results from measurements with a rotational viscometer (η_0^*) or the filament stretching elongational rheometer (λ_1^*), respectively.

The uncertainty analysis shows that the deformation retardation time λ_2 obtained by the proposed method depends weakly on uncertainties of the experiment. The measured values of λ_2 deviate strongly from the values often used in viscoelastic liquid flow simulations. It was found that for the liquids investigated the ratio λ_2/λ_1 assumes a fairly constant value.

Zusammenfassung

In der vorliegenden Dissertation wurde eine Methode zur Messung der Deformations-Retardationszeit λ_2 viskoelastischer Flüssigkeiten entwickelt. Die Methode basiert auf der Technik der schwingenden Tropfen. In dieser Studie werden gedämpfte Schwingungen kleiner Amplitude von viskoelastischen Tropfen betrachtet. Die zugrunde liegende lineare Theorie liefert die charakteristische Gleichung des Tropfens, aus der λ_2 bestimmt werden kann.
Eine akustische Levitationstechnik wird zur Positionierung einzelner Tropfen verwendet. Durch Ultraschall-Modulation wird die Tropfenschwingung des Grundmodes $m = 2$ angeregt. Wird diese Anregung gestoppt, so führt der Tropfen gedämpfte Schwingungen aus, die mit einer Hochgeschwindigkeits-Kamera aufgezeichnet werden. Aus den Bildern werden der Gleichgewichtsradius des Tropfens und die komplexe Kreisfrequenz der Schwingung bestimmt.
Dann wird die numerische Methode präsentiert, mit der aus der komplexen charakteristischen Gleichung ein Paar von Flüssigkeitseigenschaften bestimmt wird – die unbekannte Deformations-Retardationszeit λ_2 und eine andere bekannte Eigenschaft. In der vorliegenden Arbeit wurden die Paare (λ_2, η_0) und (λ_2, λ_1) gewählt, wobei η_0 die Viskosität bei sehr kleiner Scherrate und λ_1 die Spannungs-Relaxationszeit sind. Die charakteristische Gleichung enthält sphärische Besselfunktionen erster Art, die eine Vielfalt von Lösungen erzeugen. Aus der Menge der Lösungen wird das richtige Paar durch Vergleich der berechneten Werte η_0 oder λ_1 mit den Ergebnissen von Messungen mit einem Scherrheometer (η_0^*) und mit einem Filament-Dehnrheometer (λ_1^*) identifiziert.
Die Unsicherheits-Analyse zeigt, dass die Deformations-Retardationszeiten λ_2, die mittels der entwickelten Methode bestimmt werden, nur schwach von Unsicherheiten des Experiments abhängen. Die gemessenen Werte

λ_2 weichen stark von Werten ab, die oft in Simulationen viskoelastischer Strömungen benutzt werden. Es wurde gefunden, dass für die untersuchten Flüssigkeiten das Verhältnis λ_2/λ_1 einen nahezu konstanten Wert annimmt.

Contents

Nomenclature

Latin Symbols

A	fitted oscillation amplitude	[m]
a	equilibrium drop radius	[m]
a_m	initial oscillation amplitude of mode m	[m]
$\mathbf{B}$	Finger strain tensor	$[-]$
Bo	Bond number	$[-]$
$\mathbf{C}$	fourth order elasticity tensor	$[-]$
$\mathbf{D}$	strain rate tensor	$[\mathrm{s}^{-1}]$
De	Deborah number	$[-]$
De_1	relaxation Deborah number	$[-]$
De_2	retardation Deborah number	$[-]$
$\mathbf{E}$	deformation gradient tensor	$[-]$
$\boldsymbol{F}^s$	spring force	[N]
$\boldsymbol{F}^h$	hydrodynamic drag force	[N]
$\boldsymbol{F}^b$	Brownian force	[N]
$\boldsymbol{f}^{\mathrm{B}}$	body force per unit mass	$[\mathrm{m\,s}^{-2}]$

f	frequency	$[\mathrm{s}^{-1}]$
$G(t)$	linear relaxation modulus	$[\mathrm{N\,m}^{-2}]$
$G*$	complex modulus	$[\mathrm{N\,m}^{-2}]$
G'	storage modulus	$[\mathrm{N\,m}^{-2}]$
G''	loss modulus	$[\mathrm{N\,m}^{-2}]$
H	Hookean spring constant	$[\mathrm{N\,m}^{-1}]$
$H(\lambda)$	relaxation spectrum	$[\mathrm{N\,m}^{-2}]$
j_m	spherical Bessel function of the first kind of the order m	$[-]$
K_1	constant in Carreau model	[s]
k_B	Boltzman constant	$[\mathrm{N\,m\,K}^{-1}]$
$\mathbf{L}$	velocity gradient tensor	$[\mathrm{s}^{-1}]$
m	oscillation mode number	$[-]$
m_1	constant in Carreau model	$[-]$
$\boldsymbol{n}$	normal unit vector	$[-]$
n_0	constant in Carreau-Yassuda model	$[-]$
n_1	constant in Carreau-Yassuda model	$[-]$
Oh	Ohnesorge number	$[-]$
Oh^*	critical Ohnesorge number	$[-]$
P_m	Legendre polynomials	$[-]$
p	pressure	[Pa]

p_0	capillary pressure inside the undeformed drop	[Pa]
p_σ	capillary pressure inside the deformed drop	[Pa]
q	complex oscillatory length scale	[m^{-1}]
$\boldsymbol{R}$	end-to-end vector of a elastic dumbbell	[m]
R_1, R_2	radii of curvature	[m]
$\boldsymbol{r}_1$,$\boldsymbol{r}_2$	position vectors	[m]
r	radial coordinate	[m]
r_S	drop shape function	[m]
T	temperature	[K]
t	time	[s]
$\boldsymbol{u}$	velocity vector	[$\mathrm{m\,s}^{-1}$]
$\mathbf{W}$	vorticity tensor	[s^{-1}]
Wi	Weissenberg number	[$-$]
w	polymer mass fraction	[$-$]
$\boldsymbol{x}$	position vector	[m]
x_1, x_2, x_3	spatial coordinates	[m]
y_m	spherical Bessel function of the second kind of the order m	[$-$]

Greek symbols

α_m	complex angular frequency of mode m	[s^{-1}]
$\alpha_{m,0}$	Rayleigh angular frequency of mode m	[s^{-1}]

$\alpha_{m,i}$	angular frequency of mode m	$[\mathrm{s}^{-1}]$
$\alpha_{m,r}$	damping rate of mode m	$[\mathrm{s}^{-1}]$
$\dot{\boldsymbol{\gamma}}$	strain rate tensor	$[\mathrm{s}^{-1}]$
$\boldsymbol{\gamma}$	strain tensor	$[-]$
γ	deformation	$[-]$
$\boldsymbol{\delta}$	unit tensor	$[-]$
δ	Dirac delta function	$[-]$
ϵ_0	initial oscillation amplitude	$[\mathrm{m}]$
$\boldsymbol{\zeta}$	position vector	$[\mathrm{m}]$
ζ	drag coefficient	$[\mathrm{N\,s\,m}^{-1}]$
$\zeta_1, \zeta_2, \zeta_3$	material coordinates	$[\mathrm{m}]$
η	dynamic viscosity	$[\mathrm{N\,s\,m}^{-2}]$
η_0	zero-shear-rate dynamic viscosity	$[\mathrm{N\,s\,m}^{-2}]$
η_∞	infinite-shear-rate dynamic viscosity	$[\mathrm{N\,s\,m}^{-2}]$
η_p	polymer viscosity	$[\mathrm{N\,s\,m}^{-2}]$
η_s	solvent viscosity	$[\mathrm{N\,s\,m}^{-2}]$
θ	polar angle	$[\mathrm{rad}]$
λ	relaxation time	$[\mathrm{s}]$
λ_1	stress relaxation time	$[\mathrm{s}]$
λ_2	deformation retardation time	$[\mathrm{s}]$

λ_H	time constant of the Hookean dumbbells	[s]
$\lambda_{2,EVSS}$	deformation retardation time from stress splitting approach	[s]
$\boldsymbol{\pi}$	total stress tensor	[Pa]
$\boldsymbol{\pi}_p$	polymer contribution to the total stress tensor	[Pa]
$\boldsymbol{\pi}_s$	solvent contribution to the total stress tensor	[Pa]
ρ	density	$[\mathrm{kg\,m^{-3}}]$
σ	surface tension	$[\mathrm{N\,m^{-1}}]$
$\boldsymbol{\tau}$	extra stress tensor	$[\mathrm{N\,m^{-2}}]$
$\boldsymbol{\tau}_p$	polymer contribution to the extra stress tensor	$[\mathrm{N\,m^{-2}}]$
$\boldsymbol{\tau}_s$	solvent contribution to the extra stress tensor	$[\mathrm{N\,m^{-2}}]$
φ	azimuth angle	[rad]
φ_0	fitted initial phase angle	[rad]
$\boldsymbol{\Psi}$	probability function	$[-]$
$\boldsymbol{\omega}$	vorticity vector	$[\mathrm{s^{-1}}]$
Ω	non-dimensional complex frequency	$[-]$
ω	angular frequency	$[\mathrm{s^{-1}}]$

1 Introduction

The main emphasis of this work is on viscoelastic liquids, their properties and their behavior under small deformations. To describe the linear dynamic behaviour of the polymeric liquids a linearized Oldroyd-B model [1, 2], also known as the Jeffreys model [3, 4], was used:

$$\boldsymbol{\tau} + \lambda_1 \dot{\boldsymbol{\tau}} = \eta_0 \left(\dot{\gamma} + \lambda_2 \frac{\partial \dot{\gamma}}{\partial t} \right), \tag{1.1}$$

where $\boldsymbol{\tau}$ and $\dot{\gamma}$ are the deformation-induced stress and the rate of deformation tensors, respectively. This mathematical model contains three independent parameters; the zero-shear-rate viscosity η_0, i.e. the viscosity at low shear rates, and two material time constants: the stress relaxation time λ_1 and the deformation retardation time λ_2. This two polymeric time scales are important parameters in mathematical models describing the rheological behaviour of viscoelastic liquids upon small deformations. In the case of small deformations of a liquid element, the polymeric time scales λ_1 and λ_2 describe the stress relaxation after removal of strain and rate of strain relaxation after removal of stresses, respectively. In other words, as stated by Oldroyd [2, 5] when the rate of deformation is stopped, any small stress decays as e^{-t/λ_1}, and if the stress is removed, the rate of deformation decays as e^{-t/λ_2}.
Molecular mechanical properties of dissolved polymeric substances are responsible for the time scales, and computational methods for quantifying them from first principles are in general unavailable. While the stress relaxation time of spinnable liquids can be measured by standard filament stretching elongational rheometers [6–9], a standard method for measuring the deformation retardation time is not established (e.g. [10]).

It is important to note, however, that in Oldroyd's theoretical framework the polymeric time scales are material constants, which are treated as

independent of each other. In contrast to the Oldroyd derivation [1, 2], there are alternative derivations of the Oldroyd-B model [3, 4, 11, 12], where the retardation time is proportional to the relaxation time. This relationship follows from the so-called *stress-splitting approach*. where the extra stress tensor is written as the sum of solvent and polymer contributions. The stress splitting approach also implies, that the total zero shear viscosity is a sum of solvent and polymer viscosity. From this point of view can be argued, why there is no necessity to develop a method for measuring the deformation retardation time. Nevertheless, there is nowhere to be found a demonstration of the validity of the stress splitting approach, neither the limitations of the approach. In the literature studied the stress splitting approach is usually postulated and used without further explanations.

In the present thesis a method for measuring the deformation retardation time of polymeric liquids from damped drop shape oscillations [13, 14] was developed. The measured λ_2 is compared to the calculated deformation retardation time λ_2^* given by the equation derived from the stress splitting approach.

1.1 Complex fluids

Complex fluids, or more specially viscoelastic fluids, are a group of non-Newtonian fluids, for which the classical Newtonian law does not hold. Viscoelastic fluids show both viscous and elastic properties simultaneously. Newton's law describes the behaviour of an ideal viscous fluid - the Newtonian fluid, and Hooke's law describes the behaviour of an ideal elastic body - the Hookean body.

Hookean body
The ideal elastic body obeys Hooke's law, which states that the stress τ is proportional to the strain γ. The proportionality constant is the elastic modulus G. Hooke's law, formulated in a correct tensor form [15] is written as

$$\boldsymbol{\tau} = \mathbf{C} \cdot \boldsymbol{\gamma}, \tag{1.2}$$

where $\boldsymbol{\tau}$ is the stress tensor, $\boldsymbol{\gamma}$ is the strain tensor and $\mathbf{C}$ is a fourth order tensorial material constant called the elasticity tensor. Once the strain (force)

is removed the original shape of the Hookean body and the deformation energy are restored.

Newtonian fluid
For ideal viscous fluid under shear stress, Newton derived a law analogous to the Hookean where the deformation-induced stress is linearly related to the strain rate $\dot{\gamma}$ and the linearity constant is the fluid dynamic viscosity η. The constitutive equation in tensor form for the incompressible Newtonian fluid is written as

$$\boldsymbol{\tau} = \eta \dot{\boldsymbol{\gamma}}, \tag{1.3}$$

where $\boldsymbol{\tau}$ is the stress tensor and $\dot{\boldsymbol{\gamma}}$ is the rate of deformation tensor.

If the relationship between the shear stress and the strain rate is not linear, then the fluid is called a *non-Newtonian fluid*. In that case the fluid viscosity is a function of shear stress or strain rate. The non-Newtonian behavior depends on the fluid microstructure and can be characterized as shear-thinning or shear-thickening. The viscosity of shear-thinning fluids decreases with increasing shear rate, while for sheer-thickening liquids the fluid viscosity increases with increasing shear rate. The behaviour of the shear-thinning, shear-thickening and Newtonian fluids is demonstrated in figure 1.1.

Generalised Newtonian fluid
The most simple extension of the linear Newtonian model are the generalised Newtonian models ([3], pp. 169-174). These type of models are non-linear in their nature because they incorporate the shear-rate dependent viscosity $\eta(\dot{\gamma})$. The generalized Newtonian fluid model is given by the rheological equation

$$\boldsymbol{\tau} = \eta(\dot{\gamma})\dot{\boldsymbol{\gamma}}, \tag{1.4}$$

where $\dot{\gamma} = \sqrt{\dot{\boldsymbol{\gamma}} : \dot{\boldsymbol{\gamma}}/2}$ is the second invariant of the shear rate tensor. The generalized Newtonian model describes the behaviour of inelastic fluids, where the material stress response depends only on the instantaneous deformations and not on the deformation history. Thus, the generalized Newtonian model is not able to model the relaxation behaviour of viscoelastic materials.
There are various empirical expressions for describing non-Newtonian viscosity behaviour $\eta(\dot{\gamma})$ [3, 15–17]. The most commonly used are the *power-law*

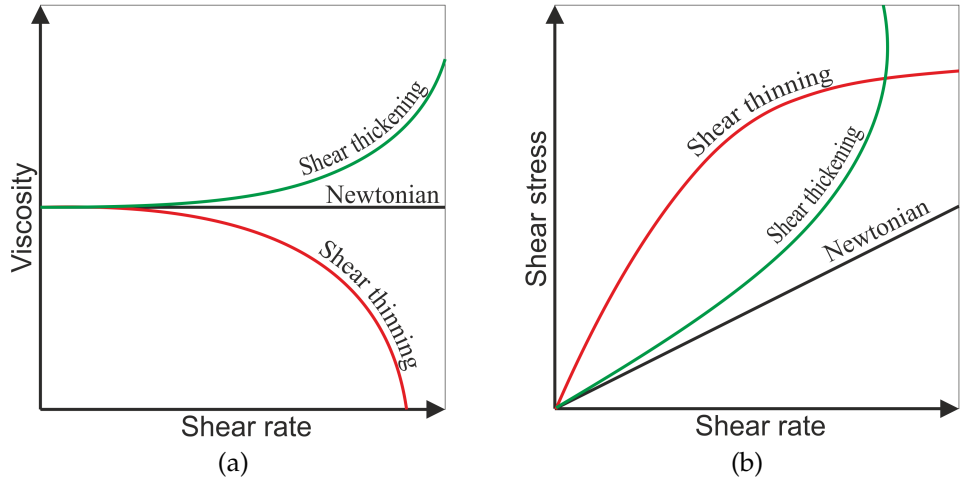

Figure 1.1: Behaviour of Newtonian and non-Newtonian fluids. (a) The fluid viscosity against the shear rate and (b) the shear stress against the shear rate.

model and the *Carreau-Yasuda model*.
The power-law model is given as

$$\eta = k\dot{\gamma}^{n_0-1} \tag{1.5}$$

where n_0 is the power-law exponent and k is the consistency factor with units of $\text{Pa} \cdot \text{s}^{n_0}$. Both n_0 and k are temperature dependent [3]. In case of $n_0 = 1$ and $k = \eta$ the Newtonian model is recovered. For $n_0 < 1$, equation (1.5) describes shear-thinning fluid behaviour, and for $n_0 > 1$, shear-thickening behaviour is represented. The power-law model (1.5) describes the viscosity in a narrow range of shear rates.
The Carreau-Yasuda model contains five parameters and is given as

$$\frac{\eta - \eta_\infty}{\eta_0 - \eta_\infty} = \left(1 + (K_1\dot{\gamma})^{n_1}\right)^{\frac{n_0-1}{n_1}}. \tag{1.6}$$

Here η_0 (*zero-shear-rate viscosity*) and η_∞ (infinite-shear-rate viscosity) are the asymptotic viscosity values in the limits of very small ($\dot{\gamma} \to 0$) and very large shear rates ($\dot{\gamma} \to \infty$), respectively. The exponent n_0 is the same as in the power-law model (1.5). Further, K_1 is the model parameter and n_1 is the Yasuda exponent. For $n_1 = 2$, a so-called Carreau model is obtained ([3], p. 172, [15], p. 96).

Viscoelastic materials
The ideal elastic and the ideal viscous behaviors are considered as idealizations, which can be realized only partially. In reality, most of the materials show combined features of both ideal models and are therefore called viscoelastic materials. Typical representatives of viscoelastic materials are viscoelastic fluids like polymer solutions.
The internal stresses of viscoelastic materials are functions of both the instantaneous deformation and also the deformation history. If the deformations or stresses are small enough, so that the rheological properties do not depend on the deformation, then the term linear viscoelasticity is used [3, 15, 17].
The typical characteristic features of viscoelastic materials are the stress relaxation and creep deformations. The stress response of the viscoelastic materials strongly depends on the time scale of deformations and the characteristic time scale of the material. A typical illustrative example is *silly putty*[1], a silicone based material. Over a long time period silly putty behaves as a viscous liquid, while at short time scales acts as an elastic solid. The constitutive equations (1.5) and (1.6) are not able to describe such type of viscoelastic behaviour. The proper constitutive equations for viscoelastic liquids will be presented in section 3.

To characterize the nature of a specific material, two important dimensionless numbers containing the characteristic time scales were constructed [15, 18]. The non-dimensional *Deborah number* is introduced as

$$\mathrm{De} = \frac{\lambda}{t_e} = \lambda\omega \tag{1.7}$$

where λ is the characteristic time scale, t_e is the time of observation and $\omega = 1/t_e$ is the characteristic frequency. The time of observation t_e is a time scale on which the experiments take place. The relaxation time λ is a material-dependent characteristic time scale on which the stress relaxes after removal of strain. For $\mathrm{De} \gg 1$, the material shows elastic or solid-like behavior, while for $\mathrm{De} \ll 1$ the viscous behavior is dominant. In case of $\mathrm{De} \cong 1$ the material behavior can be regarded as viscoelastic.
The *Weissenberg number* Wi represents the ratio between elastic and viscous

[1] Silly putty, URL: `https://en.wikipedia.org/wiki/Silly_Putty`

forces and is usually given as a product of the characteristic time scale (λ) and characteristic shear rate ($\dot{\gamma}$) (see [15], p. 71)

$$\mathrm{Wi} = \lambda\dot{\gamma}. \tag{1.8}$$

Poole [18] remarked that the Weissenberg number can be interpreted as representing the recoverable strain in the fluid. As noted further in [18], in steady simple shear flow the dominant elastic force will be due to the first normal-stress difference N_1, and the viscous force is due to the shear stress. Figure 1.2 shows the so-called Pipkin's diagram [15], which demonstrates the material behaviour as a function of the Deborah and Weissenberg numbers.

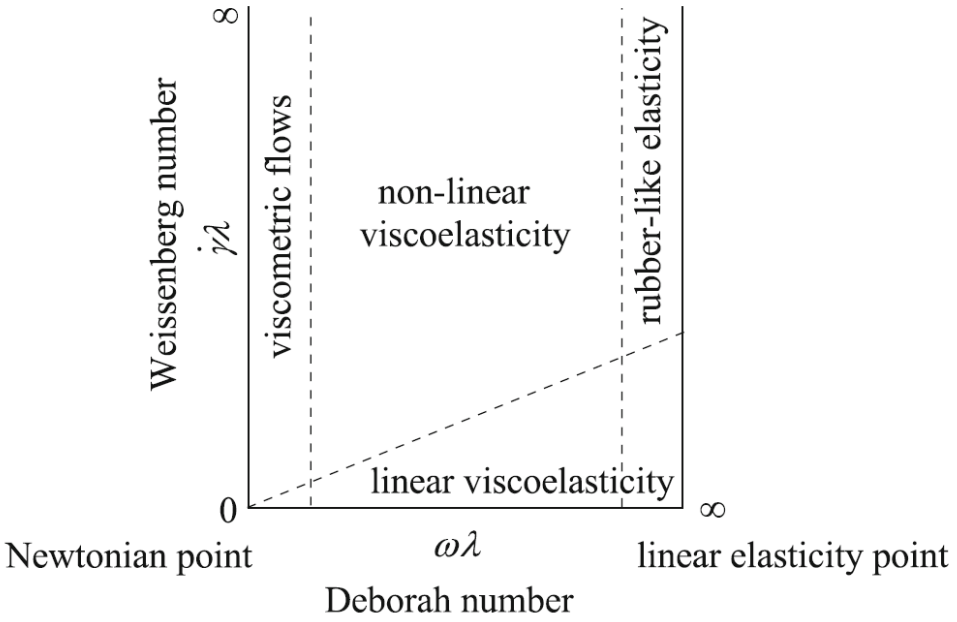

Figure 1.2: Pipkin diagram showing different material responses as a function of the Deborah and Weissenbergs number. Adapted from [15].

1.2 Polymeric time scale measurements

As already mentioned, methods for measuring the stress relaxation time are well established, while a standard method for measuring the deformation retardation time of polymer solutions is not yet established. In general, polymer solutions may exhibit spectra of both the stress relaxation and the deformation retardation times rather than single values [14]. For many flows, however, the largest values in the spectra dominate the dynamic fluid behaviour [19]. In filament stretching elongational rheometry, e.g., the longest stress relaxation time is measured, a quantity essential for the characterization of fluids in uniaxial elongational flow. The same approach is taken in the present work for the deformation retardation time.

The first attempt to measure the deformation retardation time (and the stress relaxation time) was made in 1951 by Oldroyd *et al.* [5]. In their work, they designed and tested a coaxial-cylinder elasto-viscometer, an instrument for measuring the elastic and viscous properties of viscoelastic polymer solutions. The narrow annular gap formed between two vertical coaxial cylinders was filled with the test liquid.
The viscosity of the liquids was measured using steady rotation of the cylinders, where the viscoelastic liquid behaves as purely viscous with a shear rate dependent viscosity. The viscoealastic properties were measured in the experiments involving oscillatory motion of the cylinders. The outer cylinder undergoes forced harmonic oscillations of known angular frequency and amplitude about its axis, while the inner cylinder is constrained by a torsion wire of known restoring constant. As a result from the oscillatory measurements, the ratio of the observed amplitudes of the inner and outer cylinders against the angular frequency is obtained. In order to deduce the polymeric time scales λ_1 and λ_2, the linearized Oldroyd-B equation must first be solved for this particular problem. The numerical solution, presented in a separate paper by Oldroyd [20], is then fitted to the measured frequency-amplitude-ratio curve with the polymeric time scales as fitting parameters. As noted by Oldroyd *et al.* [5], the preliminary results show that the linearized Oldroyd-B model was able to describe the measured data. In contrast, as noted further in [5], the Maxwell viscoelastic model [3], which contains only one polymeric time scale, was inadequate to describe the measured data.

The same instrument was later used by Toms et al. [21] to characterize dilute solutions of highly polymerized methyl methacrylate in different solvents. The measurements were conducted at different temperatures, ranging from 15 °C to 45 °C. It was found that both the zero shear rate viscosity and stress relaxation time depend on the polymer concentration, the temperature and the nature of the solvent. On the other hand, the deformation retardation time has a nearly constant value with no large deviation.

Chapman *et al.* [22] proposed an experimental technique to measure the deformation retardation time of large DNA molecules. The measured deformation retardation time was used to determine the molecular weight of the DNA molecules. These authors used a rotating Cartesian-diver viscometer for performing creep-recovery experiments. The solutions of DNA molecules cause the reversal of the direction of rotation of the viscometer rotor after the driving torque is suddenly removed. The motion of the rotor decays as an exponential function of time, where the characteristic decay time is identified as the deformation retardation time.
A method to obtain discrete retardation time spectra from creep and recovery data was proposed by Kaschta *et al.* [23, 24]. The method was applied in the glass-rubber transition region of polymer melts.

1.3 Oscillating drop method

The deformations of a drop surface due to shape oscillations may influence transport processes across the liquid/gas interface, such as the evaporation of the drop or the absorption of gases from the environment. For their relevance for transport processes, and for scientific interest, oscillations of liquid drops have been under investigation since the time of Lord Rayleigh, who derived the angular frequency

$$\alpha_{m,0} = \sqrt{m(m-1)(m+2)}\sqrt{\frac{\sigma}{\rho a^3}} \tag{1.9}$$

of linear oscillations of mode m for an inviscid drop with density ρ, surface tension σ and radius a against the ambient vacuum [25]. As noted in [26], the modes $m = 0$ and $m = 1$ describe the volumetric pulsation and

the translatory motion of the drop, respectively. Hence, the fundamental oscillation mode is $m = 2$, which describes elongation and contraction of the droplet. The first three oscillation modes for $m \geq 2$ are shown in Figure 1.3.

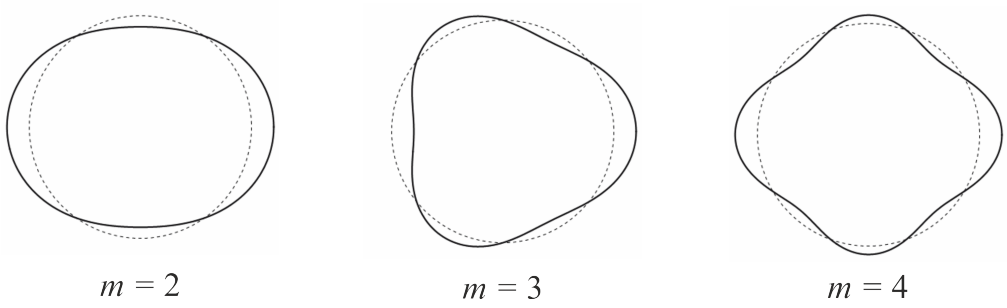

Figure 1.3: The first three oscillation modes. The dashed line represents the undeformed spherical drop shape in equilibrium.

Lamb extended the work of Rayleigh by considering the influence of the drop liquid viscosity [27], and obtained the amplitude decay time t_m of the m-th mode oscillation as

$$t_m = \frac{\rho a^2}{(m-1)(2m+1)\eta} \tag{1.10}$$

and the oscillation frequency

$$\alpha_m^* = \alpha_{m,0}\sqrt{1 - (t_m\,\alpha_{m,0})^{-2}} \tag{1.11}$$

where η is the fluid viscosity, which reduces the natural oscillation frequencies.
Lamb also generalized Rayleigh's result by including the influence from a host medium with a non-negligible density ρ_0 on the oscillations of an inviscid drop [28]. He obtained a dependency of the angular frequency of oscillation on a weighted sum of the two densities,

$$\alpha_{m,0}^L = \sqrt{\frac{m(m-1)(m+1)(m+2)}{m\rho_0 + (m+1)\rho}}\sqrt{\frac{\sigma}{a^3}}. \tag{1.12}$$

The general case of the small-amplitude oscillation of a viscous fluid drop immersed in another viscous fluid with non-negligible density was studied by Miller & Scriven [29]. They derived the characteristic equation of the oscillating drop in the form of a determinant which must be equal to zero. For the different special cases of fluid behaviour, the equation reduces to the known results of previous studies.

The characteristic equation of the oscillating drop determines the dependencies of the drop shape oscillation frequency and damping rate on physical properties of the drop liquid [13]. These dependencies allow these physical properties to be measured when the oscillation frequency and the damping rate are known. This "oscillating drop method" for measuring various liquid physical properties has been in use for several decades. In order to produce and investigate oscillating drops, the drops must be levitated by an appropriate technique. There are different levitation techniques available which allow a non-contact handling of the test sample: electrical, magnetic, aerodynamic and acoustic levitation [30]. In the present work the acoustic levitation technique was used [31], which will be explained in detail in Section 6.1.1.

The oscillating drop method was used for measuring the interfacial tension between two immiscible liquids [32] and the surface tension of the drop liquid against the ambient air [33]. The former authors used quadropole shape oscillations of an acoustically levitated drop in another liquid. They related the resonance properties of the drop to the interfacial tension [32]. The latter authors determined the liquid surface tension by measuring the frequency of an oscillating liquid droplet obtained by the break up of a liquid jet [33].

Next to the interfacial tension, the dynamic viscosity of various Newtonian liquids was measured using the drop oscillation method. Egry *et al.* measured the dynamic viscosity of the eutectic $Pd_{78}Cu_6Si_{16}$ over a wide temperature range, including the eutectic temperature of 1033 K [34]. The authors performed the damped drop oscillation experiments under microgravity conditions and related the dynamic viscosity to the damping rate. They have found a very good agreement between the measured dynamic viscosity and the values known from the literature. The resonance behaviour of the oscillating drop was studied by Perez *et al.* [35]. The authors take into

account the spheroidal shape of the drop and the velocity field inside the drop. They obtained a correlation of the dynamic viscosity with the width of the resonance peak. The method enables accurate measurements of the dynamic liquid viscosity in the range between 2 mPa s and 150 mPa s. The authors propose to apply the method to suspensions and to materials in the semisolid state [35].

The oscillating drop method was used to investigate the surface rheology of viscoelastic systems [36, 37]. The experiments with drops of surfactant solutions were performed under microgravity conditions. In the work of Tian *et al.*, complementary effects of the surface and the bulk viscosities were found. The damping rate of the oscillating drop is affected by the surface viscosity, due to the coupling between the surface viscous and elastic effects [36]. In the experiments of Apfel *et al.*, free drop oscillations were excited by loudspeakers. From the measured oscillation frequency of the drop, both bulk and surface viscoelastic properties of surfactant solutions were determined. The goal of the study was to develop rational models of the surfactant behaviour [37]. A detailed review of oscillating drop and bubble techniques can be found in the work by Kovalchuk *et al.* [38].

Most recent experiments using freely decaying oscillations of acoustically levitated droplets were reported in [39]. They simultaneously measured the surface tension and viscosity of different oils and alcohols by analyzing the freely decaying drop oscillations. They compared their results to the data from the literature and found an absolute deviation ranging from 2.63% to 15.4% in viscosity measurements and an absolute deviation ranging from 4.06% to 7.35% for the surface tension. The experimental method used was identical to the method proposed in the present thesis. The difference is, however, that they studied only Newtonian liquids, while the focus of the present work is on viscoelastic liquids.

1.4 Aim and organisation of the work

The present thesis aims to provide an experimental method for measuring the deformation retardation time of polymeric liquids and to carry out

measurements for various aqueous polymer solutions. The method is based on small amplitude damped drop oscillations using the acoustic levitation technique [13, 14].

The remainder of the dissertation is organized as follows:
Chapter 2 presents a brief review of the continuum mechanics and the governing equations of fluid kinematics and fluid dynamics. These equations are the conservation of mass, the conservation of momentum, and the expressions for the rate of deformation tensor and deformation gradient tensor.

Chapter 3 deals with the polymer rheology and the constitutive modeling. Two approaches leading to the differential constitutive equations are explained; the micro-structural approach and the continuum approach. As an appropriate rheological model the Oldroyd-B model is selected which is given in different formulations. The linearized Oldroyd-B has the simplest form among the other models, it is easy to implement and requires no additional assumptions about the fluid properties.

Chapter 4 presents a thorough mathematical analysis of linear damped viscoelastic drop oscillations. As a result of the analysis, the characteristic equation for the complex angular frequency of the drop is obtained. The dimensional analysis of the characteristic equation is conducted, and the ranges of the non-dimensional parameters (the Ohnesorge and the Deborah numbers) for which shape oscillations exist are determined. Next, the necessary steps for solving the characteristic equation for the unknown deformation retardation time are given. The characteristic equation is transcendental in the complex argument of the spherical Bessel functions involved and must be solved numerically. Due to the nature of the spherical Bessel functions, the equation produces a manifold of solutions, from which the correct one must be identified.

Chapter 5 presents a thorough characterization of the viscoelastic liquids studied in the present thesis. The available experimental methods for measuring the relevant rheological properties are described. These properties are the zero shear viscosity, surface tension and the stress relaxation time.

Chapter 6 describes the experimental part of the oscillating drop method for measuring the deformation retardation time. The fundamental part of

the experimental set-up is the acoustic levitator which is explained in detail. The outcome of the measurements are the equilibrium drop radius and the complex angular frequency of the fundamental oscillation mode. These values enter the characteristic equation, which is then solved for the unknown deformation retardation time. The measurement procedure is demonstrated with viscoelastic test liquids, and the results of the measurements are presented.

Chapter 7 provides the uncertainty and sensitivity analysis of the experimental method. The measured deformation retardation times are further analyzed and discussed.

Finally, **Chapter 8** provides the summary and conclusions of the thesis.

2 Review of continuum mechanics

In this section a basic principles of continuum mechanics are presented. The review is based on [3, 40–42], where the additional details can be found. Continuum mechanics is formally divided into solid mechanics and fluid mechanics. However, for many materials the classification into one of these two subgroups is not always possible.

Continuum mechanics deals with the kinematics and dynamics of the materials described as a continuous medium. A continuous medium, sometimes referred to as a body, is a mathematical model of the physical material where it is assumed that the occupied space is fully (continuously) filled with material particles.

2.1 Spatial and material coordinates

In the framework of continuum mechanics, the material behaviour can be described by two different mathematical formulations. The first formulation follows from the Lagrangian viewpoint, where the trajectories of specific material particles are followed. The second formulation is the Eulerian viewpoint, where the motion is described by spatio-temporal fields, either scalar or vector, rather than the temporal position of a material particle.
Let the initial location of a material particle at time $t = 0$ be given as $\boldsymbol{\zeta} = (\zeta_1, \zeta_2, \zeta_3)$. After time t, the material particle $\boldsymbol{\zeta}$ is located at a new position $\boldsymbol{x}$ given as

$$\boldsymbol{x} = \boldsymbol{x}(\boldsymbol{\zeta}, t), \qquad x_i = x_i(\zeta_1, \zeta_2, \zeta_3, t). \tag{2.1}$$

The equation (2.1) can also be inverted to give the initial position $\boldsymbol{\zeta}$ at time $t = 0$ of a particle that at time t is at position $\boldsymbol{x}$:

$$\boldsymbol{\zeta} = \boldsymbol{\zeta}(\boldsymbol{x}, t), \qquad \zeta_i = \zeta_i(x_1, x_2, x_3, t). \tag{2.2}$$

In principle the equations (2.1) or (2.2) are sufficient to completely describe the motion of a deformable body. If the motion is expressed with the initial coordinate configuration (2.1), then this is known as the Lagrangian or material description, where the coordinates $\boldsymbol{\zeta} = (\zeta_1, \zeta_2, \zeta_3)$ are the Lagrangian or material coordinates. If the motion is expressed with current coordinate configuration (2.2), then this is known as the Eulerian or spatial description where the coordinates $\boldsymbol{x} = (x_1, x_2, x_3)$ are called Eulerian or spatial coordinates.
Any physical property $\mathcal{P}$ of a continuum can be described either in spatial $\mathcal{P}(\boldsymbol{x}, t)$ or material coordinates $\mathcal{P}(\boldsymbol{\zeta}, t)$. The property $\mathcal{P}$ can be either scalar (density, pressure, temperature, ...), vector (position, velocity, acceleration, pressure gradient,...) or tensor (stress tensor, rate of deformation tensor, ...). The Eulerian description, which is usually used in fluid mechanics, gives a material property in a fixed position in space. The Lagrangian description gives the properties of the same material particle. This description is usually used in solid mechanics.
Special care must be taken when calculating the time derivative of a physical property $\mathcal{P}$ of the material because the time derivative has a different meaning in material and spatial coordinates. The time derivative in Eulerian coordinates, also known as the local derivative, is defined as

$$\left(\frac{\partial \mathcal{P}(\boldsymbol{x}, t)}{\partial t}\right)_{\boldsymbol{x}} = \frac{\partial \mathcal{P}(\boldsymbol{x}, t)}{\partial t} \tag{2.3}$$

and represents the time variation of the property $\mathcal{P}$ at a given location.
The time derivative in Lagrangian coordinates, also known as the material derivative or the substantial derivative, is written as

$$\left(\frac{\partial \mathcal{P}(\boldsymbol{\zeta}, t)}{\partial t}\right)_{\boldsymbol{\zeta}} = \frac{\mathrm{D}\mathcal{P}(\boldsymbol{\zeta}, t)}{\mathrm{D}t} \tag{2.4}$$

where the material derivative is an operator defined as

$$\frac{\mathrm{D}}{\mathrm{D}t} := \frac{\partial}{\partial t} + \boldsymbol{u} \cdot \nabla, \tag{2.5}$$

with the local velocity $\boldsymbol{u}$ and the convected derivative $(\boldsymbol{u} \cdot \nabla)$. The material derivative describes the time variation of the property $\mathcal{P}$ of a specific material particle that moves in a velocity field with velocity $\boldsymbol{u}$. The material derivative can also be viewed as a connection between the Lagrangian description and the Eulerian description.

To understand fluid dynamics or kinetics, i.e., the relationship between fluid motion and its causes, the basic principles of fluid kinematics must be presented.

2.2 Kinematics

Kinematics describes the fluid motion, without considering the forces which caused the motion. Thereby it does not matter what kind of material is in question.

In the Eulerian approach, the fluid motion is described by the velocity field $\boldsymbol{u}(\boldsymbol{x}, t)$. At a given time t, the velocity at location $\boldsymbol{x}$ is related to the velocity at the neighboring location $\boldsymbol{x} + \mathrm{d}\boldsymbol{x}$ as ([42], p. 105)

$$\boldsymbol{u}(\boldsymbol{x} + \mathrm{d}\boldsymbol{x}) = \boldsymbol{u}(\boldsymbol{x}) + \nabla \boldsymbol{u}^{\mathrm{T}} \mathrm{d}\boldsymbol{x}. \tag{2.6}$$

Equation (2.6) may be rewritten as

$$\mathrm{d}\boldsymbol{u} = \boldsymbol{u}(\boldsymbol{x} + \mathrm{d}\boldsymbol{x}) - \boldsymbol{u}(\boldsymbol{x}) = \nabla \boldsymbol{u}^{\mathrm{T}} \mathrm{d}\boldsymbol{x} := \mathbf{L} \cdot \mathrm{d}\boldsymbol{x} \tag{2.7}$$

where the velocity gradient tensor $\mathbf{L}$ is introduced as

$$\mathbf{L} = (\nabla \boldsymbol{u})^{\mathrm{T}}, \quad \text{with the Cartesian components} \quad L_{ij} = \frac{\partial u_j}{\partial x_i}. \tag{2.8}$$

This gradient tensor may be decomposed into a symmetric part $\mathbf{D}$ and an antisymmetric part $\mathbf{W}$ as

$$\mathbf{L} = \mathbf{D} + \mathbf{W} \tag{2.9}$$

where

$$\mathbf{D} = \frac{1}{2}\left(\mathbf{L} + \mathbf{L}^{\mathrm{T}}\right) = \frac{1}{2}\left((\nabla \boldsymbol{u})^{\mathrm{T}} + \nabla \boldsymbol{u}\right) \tag{2.10}$$

is the rate of deformation tensor and

$$\mathbf{W} = \frac{1}{2}\left(\mathbf{L} - \mathbf{L}^{\mathrm{T}}\right) = \frac{1}{2}\left((\nabla \boldsymbol{u})^{\mathrm{T}} - \nabla \boldsymbol{u}\right) \tag{2.11}$$

is the vorticity tensor. The rate of deformation tensor **D** describes the rate of stretching and shearing. The vorticity tensor **W** describes the rate of rotation of a solid body at a given location. Its components can be alternatively computed as

$$W_{ij} = -\frac{1}{2}\varepsilon_{ijk}\omega_k \tag{2.12}$$

where

$$\boldsymbol{\omega} = \boldsymbol{\nabla} \times \boldsymbol{u} \tag{2.13}$$

is the vorticity vector and ε_{ijk} is the Levi-Civita symbol defined as

$$\varepsilon_{ijk} = \begin{cases} 1, \text{ if } (ijk) \text{ is an even permutation of numbers} \\ -1, \text{ if } (ijk) \text{ is an odd permutation of numbers} \\ 0, \text{ else.} \end{cases} \tag{2.14}$$

For irrotational flow, both **W** and $\boldsymbol{\omega}$ are zero.

For complex fluids, like viscoelastic liquids, the above derived tensors are not sufficient for describing the deformations ([3], pp. 425-426). Additional information about the deformation can be obtained considering the Lagrangian approach and describing the deformations in the vicinity of the material particle [3].
A line element $\mathrm{d}\boldsymbol{\zeta}$ at position $\boldsymbol{\zeta}$ in the initial configuration becomes $\mathrm{d}\boldsymbol{x}$ in the new configuration at time t. The current line element $\mathrm{d}\boldsymbol{x}$ is expressed as

$$\mathrm{d}\boldsymbol{x} = \boldsymbol{x}(\boldsymbol{\zeta} + \mathrm{d}\boldsymbol{\zeta}) - \boldsymbol{x}(\boldsymbol{\zeta}) := \mathbf{E}\mathrm{d}\boldsymbol{\zeta} \tag{2.15}$$

where the deformation gradient tensor **E** is introduced as

$$\mathbf{E} = \left(\frac{\partial \boldsymbol{x}}{\partial \boldsymbol{\zeta}}\right)^{\mathrm{T}}, \quad \text{with the Cartesian components} \quad E_{ij} = \frac{\partial x_j}{\partial \zeta_i}. \tag{2.16}$$

The deformation gradient tensor relates the line element in the initial configuration to the line element in the present configuration and contains the

information about the deformation and rotation in the neighborhood of a given material particle. Since a rotation of a material cannot induce stresses, it is convenient to define strain tensors without influences of solid body rotation [3, 17, 43, 44]. These rotation-independent strain tensors are the *right Cauchy-Green strain tensor*

$$\mathbf{C} = \mathbf{E}^{\mathrm{T}}\mathbf{E} \tag{2.17}$$

and the *left Cauchy-Green strain tensor* or the *Finger strain tensor*

$$\mathbf{B} = \mathbf{E}\mathbf{E}^{\mathrm{T}}. \tag{2.18}$$

The physical meaning of $\mathbf{C}$ and $\mathbf{B}$ is evident when considering the transformation of the inner product of two line elements (see [43], p. 21, [44], p. 26 or [42], pp. 112-113). Let $\mathrm{d}\boldsymbol{x}^{(1)}$ and $\mathrm{d}\boldsymbol{x}^{(2)}$ be the line elements in the current configuration and $\mathrm{d}\boldsymbol{\zeta}^{(1)}$ and $\mathrm{d}\boldsymbol{\zeta}^{(2)}$ the line elements in the initial configuration. The inner product of the current line elements is

$$\mathrm{d}\boldsymbol{x}^{(1)} \cdot \mathrm{d}\boldsymbol{x}^{(2)} = \mathbf{E}\mathrm{d}\boldsymbol{\zeta}^{(1)} \cdot \mathbf{E}\mathrm{d}\boldsymbol{\zeta}^{(2)} = \mathrm{d}\boldsymbol{\zeta}^{(1)} \cdot \mathbf{E}^{\mathrm{T}}\mathbf{E} \cdot \mathrm{d}\boldsymbol{\zeta}^{(2)} := \mathrm{d}\boldsymbol{\zeta}^{(1)} \cdot \mathbf{C} \cdot \mathrm{d}\boldsymbol{\zeta}^{(2)} \tag{2.19}$$

and similarly for the initial line elements

$$\mathrm{d}\boldsymbol{\zeta}^{(1)} \cdot \mathrm{d}\boldsymbol{\zeta}^{(2)} = \mathrm{d}\boldsymbol{x}^{(1)} \cdot \mathbf{E}^{-\mathrm{T}}\mathbf{E}^{-1} \cdot \mathrm{d}\boldsymbol{x}^{(2)} := \mathrm{d}\boldsymbol{x}^{(1)} \cdot \mathbf{B}^{-1} \cdot \mathrm{d}\boldsymbol{x}^{(2)}. \tag{2.20}$$

Further details about strain tensors, can be found, for example, in [17] (pp. 29 - 37) and [42] (pp. 112-116).

2.3 Dynamics of fluids

The fluid dynamics or kinetics describes the relationship between fluid motion and its causes. The basic equation of continuum mechanics are the continuity equation and the Cauchy equation of motion, which are derived from the following physical laws of conservation:

- conservation of mass,
- conservation of momentum.

In the present thesis, only isothermal flows are considered, therefore the conservation of energy is not considered.

Conservation of mass
The law of conservation of mass states that the mass of a closed system must be constant over time. This can be expressed in differential form as

$$\frac{\partial \rho}{\partial t} + \boldsymbol{\nabla} \cdot (\rho \boldsymbol{u}) = 0 \tag{2.21}$$

which is known as the continuity equation, where ρ is the material density and $\boldsymbol{u}$ is the velocity field. For incompressible materials with constant density, $\rho = constant$, the above continuity equation (2.21) simplifies to

$$\boldsymbol{\nabla} \cdot \boldsymbol{u} = 0. \tag{2.22}$$

In the present work the emphasis is on incompressible fluids.

Conservation of momentum
The law of conservation of linear momentum is basically the application of Newton's second law to the continuum. If the density is constant, the conservation of momentum equation leads to the Cauchy equation of motion

$$\rho \frac{\partial \boldsymbol{u}}{\partial t} + \rho(\boldsymbol{u} \cdot \boldsymbol{\nabla})\boldsymbol{u} = \boldsymbol{\nabla} \cdot \boldsymbol{\pi} + \rho \boldsymbol{f}^B \tag{2.23}$$

where $\boldsymbol{f}^B$ represents the volume forces and $\boldsymbol{\pi}$ is the Cauchy stress tensor or the total stress tensor. Equation (2.23) is also known as the *Cauchy first law of motion*. The volume force $\boldsymbol{f}^B$, also called body force, which acts on the volume element of the material, is in most problems equal to the gravitational acceleration or set to zero. Conservation of angular momentum, together with the conservation of mass (2.22) and linear momentum (2.23), results in

$$\boldsymbol{\pi} = \boldsymbol{\pi}^{\mathrm{T}}, \tag{2.24}$$

i.e., the total stress tensor is symmetric [15, 45]. The equation (2.24) is also known as the *Cauchy second law of motion*.

For an incompressible fluid the total stress tensor $\boldsymbol{\pi}$ is usually decomposed as

$$\boldsymbol{\pi} = \boldsymbol{\tau} - p \cdot \boldsymbol{\delta}, \tag{2.25}$$

where p is the hydrodynamic pressure, δ is the unit tensor and τ is the extra stress tensor or deviatoric stress tensor, which is determined by the deformation history. As remarked in ([3], pp. 10-11), for an incompressible fluid, only the gradient of p needs to be known for solving hydrodynamic problems. Further, p can be determined by solving the equations of motion with appropriate boundary conditions. On the other side, the extra stress tensor τ must be determined from the appropriate rheological model, i.e., the constitutive equation, which relates the stresses to the material deformations. The constitutive equations in general describe all the differences between Newtonian and non-Newtonian fluid behaviour.

3 Rheological constitutive equations for viscoelastic liquid

In viscoelastic fluid mechanics we face the fundamental problem of relating the stress tensor to the material deformation. This relation is given by the constitutive equation of the material. Some of the well-known constitutive equations, as for the Hookean body (1.2), the Newtonian fluid (1.3) and the simple non-Newtonian fluid (1.4), were already presented in the Introduction.

To construct appropriate constitutive equations, many approaches have been developed [3, 4, 43–48]. These approaches can be formally divided into two categories: the *continuum (phenomenological) approach* and the *micro-structure approach*. The continuum approach can be divided further into *differential models* and *integral models*, depending on the mathematical form of the rheological model. The micro-structure approach constructs the constitutive models from assumptions on the structure of polymer chains and their behavior in the fluid flow. The micro-structure approach can be roughly divided into *dilute polymer solution theory*, the *network theories*, the *reptation theories* and *suspension models*.

3.1 Constitutive modelling: The continuum approach

In the continuum approach, the constitutive equations must satisfy certain fundamental principles, which were first introduced by Oldroyd [1] in 1950. According to Phan-Thien [15], these fundamental principles on which the constitutive equations must be based can be summarized as follows:

- *The principle of determinism of stress:* The current stress in the material is determined by the past history of motion of the material.
- *The principle of local action:* The stress at a given material point is determined by the history of the deformation within an arbitrarily small vicinity of the considered material point.
- *The principle of coordinates-indifference:* The constitutive equation must appear independent of the frame of reference. This principle is also known as the principle of material objectivity.

The first two principles are straightforward and easy to understand [15].

The third principle requires an objective time derivative of a tensor. Although shear rate tensor and stress tensor, and also the left Cauchy-Green strain tensor (2.17) and Finger strain tensor (2.18), are objective, their time derivatives (material time derivative or partial time derivative) do not fulfill the conditions of material objectivity.

A proper frame-indifferent rate tensor is obtained if the time derivative (material time derivative or partial time derivative) is taken with respect to the reference frame fixed to the body.

The Oldroyd convected derivative [1] is a time derivative in a local coordinate system which is embedded in the fluid and moving along with it, as stated in [3]. Two such Oldroyd derivatives can be formulated, the upper convected derivative $\overset{\triangledown}{\mathbf{T}}$ described in terms of contravariant components

$$\overset{\triangledown}{\mathbf{T}} \doteq \mathbf{T}^{(1)} = \frac{\mathrm{D}\mathbf{T}}{\mathrm{D}t} - \mathbf{L}\cdot\mathbf{T} - \mathbf{T}\cdot\mathbf{L}^{\mathrm{T}} \tag{3.1}$$

and the lower convected derivative $\overset{\triangle}{\mathbf{T}}$ described in terms of covariant components

$$\overset{\triangle}{\mathbf{T}} \doteq \mathbf{T}_{(1)} = \frac{\mathrm{D}\mathbf{T}}{\mathrm{D}t} + \mathbf{L}\cdot\mathbf{T} + \mathbf{T}\cdot\mathbf{L}^{\mathrm{T}}. \tag{3.2}$$

As noted in Han ([48], p. 34), when compared to experimental data, the material functions obtained from the upper convected time derivative of the stress tensor predict a correct trend, while material functions obtained from the lower convected time derivative of the stress tensor do not. Thus, the

upper convected time derivative is preferred over the lower convected time derivative.

It must be noted, that equations (3.1) and (3.2) are not the only equations which fulfill the conditions of frame-indifference [3, 43, 48]. The Jaumann or corotational derivative

$$\overset{\circ}{\mathbf{T}} = \frac{\mathrm{D}\mathbf{T}}{\mathrm{D}t} - \mathbf{W}\cdot\mathbf{T} + \mathbf{T}\cdot\mathbf{W} \tag{3.3}$$

is a time derivative with respect to a frame rotating with angular velocity $\frac{1}{2}\boldsymbol{\omega}$ of the fluid element ([48], p.34 and [43], p. 69). Although the corotational time derivative of the stress tensor provides some promising results [48–50], it will not be considered further.

3.1.1 Maxwell models

The simplest constitutive equation used for viscoelastic fluids is the so-called Maxwell model, where an objective derivative of the stress tensor is included. Depending on the type of the objective time derivatives one can define the *lower convected Maxwell model*

$$\boldsymbol{\tau} + \lambda_1 \overset{\triangle}{\boldsymbol{\tau}} = 2\eta_0 \mathbf{D}, \tag{3.4}$$

and the *upper convected Maxwell model*

$$\boldsymbol{\tau} + \lambda_1 \overset{\triangledown}{\boldsymbol{\tau}} = 2\eta_0 \mathbf{D}, \tag{3.5}$$

where λ_1 is the *Maxwell stress relaxation time* and η_0 is the *zero-shear-rate viscosity*.

The upper convected Maxwell (UCM) model gives better results regarding the magnitude of the first and second normal stress differences, therefore the UCM model is most preferred among the other Maxwell models ([43], p. 68, [48], p. 53). The main limitation of the (upper convected) Maxwell model is the shear-rate independent viscosity [3, 48].

3.1.2 Oldroyd models

The next step is to include the objective time derivative of the rate of deformation tensor in the constitutional equations. Oldroyd in his paper from 1950 [1], where the objective time derivatives were first introduced, writes the following two constitutive equations now known as the ***Oldroyd-A*** model

$$\boldsymbol{\tau} + \lambda_1 \overset{\triangle}{\boldsymbol{\tau}} = 2\eta_0 \left(\mathbf{D} + \lambda_2 \overset{\triangle}{\mathbf{D}} \right), \tag{3.6}$$

and the ***Oldroyd-B*** model

$$\boldsymbol{\tau} + \lambda_1 \overset{\triangledown}{\boldsymbol{\tau}} = 2\eta_0 \left(\mathbf{D} + \lambda_2 \overset{\triangledown}{\mathbf{D}} \right), \tag{3.7}$$

where λ_1 is the *stress relaxation time*, λ_2 is the *deformation retardation time* and $\lambda_1 \geq \lambda_2$. It is important to note that the three parameters (η_0, λ_1, λ_2) occurring in equations (3.6)-(3.7) are independent of each other. In the case of $\lambda_2 = 0$ the Oldroyd-A and Oldroyd-B models are reduced to the lower convected (3.4) and upper convected (3.5) Maxwell models, respectively. For $\lambda_1 = \lambda_2 = 0$, a Newtonian liquid is obtained.

As stated in by ([43], p. 68), the Oldroyd-B model is preferred against the Oldroyd-A model for the same reasons as given for the upper convected Maxwell model (see Bird *et al.* [3], p. 498, Han [48], p. 53 and Larson [43], p. 68). As noted in [45], the Oldroyd-B model qualitatively describes many features of the so-called Boger fluids [51], i.e. elastic fluids with constant viscosity.

In a simple steady shear flow, the Oldroyd-B model predicts a constant viscosity, a non-zero first normal stress difference and zero second normal stress difference (see [45], p. 187, [3], p. 354 and [48], p. 53). The shear-rate independent viscosity is the main limitation of the Oldroyd-B model [3, 48].

In his later work, Oldroyd [2] expanded the above convected three-parameter models by systematic inclusion of all quadratic terms in the velocity gradient and all allowable products of $\boldsymbol{\tau}$ and $\dot{\boldsymbol{\gamma}} = \boldsymbol{\gamma}_{(1)}$ [3, 52]. The proposed equation

is now known as the *Oldroyd 8-constant model*:

$$\boldsymbol{\tau} + \lambda_1 \overset{\triangledown}{\boldsymbol{\tau}} + \frac{1}{2}\lambda_3 \{\dot{\boldsymbol{\gamma}} \cdot \boldsymbol{\tau} + \boldsymbol{\tau} \cdot \dot{\boldsymbol{\gamma}}\} + \frac{1}{2}\lambda_5 (\operatorname{tr} \boldsymbol{\tau})\, \dot{\boldsymbol{\gamma}} + \frac{1}{2}\lambda_6 (\boldsymbol{\tau} : \dot{\boldsymbol{\gamma}})\, \boldsymbol{\delta} = \eta_0 \left[\dot{\boldsymbol{\gamma}} + \lambda_2 \overset{\triangledown}{\dot{\boldsymbol{\gamma}}} + \lambda_4 \{\dot{\boldsymbol{\gamma}} \cdot \dot{\boldsymbol{\gamma}}\} + \frac{1}{2}\lambda_7 (\dot{\boldsymbol{\gamma}} : \dot{\boldsymbol{\gamma}})\, \boldsymbol{\delta} \right] \quad (3.8)$$

where η_0 is again the zero-shear-rate viscosity and $(\lambda_1, ..., \lambda_7)$ are time constants. For different values of the time constants, equation (3.8) reduces to the known special cases [3, 52]:

- the Newtonian model (1.3) for λ_1 to λ_7 all equal to zero,
- the upper convected Maxwell model (3.5) for λ_2 to λ_7 all equal to zero and $\lambda_1 > 0$,
- the Oldroyd-B model (3.7) for λ_3 to λ_7 all equal to zero and $0 < \lambda_2 \leq \lambda_1$.

3.1.3 Other models

As noted in [3] (p. 353), there is no apparent reason for constitutive equations to be restricted to terms linear in stress.

Giesekus model
The Giesekus model [53] introduces the nonlinear term $\{\boldsymbol{\tau} \cdot \boldsymbol{\tau}\}$ which represents a hydrodynamic drag. The Giesekus model has the following form

$$\boldsymbol{\tau} + \lambda_1 \overset{\triangledown}{\boldsymbol{\tau}} - \alpha \frac{\lambda_1}{\eta_0} \{\boldsymbol{\tau} \cdot \boldsymbol{\tau}\} - \alpha\lambda_2 \{\dot{\boldsymbol{\gamma}} \cdot \boldsymbol{\tau} + \boldsymbol{\tau} \cdot \dot{\boldsymbol{\gamma}}\} = \eta_0 \left[\dot{\boldsymbol{\gamma}} + \lambda_2 \overset{\triangledown}{\dot{\boldsymbol{\gamma}}} + \alpha \frac{\lambda_2^2}{\lambda_1} \{\dot{\boldsymbol{\gamma}} \cdot \dot{\boldsymbol{\gamma}}\} \right] \quad (3.9)$$

where α is non-dimensional "mobility factor" and $0 \leq \alpha \leq 1$. If $\alpha = 0$ and $\lambda_2 > 0$ the Oldroyd-B model (3.7) is recovered. The Giesekus model predicts a finite value of the extensional viscosity for all extensional rates, shear thinning viscosity and nonzero first and second normal stress differences.

Phan-Thien-Tanner model
Another model containing a nonlinear stress term is the popular Phan-Thien-Tanner model

$$\Upsilon(\text{tr } \boldsymbol{\tau}) \cdot \boldsymbol{\tau} + \lambda_1 \overset{\triangledown}{\boldsymbol{\tau}} + \frac{\xi}{2} \{\dot{\boldsymbol{\gamma}} \cdot \boldsymbol{\tau} + \boldsymbol{\tau} \cdot \dot{\boldsymbol{\gamma}}\} = \eta \dot{\boldsymbol{\gamma}} \tag{3.10}$$

where ξ is a parameter and $\Upsilon(\text{tr } \boldsymbol{\tau})$ is a function of the trace of the stress tensor. The stress function Υ has either the exponential form

$$\Upsilon(\text{tr } \boldsymbol{\tau}) = \exp\left(\frac{\epsilon \lambda_1}{\eta}(\text{tr } \boldsymbol{\tau})\right), \tag{3.11}$$

or the linearized form

$$\Upsilon(\text{tr } \boldsymbol{\tau}) = 1 + \frac{\epsilon \lambda_1}{\eta}(\text{tr } \boldsymbol{\tau}), \tag{3.12}$$

where ϵ is the elongation parameter, which regulates the extensional viscosity. The parameters ϵ and ξ provide the correct shear thinning behaviour of the model.

3.2 Constitutive modelling: The micro-structure approach

In the micro-structure approach, the constitutive models are derived from assumptions on the behaviour of polymer molecules and their interaction with the solvent flow. The dilute solution theory with the dumbbell model is illustrated in this section by derivation of the Oldroyd-B model. The derivation follows the works of Bird *et al.* [3, 54], Larson [43], Phan-Thien [15], Huiligol and Phan-Thien [45] and Han [48]. The same constitutive equation as derived from the phenomenological approach is obtained.

Elastic dumbbell model

The simplest model of polymers is the so-called *elastic dumbbell model*, where two identical spherical beads with mass m_b are connected by a spring, as shown in figure 3.1. The orientation vector of the dumbbell is given as

$$\boldsymbol{R} = \boldsymbol{r}_2 - \boldsymbol{r}_1, \tag{3.13}$$

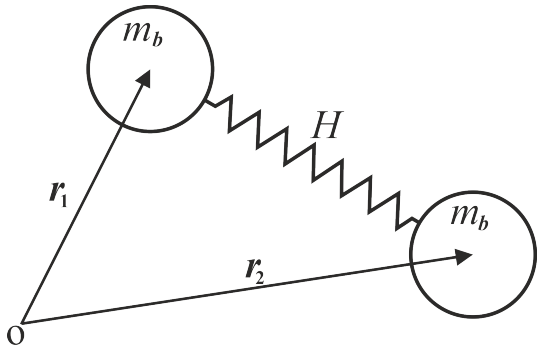

Figure 3.1: Elastic dumbbell model. Adapted from [15].

where $\boldsymbol{r}_1$ are $\boldsymbol{r}_2$ the position vectors of the beads.

The forces acting on each bead j are the spring force $\boldsymbol{F}^s_{(j)}$, the hydrodynamic drag force $\boldsymbol{F}^h_{(j)}$ and the Brownian force $\boldsymbol{F}^b_{(j)}$ [3]. The external forces such as gravity and electrical forces are neglected in the present derivation. For each bead of the dumbbell, an equation of motion can be written. By neglecting the inertial terms containing the bead masses, the equation of motion reduces to the simple force balance equation

$$\boldsymbol{F}^s_{(j)} + \boldsymbol{F}^h_{(j)} + \boldsymbol{F}^b_{(j)} = 0, \quad \text{with} \quad j = 1, 2. \tag{3.14}$$

The forces in equation (3.14) are given as follows:

- Spring force
  Assuming the linear Hookean law for the spring, then for each bead the spring force is given as

$$\begin{aligned} \boldsymbol{F}^s_{(1)} &= -H(\boldsymbol{r}_1 - \boldsymbol{r}_2) = H\boldsymbol{R} \\ \boldsymbol{F}^s_{(2)} &= -H(\boldsymbol{r}_2 - \boldsymbol{r}_1) = -H\boldsymbol{R} \end{aligned} \tag{3.15}$$

  where H is the spring constant.
- Hydrodynamic drag force
  This force represents the force of resistance experienced by the bead as it flows through the liquid. The simplest expression for the drag force is according to Stokes' law:

$$\boldsymbol{F}^h_{(j)} = -\zeta \left(\frac{\mathrm{d}\boldsymbol{r}_j}{\mathrm{d}t} - \boldsymbol{u}(\boldsymbol{r}_j) \right) \tag{3.16}$$

where $\boldsymbol{u}(\boldsymbol{r}_j)$ is the velocity of the solution at bead $\boldsymbol{r}_j$ and ζ is the drag coefficient given as

$$\zeta = 6\pi a_b \eta_s \tag{3.17}$$

with solvent viscosity η_s and radius of the spherical bead a_b. Assuming that the distance between the beads is small, then the following relation is obtained

$$\boldsymbol{u}(\boldsymbol{r}_2) - \boldsymbol{u}(\boldsymbol{r}_1) = \nabla \boldsymbol{u}^{\mathrm{T}} \cdot \boldsymbol{R}. \tag{3.18}$$

- Brownian force
  Due to the thermal fluctuations in the surrounding liquid, the beads experience a random fluctuating Brownian force, which is a stochastic process. Hence, for the Brownian force only statistical properties can be well defined. For the Brownian force $\boldsymbol{F}^b$ acting on the end-to-end vector one can write

$$\left\langle \boldsymbol{F}^b(t) \right\rangle = 0 \quad \text{and} \quad \left\langle \boldsymbol{F}^b(t)\boldsymbol{F}^b(t+t') \right\rangle = 4k_B T\zeta\delta(t')\boldsymbol{\delta} \tag{3.19}$$

  where k_B is the Boltzmann constant, T is the temperature and $\delta(t')$ is the Dirac delta function [15]. By introducing the configuration probability density function $\Psi(\boldsymbol{R}, t)$ for the end-to-end vector $\boldsymbol{R}$, the Brownian force may be expressed as

$$\boldsymbol{F}^b(t) = -k_B T \frac{\partial \Psi(\boldsymbol{R}, t)}{\partial \boldsymbol{R}} \tag{3.20}$$

  which is known as the *smoothed-out Brownian force* ([15], p. 123).

Inserting the above expressions for the forces into the force balance equation (3.14), then a stochastic differential equation is obtained. This equation can only be solved if the probability function $\Psi(\boldsymbol{R}, t)$ is specified. The stochastic differential equation can be converted in to the diffusion equation

$$\frac{\partial \Psi}{\partial t} = \frac{\partial}{\partial \boldsymbol{R}} \left[\frac{2k_B T}{\zeta} \frac{\partial \Psi}{\partial \boldsymbol{R}} - \left(\nabla \boldsymbol{u}^{\mathrm{T}} \cdot \boldsymbol{R} - \frac{2H}{\zeta} \boldsymbol{R} \right) \Psi \right] \tag{3.21}$$

which is known as the Fokker-Planck equation ([15], p. 129, [54], p. 62,). As noted further in [15] on page 129, it is usually not necessary to find the full probability distribution, since the quantity related to the stress is $\langle \boldsymbol{R}\boldsymbol{R} \rangle$. The expression for the mean dyadic $\langle \boldsymbol{R}\boldsymbol{R} \rangle$ can be obtained without solving the

diffusion equation (3.21) for the probability distribution Ψ, as explained in detail in [15] and [54]. The following equation of change for the mean dyadic $\langle \boldsymbol{RR} \rangle$ is obtained

$$\frac{\mathrm{d}}{\mathrm{d}t} \langle \boldsymbol{RR} \rangle - \nabla \boldsymbol{u}^{\mathrm{T}} \langle \boldsymbol{RR} \rangle - \langle \boldsymbol{RR} \rangle \nabla \boldsymbol{u} = \frac{4k_B T}{\zeta} \boldsymbol{\delta} - \frac{4H}{\zeta} \langle \boldsymbol{RR} \rangle . \tag{3.22}$$

The left-hand side of equation (3.22) can be recognized as the upper convected time derivative of $\langle \boldsymbol{RR} \rangle$. Considering the system in equilibrium, where $\mathrm{d} \langle \boldsymbol{RR} \rangle / \mathrm{d}t = 0$ and $\nabla \boldsymbol{u} = 0$, then from (3.22) follows.

$$\langle \boldsymbol{RR} \rangle_{eq} = \frac{k_B T}{H} \boldsymbol{\delta}. \tag{3.23}$$

As stated in Bird *et al.* ([54], p. 64), the total stress tensor $\boldsymbol{\pi}$ in a polymer solution can *presumingly* be written as the sum of the solvent contribution $\boldsymbol{\pi}_s$ and polymer contribution $\boldsymbol{\pi}_p$ as

$$\begin{aligned} \boldsymbol{\pi} &= \boldsymbol{\pi}_s + \boldsymbol{\pi}_p \\ &= (-p_s \boldsymbol{\delta} + \boldsymbol{\tau}_s) + (-p_p \boldsymbol{\delta} + \boldsymbol{\tau}_p) \\ &= -p \boldsymbol{\delta} + \boldsymbol{\tau} \end{aligned} \tag{3.24}$$

where

$$\begin{aligned} \boldsymbol{\tau} &= \boldsymbol{\tau}_s + \boldsymbol{\tau}_p = \eta_s \dot{\boldsymbol{\gamma}} + \boldsymbol{\tau}_p \\ p &= p_s + p_p. \end{aligned} \tag{3.25}$$

Different expressions relating $\langle \boldsymbol{RR} \rangle$ to the extra stress tensor $\boldsymbol{\tau}$ can be found, for example, in Bird *et al.* ([54], p. 69). For the present case of the Hookean dumbbells, the relevant equations are the Kramers expression

$$\boldsymbol{\tau} = 2\eta_s \mathbf{D} + n_d H \langle \boldsymbol{RR} \rangle - n_d k_B T \boldsymbol{\delta} \tag{3.26}$$

and the Giesekus expression

$$\boldsymbol{\tau} = 2\eta_s \mathbf{D} - \frac{n_d \zeta}{4} \overset{\triangledown}{\langle \boldsymbol{RR} \rangle} \tag{3.27}$$

with the number of dumbbells per unit volume n_d and assuming the Maxwellian velocity distribution of the beads ([54], pp. 69-71). Following

the steps described in Bird *et al.* [54] on page 71, the term $\langle \boldsymbol{RR} \rangle$ is eliminated from the Kramers expression (3.26). First, equation (3.26) is multiplied by $\zeta/4H$ and then the upper convected time derivative is applied to the resulting expression, where the relation

$$\overset{\triangledown}{\boldsymbol{\delta}} = -2\mathbf{D} \tag{3.28}$$

is considered ([54], p. 71 and [15], p. 130). Next, by adding equation (3.27) to the resulting expression, the final expression is obtained as

$$\boldsymbol{\tau} + \lambda_H \overset{\triangledown}{\boldsymbol{\tau}} = 2\left(n_d k_B T \lambda_H + \eta_s\right)\mathbf{D} + 2\eta_s \lambda_H \overset{\triangledown}{\mathbf{D}}, \tag{3.29}$$

where $\lambda_H = \zeta/4H$ is the time constant of the Hookean dumbbells.
Introducing the definitions for the zero-shear-rate viscosity η_0, stress relaxation time λ_1 and the deformation retardation time λ_2 as per

$$\begin{aligned} \eta_0 &= \eta_s + n_d k_B T \lambda_H \\ \lambda_1 &= \lambda_H \\ \lambda_2 &= \frac{\eta_s}{\eta_s + n_d k_B T}\lambda_H = \frac{\eta_s}{\eta_0}\lambda_1 \end{aligned} \tag{3.30}$$

into equation (3.29), then the Oldroyd B model is obtained.

3.3 Different formulations of the Oldroyd-B model

In the previous sections, various forms of the Oldroyd-B model have been presented. Since the Oldroyd-B model is the investigated model in the present work, its different forms will be summarized here. All these forms are often used in the literature [11, 12, 55, 56]. Some of them have concrete physical meanings, while some of them are only designed for the purpose of numerical simulation [12].

- Basic form
  This form is formulated in terms of the total extra stress tensor τ as

$$\boldsymbol{\tau} + \lambda_1 \overset{\triangledown}{\boldsymbol{\tau}} = 2\eta_0 \left(\mathbf{D} + \lambda_2 \overset{\triangledown}{\mathbf{D}} \right), \tag{3.31}$$

  where λ_1 and λ_2 are independent material constants.

- Solvent-polymer stress splitting (SPSS)
  This is the most popular form in numerical simulations [11, 12]. The method was introduced by Bird *et al.* [3]. It formulates the equation in terms of the polymeric τ_p and solvent τ_s contributions to the extra stress:

$$\begin{aligned} \boldsymbol{\tau} &= \boldsymbol{\tau}_s + \boldsymbol{\tau}_p \\ \boldsymbol{\tau}_s &= 2\eta_s \mathbf{D} \\ \boldsymbol{\tau}_p + \lambda_1 \overset{\triangledown}{\boldsymbol{\tau}}_p &= 2\eta_p \mathbf{D} \end{aligned} \tag{3.32}$$

  where η_p and η_s are the polymer and solvent viscosities interrelated by ([3], p.360)

$$\eta_0 := \eta_p + \eta_s \quad \text{and} \quad \lambda_2 := \lambda_1 \frac{\eta_s}{\eta_p + \eta_s} = \lambda_1 \frac{\eta_s}{\eta_0}. \tag{3.33}$$

- Elasto-viscous stress splitting (EVSS)
  This form is neither derived from the continuum nor from the microstructure approach. It was introduced by Perera and Walters [57] for stable numerical simulation in order to solve the problem of the

absence of an explicit diffusive term in the basic Oldroyd-B model. The governing equations are formulated in terms of the Newtonian τ_n and elastic τ_e contributions to the extra stress [12]:

$$\begin{aligned} \boldsymbol{\tau} &= \boldsymbol{\tau}_n + \boldsymbol{\tau}_e \\ \boldsymbol{\tau}_n &= 2\eta_0 \mathbf{D} \\ \boldsymbol{\tau}_e + \lambda_1 \overset{\triangledown}{\boldsymbol{\tau}}_e &= -2\lambda_1 \eta_e \overset{\triangledown}{\mathbf{D}} \end{aligned} \tag{3.34}$$

where

$$\eta_e = \left(1 - \frac{\lambda_2}{\lambda_1}\right) \eta_0. \tag{3.35}$$

Both stress splitting approaches yield the same definition for the deformation retardation time as

$$\lambda_2 := \lambda_1 \frac{\eta_s}{\eta_p + \eta_s} = \lambda_1 \frac{\eta_s}{\eta_0} := \lambda_{2,EVSS} \tag{3.36}$$

3.4 Linear Viscoelasticity

The most general history-dependent linear viscoelastic model may be written in the following form [3, 4, 58]

$$\boldsymbol{\tau} = -\int_{-\infty}^{t} G(t-t')\dot{\boldsymbol{\gamma}}(t')\mathrm{d}t' \tag{3.37}$$

and

$$\boldsymbol{\tau} = +\int_{-\infty}^{t} M(t-t')\boldsymbol{\gamma}(t,t')\mathrm{d}t' \tag{3.38}$$

where $G(t-t')$ is the relaxation modulus, $M(t-t')$ is the memory function and

$$\boldsymbol{\gamma}(t,t') := \int_{t}^{t'} \dot{\boldsymbol{\gamma}}(t'')\mathrm{d}t''. \tag{3.39}$$

The memory function is defined as

$$M(t-t') = \frac{\partial G(t-t')}{\partial t'}. \tag{3.40}$$

The integrands in equations (3.37) and (3.38) consist of two functions. As explained in Bird et al. [3] (p.263), the first function, either $G(t-t')$ or $M(t-t')$, depends on the nature of the fluid and the second, either $\dot{\boldsymbol{\gamma}}(t,t')$ or $\boldsymbol{\gamma}(t')$, depends on the nature of the flow. Further, the expression (3.37) is essential for the linear oscillations experiments explained in section 5.2.2.

The next step is to find the expressions for the linear stress tensor and the relaxation modulus or memory function. This is achieved by linearization of the constitutive equations presented in the previous section (equations (3.4) - (3.7)), replacing the objective derivatives by partial time derivatives. A popular method to describe the linear viscoelastic behaviour is the introduction of one-dimensional *mechanical models*, which consist of springs and dashpots in different arrangements [4, 48, 59]. A spring represents a purely elastic (Hookean) behaviour, which is given by equation (1.2), while a dashpot represents a purely viscous (Newtonian) behaviour, which is described by equation (1.3). As noted in [59] on page 40, "*the correspondence between the behaviour of a model and a real material is achieved if the differential equation relating force, extension and time for the model is the same as that relating stress, strain and time for the material.*"

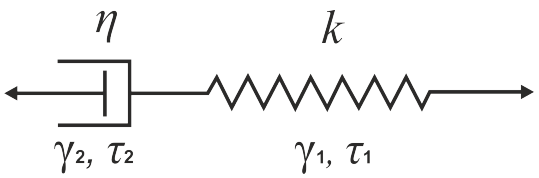

Figure 3.2: Maxwell element. Adapted from [59].

3.4.1 Linear Maxwell model

The UCM model (3.5) after linearization reduces to

$$\boldsymbol{\tau} + \lambda_1 \frac{\partial \boldsymbol{\tau}}{\partial t} = 2\eta_0 \mathbf{D}. \tag{3.41}$$

The mechanical analog of the linear Maxwell model is the Maxwell element (figure 3.2), which consists of a elastic spring and a purely viscous dashpot in series [4, 48, 59]. The stress in the spring is calculated by Hooke's law

$$\tau_1 = k\gamma_1 \tag{3.42}$$

where k is the elastic modulus and γ_1 is the strain of the spring. The stress τ_2 in the dashpot is

$$\tau_2 = \eta \frac{\partial \gamma_2}{\partial t} \tag{3.43}$$

where η is the viscosity and γ_2 is the strain of the dashpot. The spring and the dashpot are in series, therefore the stresses must be equal, that is $\tau_1 = \tau_2 = \tau$. The total strain γ, or equally the total strain-rate $\dot{\gamma}$, is the sum of the strains or the strain rates of the two elements, hence

$$\gamma = \gamma_1 + \gamma_2, \quad \dot{\gamma} = \dot{\gamma}_1 + \dot{\gamma}_2 \tag{3.44}$$

By combining equations (3.42)-(3.44), the Maxwell model is obtained as

$$\tau + \frac{\eta}{k}\dot{\tau} = \eta\dot{\gamma}. \tag{3.45}$$

After replacing $\dot{\gamma}$ with $2\boldsymbol{D}$ and η with η_0, and defining

$$\lambda_1 = \frac{\eta}{k} \tag{3.46}$$

as the relaxation time, the formal Maxwell model is obtained as in equation (3.41).
The integral form of the linear Maxwell equation may be written as

$$\boldsymbol{\tau}(t) = -\int_{-\infty}^{t} \left\{ \frac{\eta_0}{\lambda_1} \exp\left(-\frac{t-t'}{\lambda_1}\right) \right\} \dot{\boldsymbol{\gamma}}(t')\mathrm{d}t' \tag{3.47}$$

where the expression between the curled braces is identified as the relaxation modulus of the Maxwell model ([3], pp. 259-260). Integrating equation (3.47) by parts yields

$$\boldsymbol{\tau}(t) = +\int_{-\infty}^{t} \left\{ \frac{\eta_0}{\lambda_1^2} \exp\left(-\frac{t-t'}{\lambda_1}\right) \right\} \boldsymbol{\gamma}(t,t')\mathrm{d}t' \tag{3.48}$$

where the expression between the curled braces is identified as the memory function of the Maxwell model.

3.4.2 Linear Oldroyd-B (Jeffreys) model

The linearization of the Oldroyd-B model equation (3.7) leads to

$$\boldsymbol{\tau} + \lambda_1 \frac{\partial \boldsymbol{\tau}}{\partial t} = \eta_0 \left(\dot{\boldsymbol{\gamma}} + \lambda_2 \frac{\partial \dot{\boldsymbol{\gamma}}}{\partial t} \right), \tag{3.49}$$

which is known as the Jeffreys model.

The mechanical analog of the Jeffreys model is the Jeffreys element (see figure 3.3), obtained by extending the Maxwell element. The Maxwell model may be extended either by adding a second dashpot with viscosity η_2 parallel to the spring (figure 3.3(a)), or by adding a second dashpot with viscosity η_2 parallel to the Maxwell model (see figure 3.3(b)) ([59], pp. 42-43). The combination of the dashpot and spring in parallel is known as the Voigt element [4].

For the case depicted in figure 3.3(a), the total strain γ in a Jeffreys element is the sum of the strains in the Voigt element γ_2 and the dashpot γ_1, thus

$$\gamma = \gamma_1 + \gamma_2 \quad \text{and} \quad \dot{\gamma} = \dot{\gamma}_1 + \dot{\gamma}_2. \tag{3.50}$$

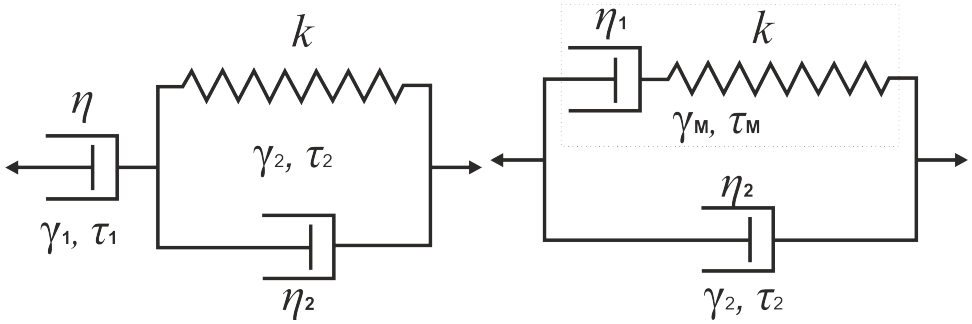

Figure 3.3: Jeffreys element obtained as an extension of the Maxwell model (a) by adding a second dashpot η_2 parallel to the spring or (b) by adding a second dashpot η_2 parallel to the Maxwell model. Adapted from [59].

The stresses in both elements are the same, hence

$$k\gamma_2 + \eta_2\dot{\gamma}_2 = \eta\dot{\gamma}_1 = \tau. \tag{3.51}$$

Eliminating γ_1 and γ_2 leads to the Jeffreys model in the form

$$\tau + \frac{\eta + \eta_2}{k}\dot{\tau} = \eta\left(\dot{\gamma} + \frac{\eta_2}{k}\ddot{\gamma}\right). \tag{3.52}$$

With the new definitions for the relaxation time

$$\lambda_1 := \frac{\eta + \eta_2}{k} \tag{3.53}$$

and for the retardation time

$$\lambda_2 := \frac{\eta_2}{k} = \frac{\eta_2}{\eta + \eta_2}\lambda_1, \tag{3.54}$$

the Jeffreys model is recovered as

$$\boldsymbol{\tau} + \lambda_1\frac{\partial\boldsymbol{\tau}}{\partial t} = \eta\left(\dot{\gamma} + \lambda_2\frac{\partial\dot{\gamma}}{\partial t}\right). \tag{3.55}$$

Similar calculation can be made for the case depicted in figure 3.3(b). The displacement γ_2 in the viscous dashpot with viscosity η_2 is equal to the

displacement in the Maxwell element γ_M. The total stress τ is the sum of the stress in the Maxwell element τ_M and the stress in the viscous dashpot $\tau_2 = \eta_2 \dot{\gamma}_2$

$$\tau = \tau_2 + \tau_M = \eta_2 \dot{\gamma}_2 + \tau_M \quad \text{with} \quad \tau_M + \lambda_1 \dot{\tau}_M = \eta_1 \dot{\gamma}_M. \tag{3.56}$$

After eliminating τ_M, the following form is derived

$$\tau + \lambda_1 \dot{\tau} = (\eta_1 + \eta_2) \left(\dot{\gamma} + \lambda_1 \frac{\eta_2}{\eta_1 + \eta_2} \frac{\partial \dot{\gamma}}{\partial t} \right). \tag{3.57}$$

By introducing the new definitions for the total viscosity η_0 and for the retardation time λ_2 as

$$\eta_0 := \eta_1 + \eta_2 \quad \text{and} \quad \lambda_2 := \frac{\eta_2}{\eta_1 + \eta_2} \lambda_1 = \frac{\eta_2}{\eta_0} \lambda_1 \tag{3.58}$$

the original Jeffreys model, given by equation (3.49), is recovered.

The integral form of the linear Jeffreys model may be written as

$$\boldsymbol{\tau}(t) = - \int_{-\infty}^{t} \left\{ \frac{\eta_0}{\lambda_1} \left(1 - \frac{\lambda_2}{\lambda_1} \right) \exp \left(- \frac{t - t'}{\lambda_1} \right) + 2 \frac{\eta_0 \lambda_2}{\lambda_1} \delta(t - t') \right\} \dot{\boldsymbol{\gamma}}(t') \mathrm{d}t' \tag{3.59}$$

where the expression between the curled braces is identified as the relaxation modulus of the Jeffreys model. Integrating equation (3.59) by parts yields

$$\boldsymbol{\tau}(t) = - \int_{-\infty}^{t} \left\{ \frac{\eta_0}{\lambda_1^2} \left(1 - \frac{\lambda_2}{\lambda_1} \right) \exp \left(- \frac{t - t'}{\lambda_1} \right) + 2 \frac{\eta_0 \lambda_2}{\lambda_1} \frac{\partial}{\partial t'} \delta(t - t') \right\} \boldsymbol{\gamma}(t, t') \mathrm{d}t' \tag{3.60}$$

where the expression between the curled braces is identified as the memory function of the Jeffreys model.

In the present case, studying the damped shape oscillations of a spherical viscoelastic drop, the time dependency of motion is described by an exponential function of time. Thus, the stress tensor and the strain rate tensor in spherical coordinates may be formulated as ([60], p. 4)

$$\boldsymbol{\tau} = \hat{\boldsymbol{\tau}}(r, \theta, \varphi) \mathrm{e}^{-\alpha t} \tag{3.61}$$

and

$$\dot{\gamma} = \hat{\dot{\gamma}}(r, \theta, \varphi) \mathrm{e}^{-\alpha t}, \tag{3.62}$$

respectively. There α is the complex angular frequency and $\hat{\boldsymbol{\tau}}(r, \theta, \varphi)$ and $\hat{\dot{\gamma}}(r, \theta, \varphi)$ are the amplitude functions of the stress tensor and the strain rate tensor, respectively. Inserting the expressions (3.61) and (3.62) into the Jeffreys model (3.49) results in

$$\boldsymbol{\tau} = \eta_0 \frac{1 - \alpha\lambda_2}{1 - \alpha\lambda_1} \dot{\gamma} := \eta(\alpha) \dot{\gamma}, \tag{3.63}$$

where $\eta(\alpha)$ is the frequency dependent dynamic viscosity. Drop shape oscillations may be used for determining material parameters in these equations [13, 14].

4 Linear drop shape oscillations

Droplet dynamics is one of the classical problems in fluid mechanics. Until recently [13, 60, 61], the only analytical solution found for this problem is the linear theory of small amplitude oscillations of inviscid [25] and viscous droplets [28, 29, 62, 63]. The results of the linear theory, that is the angular frequency and decay rate of viscous liquid drop oscillations, were already presented in the Introduction. In this chapter, a study of small-amplitude shape oscillations of a viscoelastic liquid drop in air, based on the linear theory, is presented.

In the first part, the mathematical formulation of the problem is given and the characteristic equation of the drop is derived. The dimensional analysis of the characteristic equation is conducted, and the ranges of the non-dimensional parameters (the Ohnesorge and the Deborah numbers) for which shape oscillations exist are determined. Next, the steps necessary for solving the characteristic equation for the unknown deformation retardation time are given.

4.1 Mathematical derivation

The mathematical description follows the works of Brenn and Teichtmeister [13] and Brenn [60]. Let us consider a spherical drop with equilibrium radius a which undergoes damped shape oscillations with frequency f and damping rate $\alpha_{m,r}$. The shape of the oscillating drop $r_s(\theta, t)$, shown in Figure 4.1, formulated in spherical coordinates, assuming symmetry in the azimuthal direction φ, is given by an infinite series of the surface spherical

harmonics as

$$r_s(\theta, t) = a\left(1 + \sum_{m=2}^{\infty} a_m P_m(\cos\theta) e^{-\alpha_m t}\right) \tag{4.1}$$

where a_m are the initial oscillation amplitudes, P_m are the Legendre polynomials and $\alpha_m = \alpha_{m,r} + i2\pi f$ is the complex angular frequency of mode m and $i = \sqrt{-1}$ [26, 64]. The summation in (4.1) starts with the fundamental mode $m = 2$ as $m = 0$ describes a volumetric pulsation and $m = 1$ a translatory motion of the drop. According to the equation for the decay time (1.10), the damping increases with increasing mode number as $\mathrm{O}(m^2)$, and, consequently, the higher oscillation modes are damped faster. Therefore, the droplet oscillations described by equation (4.1) may in practice be limited to the first few oscillation modes. The first three modes of oscillations for $m \geq 2$ are shown in figure 1.3.

The linear theory is expected to hold if the initial oscillation amplitude is less than 10% of the equilibrium drop radius [26]. In the linear approximation, the different oscillation modes are uncoupled and can be treated separately from each other [63]. Further, in the case of small initial amplitude, the dominant mode of oscillation is the fundamental mode $m = 2$, as was shown in [64]. Therefore, the general equation (4.1) can be simplified by omitting the summation symbol and the following equation with just one oscillation mode is obtained

$$r_s(\theta, t) = a + \epsilon_0 P_m(\cos\theta) e^{-\alpha_m t}. \tag{4.2}$$

where ϵ_0 is the initial oscillation amplitude [13, 14, 60–63]. The time dependency of motion is therefore known and is given by the exponential function $\exp(-\alpha_m t)$.

The equations governing the problem are the continuity equation (2.21) and the momentum equation (2.23) formulated in spherical coordinates assuming symmetry in the azimuthal direction φ. The continuity equation for incompressible liquid

$$\boldsymbol{\nabla} \cdot \boldsymbol{u} = 0 \tag{4.3}$$

is in spherical coordinates for the axisymmetric case given as

$$\frac{1}{r^2}\frac{\partial}{\partial r}\left(r^2 u_r\right) + \frac{1}{r\,\sin\theta}\frac{\partial}{\partial\theta}\left(u_\theta \sin\theta\right) = 0 \tag{4.4}$$

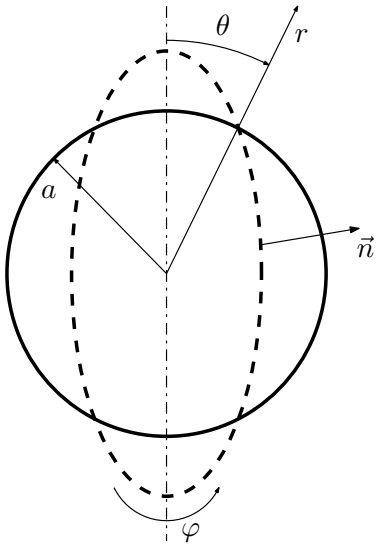

Figure 4.1: Equilibrium (solid line) and deformed (dashed line) drop shape in spherical coordinate system for $m = 2$ [13].

The momentum balance equation is given as

$$\rho \left(\frac{\partial}{\partial t} + \boldsymbol{u} \cdot \boldsymbol{\nabla} \right) \boldsymbol{u} = \nabla \cdot \boldsymbol{\pi} + \rho \boldsymbol{f}^B \tag{4.5}$$

where $\boldsymbol{\pi}$ is the stress tensor and $\rho \boldsymbol{f}^B$ are the body forces. The stress tensor $\boldsymbol{\pi}$ can be written as

$$\boldsymbol{\pi} = -p\boldsymbol{\delta} + \boldsymbol{\tau} \tag{4.6}$$

where p is the pressure and $\boldsymbol{\tau}$ is the extra stress tensor representing the deformation induced stresses. The extra stress tensor $\boldsymbol{\tau}$ is determined from the linear Oldroyd-B constitutive equation (3.49) assuming the fluid motion is known. Introducing the time dependency of shear stress and shear rate tensor, which are, according to equations (3.61) and (3.62), given as

$$\boldsymbol{\tau} \propto \mathrm{e}^{-\alpha_m t} \quad \text{and} \quad \dot{\boldsymbol{\gamma}} \propto \mathrm{e}^{-\alpha_m t}, \tag{4.7}$$

into the linear Oldroyd-B equation (3.49) results in the deformation-induced stress as

$$\boldsymbol{\tau} = \eta_0 \frac{1 - \alpha_m \lambda_2}{1 - \alpha_m \lambda_1} \dot{\boldsymbol{\gamma}} := \eta(\alpha_m) \dot{\boldsymbol{\gamma}}, \tag{4.8}$$

where $\eta(\alpha_m)$ is the complex frequency (of the oscillation mode m) dependent dynamic viscosity. The expression (4.8) is therefore formally identical to that of a Newtonian fluid (1.3) formulated with a complex viscosity.

After neglecting the body forces $\rho \boldsymbol{f}^B$ and nonlinear inertial terms, the momentum equation reads

$$\rho \frac{\partial \boldsymbol{u}}{\partial t} = -\boldsymbol{\nabla} \cdot (p\boldsymbol{\delta} - \boldsymbol{\tau}) . \tag{4.9}$$

The linearized momentum equation (4.9) in spherical coordinates for the axisymmetric case in the radial direction reads

$$\rho \frac{\partial u_r}{\partial t} = -\frac{\partial p}{\partial r} + \eta(\alpha_m) \left[\frac{1}{r^2} \frac{\partial^2}{\partial r^2} \left(r^2 u_r \right) + \frac{1}{r^2 \sin\theta} \frac{\partial}{\partial \theta} \left(\sin\theta \frac{\partial u_r}{\partial \theta} \right) \right] \tag{4.10}$$

and in the angular direction is given as

$$\begin{aligned} \rho \frac{\partial u_\theta}{\partial t} = & -\frac{1}{r} \frac{\partial p}{\partial \theta} + \\ & + \eta(\alpha_m) \left[\frac{1}{r^2} \frac{\partial^2}{\partial r^2} \left(r^2 \frac{\partial u_\theta}{\partial r} \right) + \frac{1}{r^2} \frac{\partial}{\partial \theta} \left(\frac{1}{\sin\theta} \frac{\partial}{\partial \theta} \left(u_\theta \sin\theta \right) \right) + \frac{2}{r^2} \frac{\partial u_r}{\partial \theta} \right] . \end{aligned} \tag{4.11}$$

The velocity field is formulated by the Stokes stream function ψ as

$$u_r = -\frac{1}{r^2 \sin\theta} \frac{\partial \psi}{\partial \theta} \tag{4.12}$$

and

$$u_\theta = \frac{1}{r \sin\theta} \frac{\partial \psi}{\partial r} . \tag{4.13}$$

Introducing definitions (4.12) and (4.13) into the momentum equations and taking the curl of the resulting equation

$$\boldsymbol{\nabla} \times \begin{pmatrix} r - momentum \\ \theta - momentum \\ 0 \end{pmatrix} = \boldsymbol{0} \tag{4.14}$$

which eliminates the pressure gradient, results in the partial differential equation of the fourth-order

$$\frac{\rho}{\eta\left(\alpha_m\right)}\frac{\partial}{\partial t}\left(E^2\psi\right) = E^2\left(E^2\psi\right) \tag{4.15}$$

with the differential operator

$$E^2 = \frac{\partial^2}{\partial r^2} + \frac{\sin\theta}{r^2}\frac{\partial}{\partial\theta}\left(\frac{1}{\sin\theta}\,\frac{\partial}{\partial\theta}\right). \tag{4.16}$$

The operators $\frac{\rho}{\eta(\alpha_m)}\frac{\partial}{\partial t}$, $\frac{\rho}{\eta(\alpha_m)}\frac{\partial}{\partial t} + E^2$ and E^2 are commutative with each other, that is, changing the order of operands does not change the result. Therefore, equation (4.15) can be rewritten as

$$\left(-\frac{\rho}{\eta\left(\alpha_m\right)}\frac{\partial}{\partial t} + E^2\right)\left(E^2\psi\right) = 0 \tag{4.17}$$

or equivalently

$$E^2\left[\left(-\frac{\rho}{\eta\left(\alpha_m\right)}\frac{\partial}{\partial t} + E^2\right)\psi\right] = 0 \tag{4.18}$$

That allows that the solution ψ of equation (4.17) can be found with the ansatz [65]

$$\psi = \psi_1 + \psi_2 \tag{4.19}$$

where ψ_1 solves the equation

$$E^2\psi_1 = 0 \tag{4.20}$$

and ψ_2 solves the equation

$$\left(-\frac{\rho}{\eta\left(\alpha_m\right)}\frac{\partial}{\partial t} + E^2\right)\psi_2 = 0 \tag{4.21}$$

The method of separation of variables is used to find the solutions of the equations (4.20) and (4.21). The appropriate ansatz for ψ_1 is

$$\psi_1 = f_1\left(r\right)g_1\left(\theta\right)e^{-\alpha_m t} \tag{4.22}$$

and equation (4.20) now reads

$$g_1(\theta)\frac{\partial^2 f_1(r)}{\partial r^2} + f_1(r)\frac{\sin\theta}{r^2}\frac{\partial}{\partial\theta}\left(\frac{1}{\sin\theta}\frac{\partial g_1(\theta)}{\partial\theta}\right) = 0 \tag{4.23}$$

or equivalently

$$r^2\frac{f_1''}{f_1} = -\frac{\sin\theta}{g_1}\frac{\partial}{\partial\theta}\left(\frac{1}{\sin\theta}g_1'\right) \tag{4.24}$$

The left-hand side of equation (4.24) can only be a function of the radial coordinate (r) and the right hand-side can only be a function of the angular coordinate (θ); this leads to the conclusion that equation (4.24) is satisfied if both sides of the equation are constant. Let this constant be equal to $m(m+1)$. The left-hand side of equation (4.24) can now be written as

$$r^2\frac{f_1''}{f_1} = m(m+1) \tag{4.25}$$

which has the form of the Euler differential equation with the solution

$$f_1(r) = A_1 r^{-m} + A_2 r^{m+1} \tag{4.26}$$

where A_1 and A_2 are unknown constants. The expression $A_1 r^{-m}$ for positive m diverges for $r \to 0$. Therefore the constant A_1 must be set to zero

$$A_1 = 0 \tag{4.27}$$

The right-hand side of equation (4.24) is also equal to $m(m+1)$

$$-\frac{\sin\theta}{g_1}\frac{\partial}{\partial\theta}\left(\frac{1}{\sin\theta}g_1'\right) = m(m+1) \tag{4.28}$$

Introducing a new function $\tilde{g}$ defined through

$$g_1(\theta) = \tilde{g}(\cos\theta), \quad \text{so that} \quad g_1' = -\tilde{g}'\sin\theta,\ g_1'' = -\tilde{g}''\sin^2\theta - \tilde{g}'\cos\theta \tag{4.29}$$

into equation (4.28) results in

$$\tilde{g}''\left(1-\cos^2\theta\right) + m(m+1)\tilde{g} = 0 \tag{4.30}$$

which is a special case of the Legendre differential equation. The solutions to this kind of equation are combinations of Legendre functions of the first P_m and the second kinds Q_m (with the argument $\cos\theta$)

$$g_1 = \tilde{g} = A_3 P'_m(\cos\theta)\sin^2\theta + A_4 Q'_m(\cos\theta)\sin^2\theta \tag{4.31}$$

The Legendre function of the second kind $Q_m(\cos\theta)$ and its derivative $Q'_m(\cos\theta)$ diverge for $\cos\theta \to 1$. Therefore the constant A_4 must be set to zero

$$A_4 = 0. \tag{4.32}$$

The function ψ_1 can now be written as

$$\psi_1 = A_2 r^{m+1} \cdot A_3 \sin^2\theta \cdot P'_m(\cos\theta) \cdot e^{-\alpha_m t}. \tag{4.33}$$

Introducing the ansatz

$$\psi_2 = f_2(r)\, g_2(\theta) \cdot e^{-\alpha_m t} \tag{4.34}$$

into equation (4.21) yields

$$\frac{\rho\alpha_m}{\eta(\alpha_m)} f_2(r)\, g_2(\theta) + g_2(\theta)\frac{\partial^2 f_2(r)}{\partial r^2} + f_2(r)\frac{\sin\theta}{r^2}\frac{\partial}{\partial\theta}\left(\frac{1}{\sin\theta}\frac{\partial g_2(\theta)}{\partial\theta}\right) = 0 \tag{4.35}$$

and after rearrangement

$$\frac{\rho\alpha_m}{\eta(\alpha_m)} r^2 + \frac{r^2}{f_2(r)}\frac{\partial^2 f_2(r)}{\partial r^2} = -\frac{\sin\theta}{g_2(\theta)}\frac{\partial}{\partial\theta}\left(\frac{1}{\sin\theta}\frac{\partial g_2(\theta)}{\partial\theta}\right). \tag{4.36}$$

The left and right-hand sides of equation (4.36) must be a constant, for the same reasons as mentioned above, and the constant is again set to $m(m+1)$. From comparison of the right-hand side of equation (4.36) with equation (4.28) it is clear that

$$g_2 = g_1 = A_3 P'_m(\cos\theta)\sin^2\theta. \tag{4.37}$$

Setting the left-hand side of equation (4.36) equal to m(m+1), and after rearrangement, the following equation is obtained

$$r^2 f_2'' + \left(\frac{\alpha_m}{\nu(\alpha_m)} r^2 - m(m+1)\right) f_2 = 0. \tag{4.38}$$

Introducing a function $\tilde{f}$ defined through

$$f_2(r) = \tilde{f}\left(r\sqrt{\frac{\alpha_m}{\nu}}\right) \ , \ f_2'(r) = \sqrt{\frac{\alpha_m}{\nu}}\tilde{f}' \ \text{ and } \ f_2''(r) = \frac{\alpha_m}{\nu}\tilde{f}'' \tag{4.39}$$

into equation (4.38) yields the Riccati-Bessel equation

$$z^2\tilde{f}''(z) + \left(z^2 - m(m+1)\right)\tilde{f}(z) = 0 \tag{4.40}$$

where $z = r\sqrt{\alpha_m/\nu}$. The solutions of the Riccati-Bessel equation (4.40) are the spherical Bessel functions of the first $j_m(z)$ and the second kinds $y_m(z)$ of the order m

$$\tilde{f}(z) = A_5 \cdot z j_m(z) + A_6 \cdot z y_m(z). \tag{4.41}$$

The solution of the (4.38) can be written as

$$f_2(r) = A_5 \cdot qr j_m(qr) + A_6 \cdot qr y_m(qr) \tag{4.42}$$

where the parameter q is defined as

$$q = \sqrt{\frac{\alpha_m}{\nu(\alpha_m)}}. \tag{4.43}$$

The spherical Bessel function of the second kind $y_m(qr)$ diverges for $r \to 0$, more strongly that qr goes to zero. Therefore the constant A_6 must be set to zero

$$A_6 = 0 \tag{4.44}$$

The function ψ_2 can now be written as

$$\psi_2 = A_5 \cdot qr j_m(qr) \cdot A_3 \sin^2\theta \cdot P_m'(\cos\theta) \cdot e^{-\alpha_m t}. \tag{4.45}$$

Finally, the Stokes stream function ψ may be written as

$$\psi = \left(A_2 r^{m+1} + A_5 \cdot qr j_m(qr)\right) \cdot A_3 \sin^2\theta \cdot P_m'(\cos\theta) \cdot e^{-\alpha_m t} \tag{4.46}$$

The constants A_2 and A_3 can be combined as $C_1 = A_2 \cdot A_3$ and the constants A_3 and A_5 can be combined as $C_2 = A_3 \cdot A_5$. This yields the following equation

$$\psi = \left(C_1 r^{m+1} + C_2 \cdot qr j_m(qr)\right) \cdot \sin^2\theta \cdot P'_m(\cos\theta) \cdot e^{-\alpha_m t} \tag{4.47}$$

The resulting radial and angular velocity components, given by the equations (4.12) and (4.13), now read

$$u_r = -\left(C_1 r^{m-1} + C_2 q^2 \frac{j_m(qr)}{qr}\right) m(m+1) P_m \cdot e^{-\alpha_m t} \tag{4.48}$$

and

$$u_\theta = \left[C_1(m+1) r^{m-1} + C_2 q^2 \left((m+1)\frac{j_m(qr)}{qr} - j_{m+1}(qr)\right)\right] \cdot \cdot \sin\theta P'_m \cdot e^{-\alpha_m t} \tag{4.49}$$

The constants C_1 and C_2 are determined by the kinematic and dynamic boundary conditions.

The kinematic boundary condition states that the radial velocity component at the equilibrium drop radius $r = a$ equals the rate of the radial displacement of the deformed surface of the oscillating drop, that is,

$$u_r|_{r=a} = \frac{\partial r_S}{\partial t} \tag{4.50}$$

The dynamic boundary condition for the drop in a gas states that the shear stress at the drop surface, calculated at $r = a$, is zero

$$\left(\frac{1}{r}\frac{\partial u_r}{\partial \theta} + r\frac{\partial\left(u_\theta / r\right)}{\partial r}\right)\Bigg|_{r=a} = 0 \tag{4.51}$$

From the above mentioned boundary conditions the two integration constants are obtained as

$$C_{1,m} = \frac{\varepsilon_0 \alpha_m}{m(m+1) a^{m-1}} \left(1 + \frac{2\left(m^2-1\right)}{2qa\,\frac{j_{m+1}(qa)}{j_m(qa)} - q^2 a^2}\right) \tag{4.52}$$

and

$$C_{2,m} = -\frac{2\,(m-1)\,\varepsilon_0 \alpha_m a}{mq\,(2qa\;j_{m+1}\,(qa) - q^2 a^2 j_m\,(qa))} \tag{4.53}$$

The subscript m denotes the mode-dependency of the calculated constants.

The dynamic boundary condition for the normal stress reveals the characteristic equation for the complex angular frequency α_m of the drop. To obtain this normal-stress boundary condition, the capillary pressure inside the undeformed drop p_0 and deformed drop p_σ, and the pressure field p inside the drop must be known. The normal-stress boundary condition states that the (r,r) component of the total stress tensor $\boldsymbol{\pi}_{r,r}$ must be zero at the drop surface

$$\boldsymbol{\pi}_{r,r} = -p - (p_0 - p_\sigma) + \boldsymbol{\tau}_{rr} \tag{4.54}$$

where $\boldsymbol{\tau}_{rr}$ is the (r,r) component of the viscoelastic extra stress tensor defined as

$$\boldsymbol{\tau}_{rr} = 2\eta\,(\alpha_m)\,\frac{\partial u_r}{\partial r}. \tag{4.55}$$

With the known velocity field inside the drop, the normal extra stress at $r = a$ is calculated as

$$\begin{aligned}\boldsymbol{\tau}_{rr}|_{r=a} &= 2\eta\,(\alpha_m)\,\left.\frac{\partial u_r}{\partial r}\right|_{r=a} = \\ &-2\eta\left((m-1)\,C_1 a^{m-2} + C_2 q^3\,\frac{(m-1)\,j_m\,(qa) - qa j_{m+1}\,(qa)}{q^2 a^2}\right)\cdot \\ &\qquad\qquad \cdot m\,(m+1)\,P_m \cdot e^{-\alpha_m t}\end{aligned} \tag{4.56}$$

The capillary pressure inside the undeformed drop is given as

$$p_0 = \frac{2\sigma}{a} \tag{4.57}$$

and the capillary pressure for the deformed drop is calculated as

$$p_\sigma = \sigma \boldsymbol{\nabla} \cdot \boldsymbol{n} \tag{4.58}$$

where

$$\boldsymbol{\nabla} \cdot \boldsymbol{n} = \boldsymbol{\nabla} \cdot \left(\frac{\boldsymbol{\nabla} F}{|\boldsymbol{\nabla} F|}\right) \tag{4.59}$$

is the curvature of the drop and the function F describes the free surface of the drop

$$F = r - a - r_s(\theta, t) = r - a - \varepsilon_0 P_m(\cos\theta) \cdot e^{-\alpha_m t}. \tag{4.60}$$

For small oscillation amplitudes, the capillary pressure inside the deformed drop is given as [28]

$$p_\sigma = \frac{\sigma}{a}\left(2 + (m-1)(m+2)\frac{\varepsilon_0}{a} P_m(\cos\theta) \cdot e^{-\alpha_m t}\right). \tag{4.61}$$

Introducing the expression (4.12) into the radial momentum balance equation (4.10), and considering (4.20) and (4.21), yields the radial derivative of the pressure as

$$\frac{\partial p}{\partial r} = -\frac{\rho\alpha_m}{r^2 \sin\theta}\frac{\partial \psi_1}{\partial \theta}. \tag{4.62}$$

The pressure field is obtained by integration of equation (4.62) and reads

$$p = -(m+1) C_{1,m} \rho \alpha_m r^m P_m(\cos\theta) \cdot e^{-\alpha_m t}, \tag{4.63}$$

with the integration constant set to zero ([60], pp. 143-144). Using the θ momentum balance equation (4.11) produces the same result [60].

Inserting the expressions for p_σ, p_0, p and $\boldsymbol{\tau}_{rr}$ into the normal-stress boundary condition, the characteristic equation for the complex angular frequency α_m of the drop is obtained

$$\frac{\alpha_{m,0}^2}{\alpha_m^2} = \frac{2\left(m^2-1\right)}{q^2a^2 - 2qa\frac{j_{m+1}(qa)}{j_m(qa)}} - 1 + \frac{2m(m-1)}{q^2a^2}\left(1 + \frac{2(m+1)\frac{j_{m+1}(qa)}{j_m(qa)}}{2\frac{j_{m+1}(qa)}{j_m(qa)} - qa}\right) \tag{4.64}$$

where $\alpha_{m,0}$ is given by (1.12). The derived characteristic equation is formally identical to the results of Lamb [27] and Chandrasekhar ([62], p. 472) obtained for Newtonian liquids. In the present case of viscoelastic liquids, however, the dynamic viscosity $\eta(\alpha_m)$ involved in the equation is a function of the complex oscillation frequency α_m. From the definition of the parameter q (4.43) follows that the complex argument of the spherical Bessel functions qa can be written as

$$qa = a\sqrt{\frac{\rho\alpha_m}{\eta_0}\frac{1-\lambda_1\alpha_m}{1-\lambda_2\alpha_m}}. \tag{4.65}$$

The characteristic equation (4.64), together with the definition of the argument qa (4.65), is the basis of the proposed method for measuring the deformation retardation time λ_2 of viscoelastic liquid described by the Jeffreys model (3.49).

4.2 Dimensional analysis of the characteristic equation

The present analysis of the characteristic equation of the viscoelastic drop is primarily based on the work of Brenn and Teichtmeister [13] and of Khismatullin and Nadim [61]. To analyze the characteristic equation (4.64), some non-dimensional quantities are introduced as

$$\Omega_m = \frac{\alpha_m}{\alpha_{m,0}}, \quad \mathrm{Oh} = \frac{\eta_0}{\sqrt{\sigma\rho a}}, \quad \mathrm{De}_1 = \alpha_{m,0}\lambda_1; \quad \mathrm{De}_2 = \alpha_{m,0}\lambda_2 \tag{4.66}$$

where Ω_m is the non-dimensional complex frequency, Oh is identified as the Ohnesorge number and De_1 and De_2 are the relaxation and retardation Deborah numbers formulated with λ_1 and λ_2, respectively. The complex argument of the spherical Bessel functions qa (4.65) involved in the characteristic equation may now be written as

$$qa = \sqrt{\sqrt{m(m-1)(m+2)}\,\frac{\Omega_m}{\mathrm{Oh}}\frac{1-\Omega_m\mathrm{De}_1}{1-\Omega_m\mathrm{De}_2}}\,. \tag{4.67}$$

The aim of this analysis is to determine the ranges of the non-dimensional parameters, given by equations (4.66), for which shape oscillations exist. The dimensional analysis was performed numerically for the first oscillation mode $m = 2$. As the initial assumptions, a drop with radius between $a = 0.8$ and $a = 1.2$ mm, density $\rho = 1000\,\mathrm{kg\,m^{-3}}$, surface tension $\sigma = 0.073\,\mathrm{N\,m^{-1}}$, maximum zero-shear rate viscosity $\eta_0 = 5\,\mathrm{Pa\,s}$ and the maximum stress relaxation time $\lambda_1 = 0.5$ s was considered. This results in a Rayleigh angular frequency of about $\alpha_{2,0} \approx 764\,\mathrm{rad\,s^{-1}}$, a maximum Ohnesorge number around $\mathrm{Oh} \approx 20$ and maximum Deborah number $\mathrm{De}_1 \approx 380$.
The solutions of the characteristic equation are searched in the form of the

non-dimensional complex frequency Ω_m as a function of the Ohnesorge number, with De_1 and De_2 as parameters.
In the first part of the present analysis $\mathrm{De}_2 = \mathrm{De}_1/10$ was set, similarly as in [13]. The corresponding results, the non-dimensional oscillation frequency $\mathrm{Im}(\Omega_m)$ and the non-dimensional damping rate $\mathrm{Re}(\Omega_m)$ as functions of the Ohnesorge number, are presented in figures 4.2(a) and (b), respectively. Figure 4.2(a) the non-dimensional frequency as a function of the Ohnesorge number. For the purely inelastic case ($\mathrm{De}_1 = 0$), the non-dimensional frequency $\mathrm{Im}(\Omega_m)$ decreases with increasing Ohnesorge number. A critical Ohnesorge number Oh^* can be identified for which $\mathrm{Im}(\Omega_m) = 0$. The shape oscillations exist only for the Ohnesorge numbers below Oh^*. Increasing the Ohnesorge number above Oh^*, two aperiodic decaying modes appear. For the Newtonian case ($\mathrm{De}_1 = 0$), the critical value $\mathrm{Oh}^*_{De_1=0} := \mathrm{Oh}^*_0 \approx 0.766$.
For values $De_1 > 0$, the value of Oh^* becomes larger than for the inelastic case Oh^*_0, and therefore a wider range of Ohnesorge numbers for drop shape oscillations exist. This range, however, becomes narrower with increasing liquid elasticity, keeping the ratio $\mathrm{De}_2/\mathrm{De}_1$ constant. In the limiting case, where De_1 goes to infinity, one can find that $\mathrm{Oh}^* \approx 7.66$. which is 10 times the value Oh^*_0, due to the constant ratio $\mathrm{De}_2/\mathrm{De}_1 = 1/10$ [13]. This can be verified by rewriting Oh^* as a function of De_1. Therefore, the constant zero-shear-rate viscosity η_0, occurring in the definition of the Ohnesorge number (4.66), is replaced with the expression for the frequency dependent viscosity $\eta(\alpha_m)$ given by equation (4.8). This leads to the following expression for the critical Ohnesorge number at large De_2

$$\lim_{\mathrm{De}_1 \to \infty} \mathrm{Oh}^* = \mathrm{Oh}^*_0 \cdot \frac{\mathrm{De}_2}{\mathrm{De}_1}. \tag{4.68}$$

Figure 4.2(b) depicts the non-dimensional damping rate as a function of the Ohnesorge number. For the inviscid case ($\mathrm{Oh} = 0$) the damping rate is zero, as expected. At the critical Ohnesorge number Oh^* the damping rate bifurcates into two branches; the upper branch corresponds to the fast decaying mode, while the lower branch corresponds to the creeping mode [13]. The appearance of the two modes of decay was reported also by Chandrasekhar [62] and Prosperetti [63] for the inelastic case.

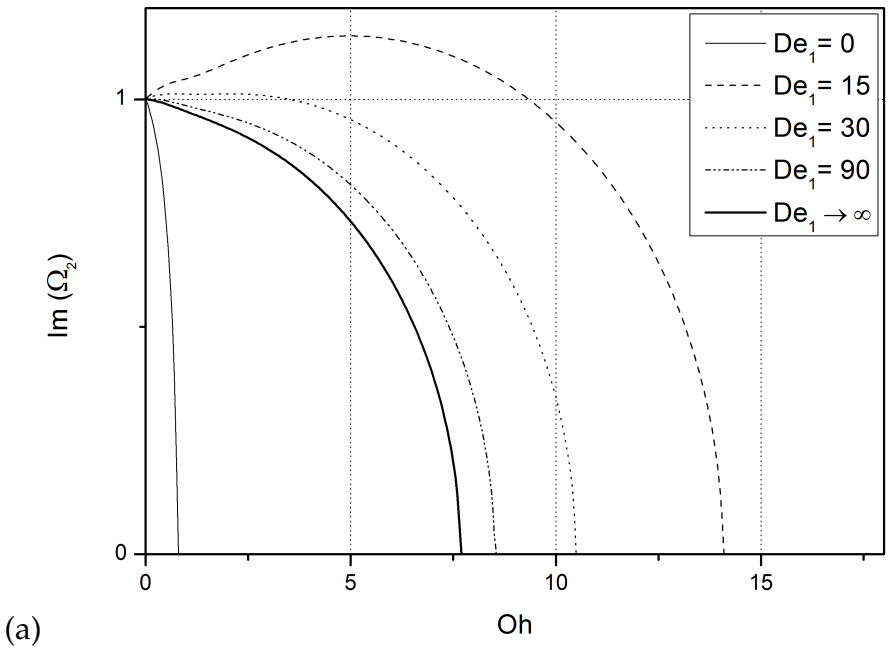

(a)

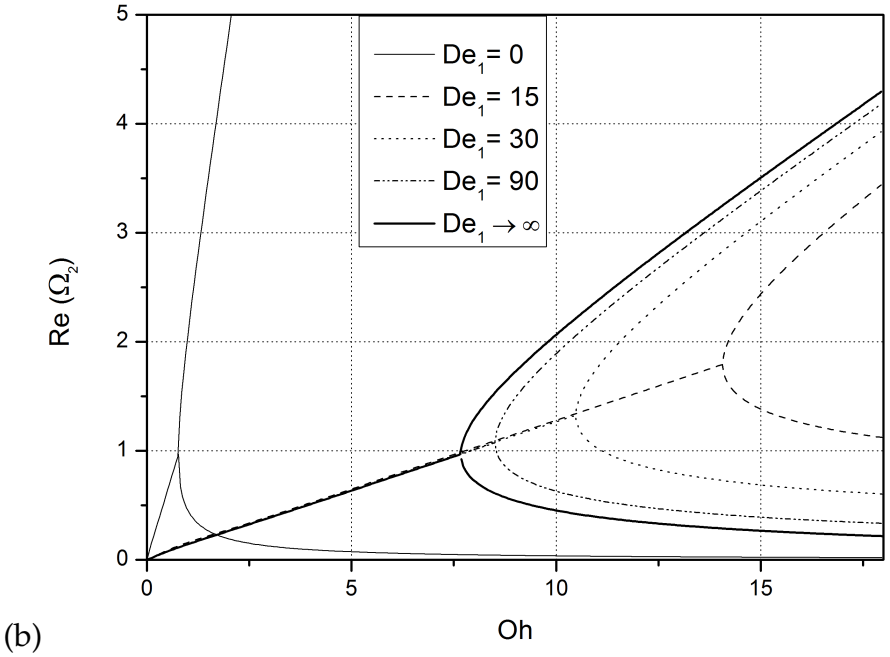

(b)

Figure 4.2: Non-dimensional (a) frequency $\mathrm{Im}(\Omega_m)$ and (b) damping rate $\mathrm{Re}(\Omega_m)$ as a function of the Ohnesorge number for different Deborah numbers De_1 for mode $m = 2$. The second Deborah number was set as $\mathrm{De}_2 = \mathrm{De}_1/10$.

Figure 4.3 demonstrates the validity of equation (4.68) for the critical Ohnesorge number for different values of De_2/De_1 as $De_1 \to \infty$. By decreasing De_2, the value of the critical Ohnesorge number increases according to equation (4.68), as expected.
The non-dimensional frequency, depicted in figure 4.3(a), shows the overall tendency to decrease monotonically with increasing Oh. The rate of decrease of the non-dimensional frequency with increasing Oh depends on the ratio De_2/De_1 and is faster for larger ratios De_2/De_1. For the lowest ratio De_2/De_1 in figure 4.3(a), the non-dimensional frequency slightly increases with Oh, reaches a maximum, and then slowly decreases.
The non-dimensional damping rate, shown in figure 4.3(b), shows similar behaviour as in figure 4.2(b). The non-dimensional damping rate increases with increasing Oh until the bifurcation point is reached, that is, for $Oh < Oh^*$. At $Oh = Oh^*$ the curves converge to $Re(\Omega_2) = 1$ asymptotically with decreasing ratio De_2/De_1. For $0 < Oh < 20$, which is the relevant range of Ohnesorge numbers in the present work, the non-dimensional damping rate decreases with decreasing values of De_2/De_1.

By further reducing De_2 and keeping De_1 constant at some reasonable value (say $De_1 = 50$), one interesting phenomenon is observed, which is not shown in figure 4.3, namely the branching of the non-dimensional frequency and damping rate for $Oh < Oh^*$. To exclude the possibility of a numerical error in solving the characteristic equation for the non-dimensional frequency, the following test was made. The calculated solutions of the characteristic equation were inserted back into the characteristic equation and the difference between the values on the left and right-hand sides of the equation were monitored. In the case that the calculated value is a correct solution of the characteristic equation, the values of the left and the right-hand sides of (4.64) should be equal. The calculated difference between values on the left and right-hand side of the equation should be in the order of the machine precision, which is the case in these calculations.
First the analysis for the limiting case $De_2 = 0$ is performed. The case presented in figure 4.4 with $De_1 = 50$ and $De_2 = 0$ corresponds to the Maxwell model, equation (3.41), with a single relaxation time. It must be mentioned that, for $Oh < 1$, it was practically impossible to find the complete set of solutions .

Figure 4.4(a) shows different branches of the non-dimensional frequency

as a function of the Ohnesorge number. Different branches correspond to different oscillation behaviour for the same set of parameters.
One of the solutions, the violet curve shown in figure 4.4(a), starts at $\mathrm{Im}(\Omega) = 1$, as expected from the previous analysis (figures 4.2(a) and 4.3(a)). For low values of Oh, the considered curve increases slowly with Oh, while for $\mathrm{Oh} > 2$ the increase of the curve is more rapid.
The other two solutions, the blue and yellow curves shown in figure 4.4(a), apparently start at $\mathrm{Im}(\Omega) = 0$, which is rather surprising. These two branches slowly increase with Oh.
The non-dimensional damping rate, shown in figure 4.3(b), also exhibits different branches. It will be interesting to compare the measured complex angular frequency with the behaviour shown in figure 4.4.

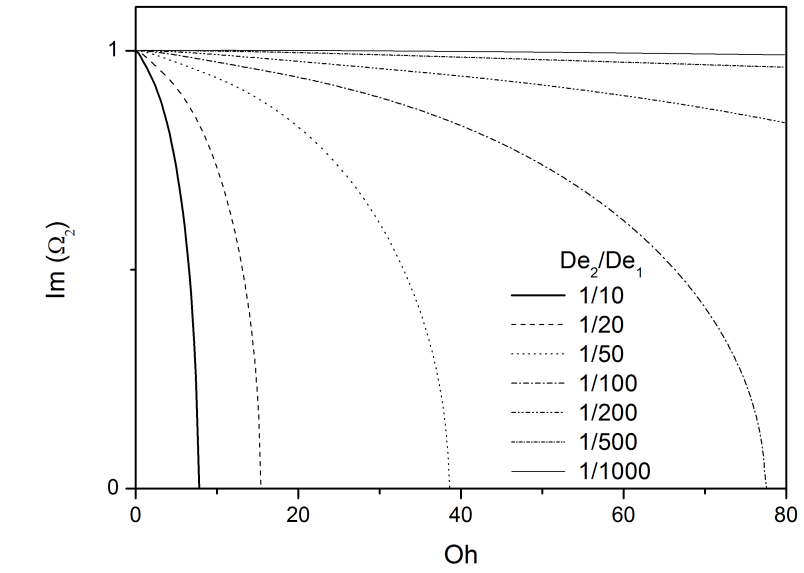

(a)

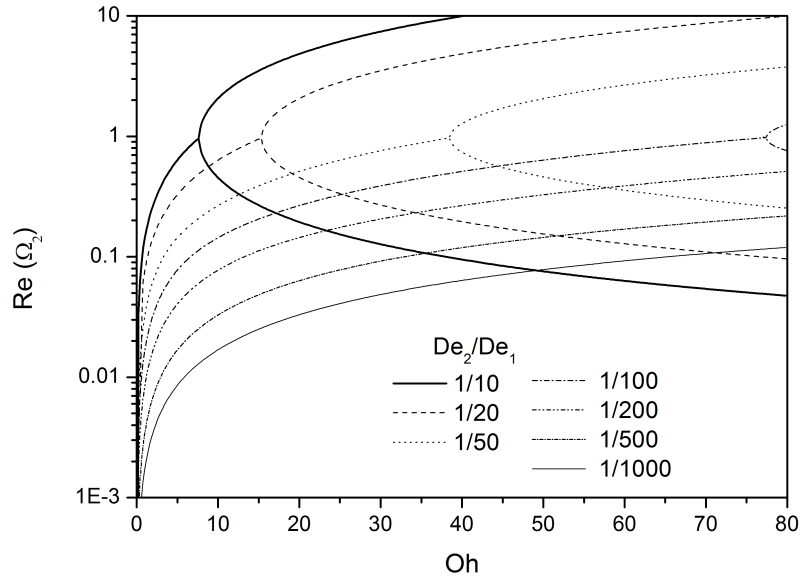

(b)

Figure 4.3: Non-dimensional (a) frequency $\mathrm{Im}(\Omega_2)$ and (b) damping rate $\mathrm{Re}(\Omega_2)$ as a function of the Ohnesorge number for $\mathrm{De}_1 \to \infty$ and different $\mathrm{De}_2/\mathrm{De}_1$.

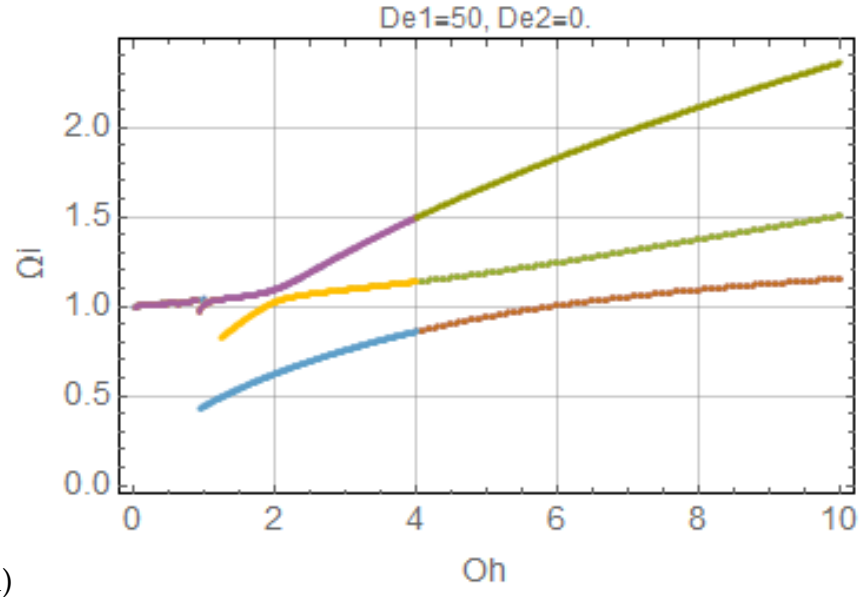

(a)

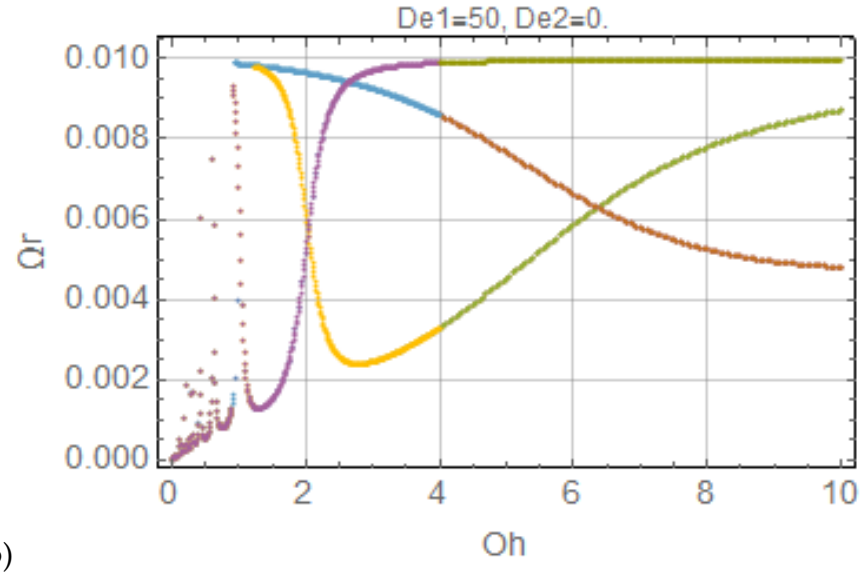

(b)

Figure 4.4: Non-dimensional (a) frequency $\Omega i = \mathrm{Im}(\Omega_m)$ and (b) damping rate $\Omega r = \mathrm{Re}(\Omega_m)$ as a function of the Ohnesorge number for $\mathrm{De}_1 = 50$, $\mathrm{De}_2 = 0$ and $m = 2$.

4.3 Solution of the characteristic equation

In Section 4.1 the characteristic equation (4.64) of the drop was derived. In this section, the analysis of the characteristic equation and the method for determining λ_2 by solving the characteristic equation is presented. This equation is transcendental in the argument of the spherical Bessel functions involved and cannot be solved analytically. The numerical solutions were obtained by using the computer software MATHEMATICA. In the last part of this section, the uncertainty and sensitivity analysis of the method is addressed.

4.3.1 Solving the characteristic equation

To analyze the characteristic equation (4.64), a complex function $F(qa)$ is introduced as per [14]

$$F(qa) = \frac{2\left(m^2-1\right)}{q^2a^2 - 2qa\frac{j_{m+1}(qa)}{j_m(qa)}} - 1 + \frac{2m\,(m-1)}{q^2a^2}\left(1 + \frac{2\,(m+1)\,\frac{j_{m+1}(qa)}{j_m(qa)}}{2\frac{j_{m+1}(qa)}{j_m(qa)} - qa}\right). \tag{4.69}$$

The function $F(qa)$ represents the right-hand side of the characteristic equation (4.64). The behaviour of the function (4.69) is examined for different values of its complex argument qa. The chosen values of qa cover the range of values important for the experiments with drops of viscoelastic liquids examined. The relevant values are taken from the preliminary experiments conducted by Brenn and Teichtmeister [13]. A drop with a radius of $O(1\text{ mm})$, density $O(1000\text{ kg m}^{-3})$, surface tension $O(0.075\text{ N m}^{-1})$, viscosity $O(0.5\text{ Pa s})$ and stress relaxation time $O(0.1\text{ s})$ is considered. For this drop, an oscillation frequency $O(130\text{ Hz})$ and damping rate $O(10\text{ s}^{-1})$ are expected. Figure 4.5a shows the real part of the function $F(qa)$ as a function of the real part of its argument qa, with the imaginary part of qa as a parameter. For values of the imaginary part of qa larger than 1, the real part of the function $F(qa)$ is a smooth and piecewise monotonic function. In contrast, for smaller values of the imaginary part of qa, the real part of the function $F(qa)$ is not a monotonic function, and for values of the imaginary

part of qa smaller than 0.1 the real part of the function $F(qa)$ displays sharp peaks. The examination of the imaginary part of the function $F(qa)$ gives the same results, as can be seen in Figure 4.5b.

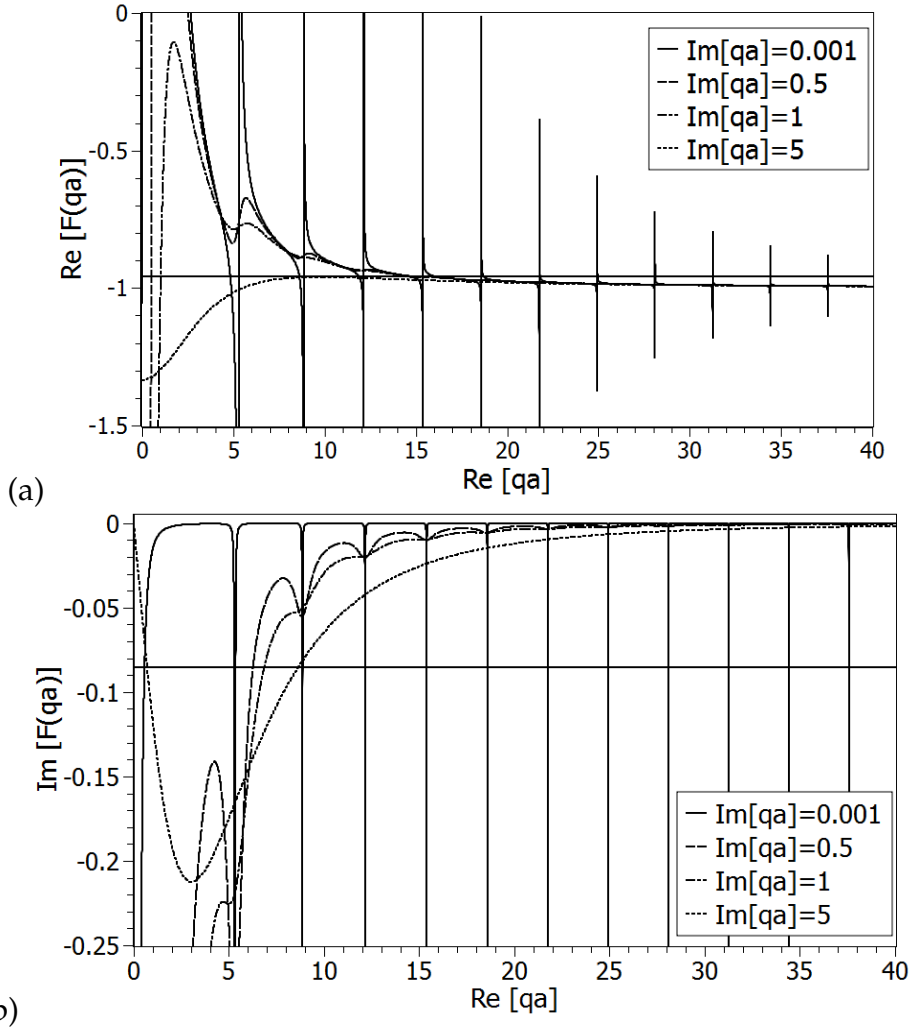

Figure 4.5: The function $F(qa)$ for different values of its argument qa in the basic oscillation mode $m = 2$. (a) The real and (b) the imaginary part of the function. The horizontal lines at $Re[F(qa)] = -0.95787$ and $Im[F(qa)] = -0.0855i$ represent the left-hand side of equation (4.69) for the 1.94 mm 0.3 $wt\%$ Praestol 2500 drop studied in [14].

4.3.2 Determination of the deformation retardation time

To determine the deformation retardation time λ_2 from the characteristic equation the quantities involved in the equation must all be accurately measured. These quantities are the complex frequency α_m of the oscillation mode $m = 2$, the equilibrium radius of the drop a, the density ρ and zero shear viscosity η_0, the surface tension σ of the liquid in contact with the ambient air, and the stress relaxation time λ_1.
With the calculated Rayleigh angular frequency $\alpha_{2,0}$ and the measured complex frequency α_2 of the fundamental oscillation mode $m = 2$, the left-hand side of the characteristic equation is known. The complex equation (4.64) is a system of two equations, and two quantities can be determined from it; the unknown deformation retardation time λ_2 and any other (known) quantity involved. The purpose of the second quantity will be explained later in the text.
With the argument qa for the fundamental mode $m = 2$ given as

$$qa = a\sqrt{\frac{\rho\alpha_2}{\eta_0}\frac{1-\alpha_2\lambda_1}{1-\alpha_2\lambda_2}} \tag{4.70}$$

and inserted into equation (4.64), it could in principle be possible to calculate the unknown deformation retardation time λ_2 from the characteristic equation directly. Unfortunately, the direct approach is not always possible, because the mathematical system is numerically unstable.
For this reason, the proposed method consists of three steps [14]:

1. First the argument qa solving the characteristic equation is determined. This is done by finding the roots of the equation

$$\frac{\alpha_{2,0}^2}{\alpha_2^2} = F(qa) \tag{4.71}$$

where $F(qa)$ is defined in equation (4.69). Because of the influence of the spherical Bessel functions with complex argument, equation (4.71) displays a manifold of solutions. The roots are searched with the algorithm of Oftadeh and co-workers for computing the complex roots of systems of nonlinear equations [66, 67]. The algorithm begins with

an initial estimate of the root. The initial estimates were determined according to the analysis of the function $F(qa)$ in figure 4.5. In these diagrams, two horizontal lines are added representing the real and imaginary parts of the left-hand side of equation (4.69). The crossing points of the horizontal lines with the real and imaginary parts of the function $F(qa)$ in Figs. 4.5a and b are identified as appropriate values for the initial estimates.
From analysing the data in figure 4.5 it was concluded that for values of the imaginary part of the argument qa greater than 5 no roots exist [14]. For values of the imaginary part of the argument qa less than 0.5, the function $F(qa)$ assumes a regular shape with nearly evenly spaced intersections with the horizontal lines. These intersections, which are straightforward to find, define the set of starting values of qa for the algorithm.
Concerning the range of values of the real part of the argument qa, the appropriate domain, which delivers the roots relevant to the experiments, is covering the values from 0 to approximately 40.
The complex domain where the relevant roots are located, for the case depicted in figure 4.5, is therefore between $0i$ and $5i$ for the imaginary, and between 0 and 40 for the real part of the argument qa. The roots found are the complex numbers $qa = q_r a + iq_i a$ satisfying (4.71). The numerical routine determines the roots to machine precision of the computer. Figure 4.6 shows the pairs of real and imaginary parts of the argument qa satisfying the characteristic equation (4.64) for the 1.94 mm 0.3 wt% Praestol 2500 drop studied in [14].

2. From the set of solutions $qa = q_r a + iq_i a$ of the characteristic equation, the deformation retardation time is determined by solving equation (4.70). The rewritten equation (omitting the radius a) reads

$$q^2 = \frac{\rho\alpha_2}{\eta_0}\frac{1-\alpha_2\lambda_1}{1-\alpha_2\lambda_2} \tag{4.72}$$

where $q^2 = (q_r + iq_i)^2 = q_r^2 - q_i^2 + 2iq_rq_i$ and $\alpha_2 = \alpha_{2,r} + i\alpha_{2,i} = \alpha_{2,r} + i2\pi f$ is the measured complex frequency of the mode $m = 2$. The complex equation (4.72) is a system of two equations for two liquid properties which can be determined from it; either the pair (λ_2, λ_1), or the pair (λ_2, η_0). For the latter pair, analytical solutions are

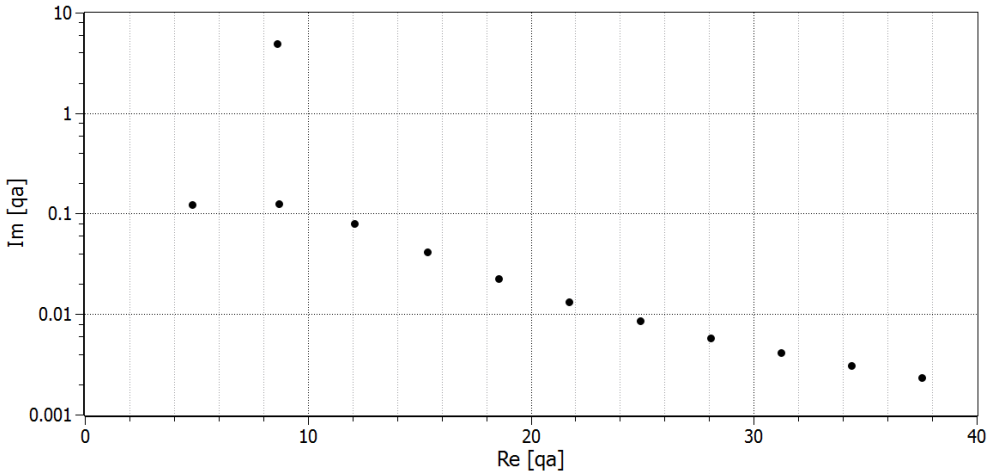

Figure 4.6: The pairs of real and imaginary parts of the argument qa satisfying the characteristic equation (4.64) for the 1.94 mm 0.3 $wt\%$ Praestol 2500 drop studied in [14].

found, and they are given as

$$\lambda_2 = \frac{\alpha_{2,r}\beta_2 + \lambda_1\alpha_{2,i}^2 - \beta_1\left[\alpha_{2,i}\beta_2 - \lambda_1\alpha_{2,r}\alpha_{2,i}\right]}{\left(\alpha_{2,r}^2 + \alpha_{2,i}^2\right)\left(\lambda_1\beta_1\alpha_{2,i} + \beta_2\right)} \tag{4.73}$$

and

$$\eta_0 = \frac{\rho}{q_r^2 - q_i^2}\frac{\left(\alpha_{2,r}\beta_2 + \lambda_1\alpha_{2,i}^2\right)\left(1 - \lambda_2\alpha_{2,r}\right) - \left(\alpha_{2,i}\beta_2 - \lambda_1\alpha_{2,r}\alpha_{2,i}\right)\lambda_2\alpha_{2,i}}{\left(1 - \lambda_2\alpha_{2,r}\right)^2 + \left(\lambda_2\alpha_{2,i}\right)^2} \tag{4.74}$$

with $\beta_1 := \left(q_r^2 - q_i^2\right)/2q_rq_i$ and $\beta_2 := \left(1 - \lambda_1\alpha_{2,r}\right)$.
For each root of equation (4.71) a different pair of (λ_2, λ_1) or (λ_2, η_0) satisfying equation (4.72) exists.

3. The identification of the right solution among the calculated pairs follows from the comparison of the calculated values of λ_1 or η_0 with the results from the measurements with a filament stretching elongational rheometer (λ_1^*) or rotational viscosimeter (η_0^*), respectively.

5 Characterization of the test liquids

This chapter presents a thorough characterization of viscoelastic liquids. The available experimental methods for measuring the relevant rheological properties are described. These properties are the zero-shear viscosity, surface tension, density and stress relaxation time. The measured data are presented in the table at the end of this chapter.

5.1 Polymeric liquids

5.1.1 Materials

The experiments were carried out with aqueous solutions of the two different polyacrylamides Praestol 2500 and Praestol 2540 from Solenis Technologies (Germany). High molecular weight water-soluble polyacrylamides are synthetic organic polymers, which are mainly used as flocculants. Polyacrylamides can be classified as non-ionic, anionic or cationic according to the type of ionic charge present. The properties of the polymers, such as the molecular mass, type of charge and the degree of hydrolysis, were provided by the manufacturer. Praestol 2500 and Praestol 2540 were obtained in a white granular powder form.
The linear polyacrylamide Praestol 2500 (P2500) is a non-ionic organic polymer with a degree of hydrolysis of $3-4$ % and with a molecular mass of $M \approx 15-20\times10^6$ kg kmol^{-1}. The molecular structure of the repeating unit of the Praestol 2500 polymer is shown in figure 5.1. The linear polyacrylamide Praestol 2540 (P2540) is middle anionic polymer with a degree

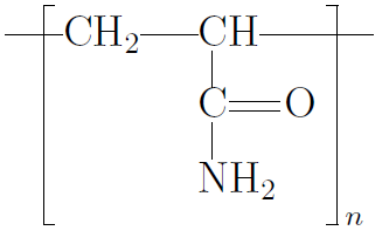

Figure 5.1: The structure of the repeating unit of the polymer Praestol 2500 .

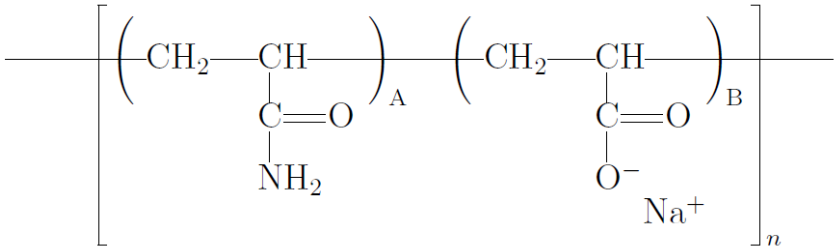

Figure 5.2: The structure of the repeating unit of the polymer Praestol 2540.

of hydrolysis of 40 % and with a molecular mass of $M \approx 15 - 20 \times 10^6$ kg kmol^{-1}. The molecular structure of the repeating unit of the Praestol 2540 polymer is shown in figure 5.2.

5.1.2 Preparation

The aqueous polymer solutions were prepared in pure demineralised water, producing a master solutions with a known polymer mass fraction. The first master solution contained 10000 ppm of the polymer Praestol 2500 and the second master solution contained 1000 ppm of the polymer Praestol 2540. The solutions were stirred for about 12 hours and then rested for 24 hours at room temperature in order to produce homogeneous solutions.
The master polymer solutions were prepared in an glass beaker, with an inner diameter of about 160 mm, by slowly adding the polymer powder to demineralised water, while slowly swirling the fluid in order to achieve wetting of each granule. This way the formation of lumps is minimized and

the incomplete dissolution of the polymer is avoided. The stirring was done with an anchor stirrer, with a blade diameter of about $\approx$ 70 mm, at low rotational speed (100 rpm) in order to avoid shear-induced degradation of the polymer macromolecules [68].
In the solutions of P2500 and P2540, small portions of gel structures were formed and the liquids had to be put trough a stainless-steel sieve with a mesh width of 300 µm to remove theses lumps. The master solutions were then diluted to obtain the various concentrations for the experiments. The densities of the test liquids were all in the order of 10^3 kg m^{-3}, as in [13, 14]

5.2 Shear rheometry

The shear rheometric characterisation of the polymer solutions was carried out with the rotational rheometer ANTON PAAR Physica UDS 200 at the Institute of Chemistry of the University of Graz. The device enables rotational experiments for measuring the shear viscosity as a function of shear rate (flow curve) as well as oscillatory experiments for measuring the loss and storage moduli of the test liquids. After each experiment, a fresh liquid sample was used.

5.2.1 Rotational experiments

In a rotational viscosimeter, the test samples are loaded between a fixed and a moving solid surface. A kinematic quantity in form of shear, shear rate or angular frequency was applied to the sample and the material response in terms of torque M and normal force F was measured. For measuring the flow curves of the polymer solutions, two configurations/geometries were used; the cylindrical double gap measuring system for polymer solutions with viscosities lower than 0.02 N s m^{-2}, and the cone-plate geometry for viscosities above 0.02 N s m^{-2}.

Cone-and-plate geometry
For the cone-and-plate geometry, the configuration MS-KP 25 (according to

DIN 53018) was used (figure 5.3). This configuration enables shear rates in the range $0 - 2400\ s^{-1}$ and viscosity measurements in the range from 0.02 $N\,s\,m^{-2}$ to 120 $N\,s\,m^{-2}$. An advantage of the cone-and-plate geometry is the small required volume of the test sample. For the MS-KP 25 configuration, the required volume of the test liquid is 5.2 ml. For accurate measurements it is important that the volume between the plate and the rotating disc is entirely filled with the test liquid [69].

From the imposed shear rate $\dot{\gamma}$ and the measured shear stress τ, the stationary shear viscosity η is obtained as

$$\eta(\dot{\gamma}) = \frac{\tau}{\dot{\gamma}}. \tag{5.1}$$

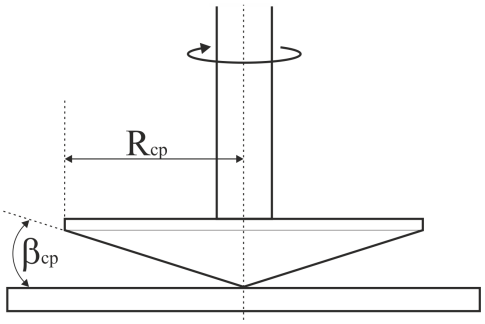

Figure 5.3: Schematic diagram of the cone-and-plate measuring system.

Double gap geometry
For the cylindrical double gap geometry, the configuration Z1 (according to DIN 54453) was used (figure 5.4).
The test liquid is loaded into the narrow gap formed between two fixed concentric cylinders. The flow is driven by a thin inverted cup rotating inside the gap. The distribution of the shear strain inside the very narrow gap is the same as in the Couette flow between two parallel plates and can be regarded constant over the width of the gap, that is, the curvature can be neglected.

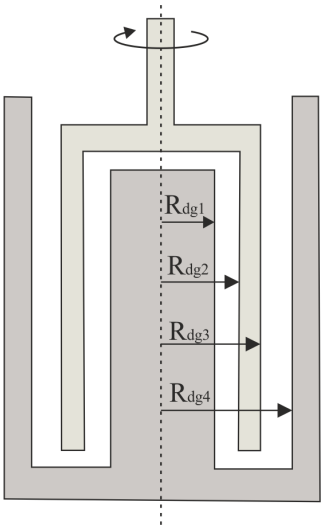

Figure 5.4: Schematic diagram of the double gap measuring system.

Results

The results of the rotational experiments are obtained as flow curves as shown in figure 5.5. At small shear rates, the viscosity reaches a constant value, the so-called *first Newtonian plateau viscosity* or the zero-shear-rate viscosity η_0. For medium shear rates, shear thinning behaviour, which enhances with increasing polymer mass fraction, can be observed. At high shear rates, the *second Newtonian plateau viscosity* (η_∞) is expected, but not fully reached in the current experiments due to experimental limitations. The described dependence of the measured shear viscosity on the shear rate is best approximated by the so-called Carreau model [3]:

$$\eta(\dot{\gamma}) = \frac{\eta_0 - \eta_\infty}{[1 + (K_1 \cdot \dot{\gamma})^2]^{m_1}} + \eta_\infty \tag{5.2}$$

where m_1 and K_1 are fit parameters. The fitting procedure of the experimental data with the equation (5.2) was done using the software from ANTON PAAR. The obtained best fit parameters are listed in table 5.1.

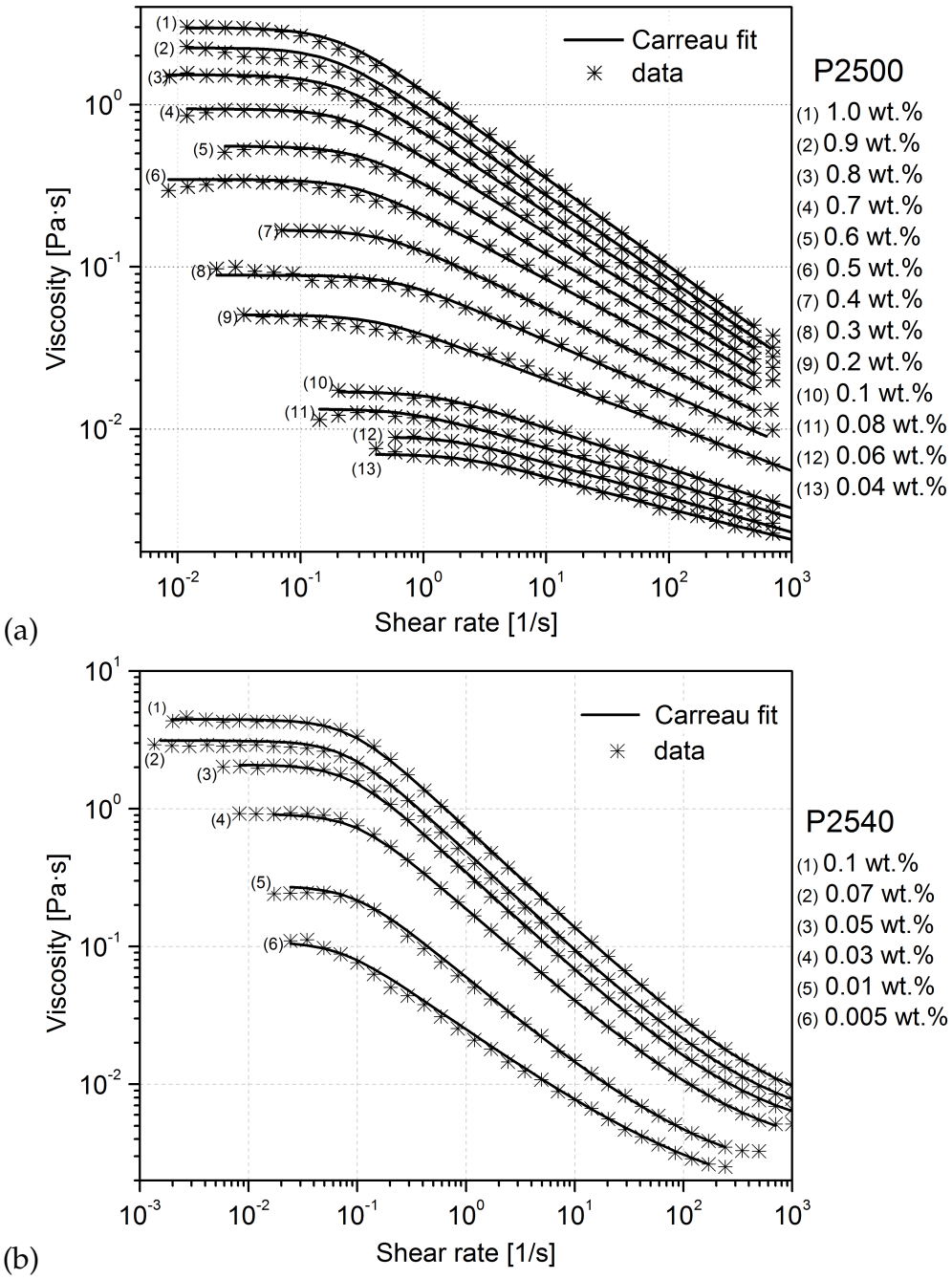

Figure 5.5: Flow curves for (a) aqueous P2500 and (b) P2540 solutions of various polymer mass fractions. The polymer mass fraction increases from bottom to top.

Polymer	w [wt.%]	η_0 [Pa s]	η_∞ [Pa s]	K_1 [s^{-1}]	m_1 [−]
Praestol 2500 (P2500)	0.04	0.0070086	$3.7457 \cdot 10^{-4}$	0.47634	0.10962
	0.06	0.0089914	$2.8209 \cdot 10^{-10}$	0.57134	0.10689
	0.08	0.013305	$3.4939 \cdot 10^{-10}$	1.315	0.10776
	0.1	0.016985	$3.9979 \cdot 10^{-10}$	0.80043	0.1238
	0.2	0.050574	$6.6994 \cdot 10^{-10}$	2.5561	0.14102
	0.3	0.088864	$1.1639 \cdot 10^{-9}$	1.6762	0.16481
	0.4	0.16847	$1.611 \cdot 10^{-9}$	2.0674	0.1847
	0.5	0.34594	$2.1249 \cdot 10^{-9}$	3.4373	0.20074
	0.6	0.55429	$2.6582 \cdot 10^{-9}$	3.2542	0.22
	0.7	0.94028	$3.1607 \cdot 10^{-9}$	4.1787	0.23588
	0.8	1.5258	$3.8295 \cdot 10^{-9}$	5.2181	0.24703
	0.9	2.2418	$4.3453 \cdot 10^{-4}$	5.6319	0.25993
	1.0	2.9742	$5.1664 \cdot 10^{-9}$	5.1557	0.27102
Praestol 2540	0.005	0.10848	0.0013548	14.274	0.28371
	0.01	0.27575	0.0019793	10.335	0.33203
	0.03	0.91688	0.0030357	10.011	0.34653
	0.05	2.0871	0.00416	11.911	0.36414
	0.07	3.1119	0.0047122	12.587	0.36635
	0.10	4.4462	0.005323	11.645	0.3691

Table 5.1: The fit parameters of the Carreau model (5.2) for aqueous polymer solutions at 22 °C.

The difference between aqueous solutions prepared with the flexible (PRAESTOL 2500) and rigid rod-like (PRAESTOL 2540) polymers can be seen in figure 5.6, where the dependence of the zero-shear-rate viscosity η_0 on the polymer mass fraction w is shown.
The aqueous solutions of flexible polymers (P2500) (figure 5.6a) show an approximately linear increase of the zero-shear-rate viscosity η_0 with the polymer mass fraction w for concentrations up to 0.1 wt.%. Increasing the polymer mass fraction above 0.1% causes a steep increase of the viscosity, indicating roughly the concentration at which the polymer molecules start to overlap and become entangled [16]. This behaviour is typical for solutions

of high molecular-weight polymers. Above the critical concentration, η_0 increases with w following a power law.
Rigid rod-like polymers in aqueous solutions show a different behaviour in the zero shear rate–concentration relationship, which does not allow for a distinction between the concentration regimes in the range under investigation (figure 5.6b).

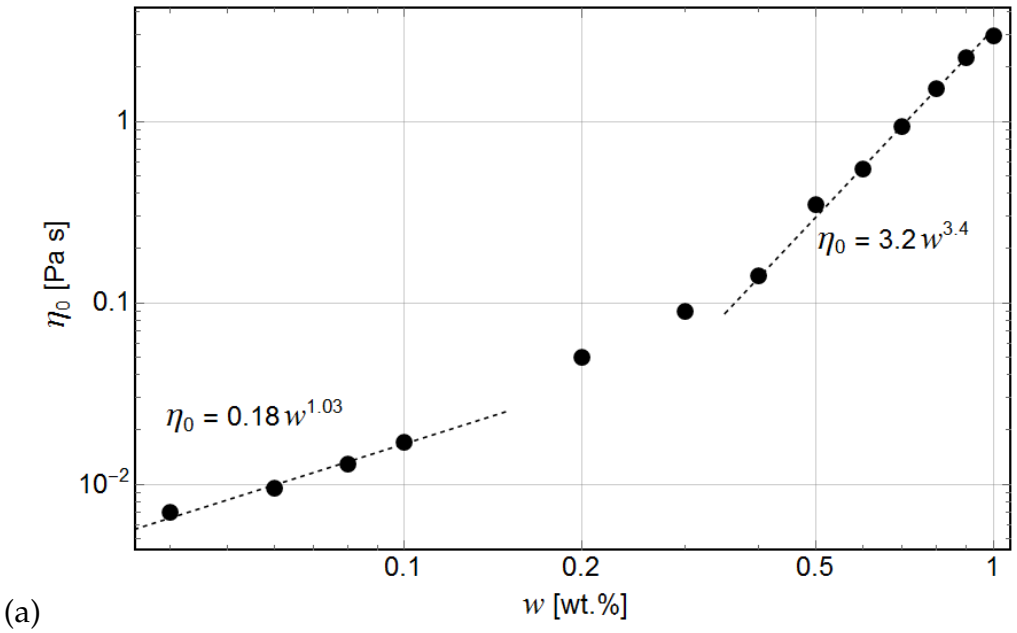

(a)

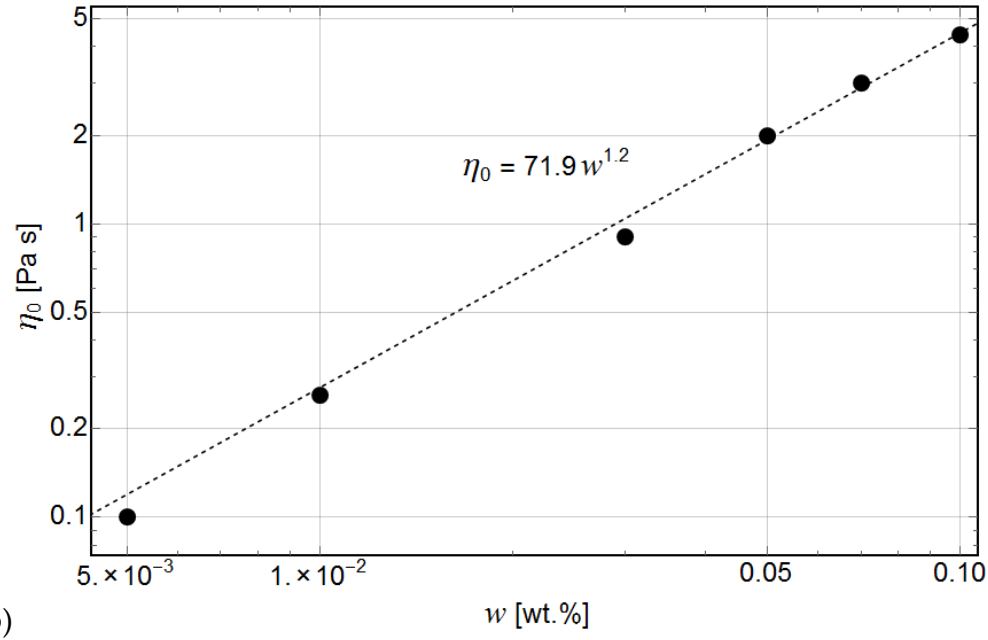

(b)

Figure 5.6: Zero shear viscosity vs. polymer mass fraction for (a) P2500 and (b) P2540 in water. The equations yield η_0 in Pa s for w in wt.%.

5.2.2 Oscillation experiments

The oscillation experiments are used to study the linear viscoelastic behaviour by applying a sinusoidal shear strain

$$\gamma^*(t) = \hat{\gamma}^* e^{i\omega t} \tag{5.3}$$

with the angular frequency ω and $i = \sqrt{-1}$ to the viscoelastic test liquid. The corresponding induced shear stress is given as

$$\tau^*(t) = \hat{\tau}^* e^{i(\omega t+\delta)} = \int_{-\infty}^{t} G(t-t') \frac{\mathrm{d}\gamma^*(t')}{\mathrm{d}t'} \,\mathrm{d}t' = i\omega\hat{\gamma}^* \int_{-\infty}^{t} G(t-t') e^{i\omega t'} \,\mathrm{d}t' \tag{5.4}$$

where δ is the phase shift and $G(t)$ is the linear relaxation modulus. Viscoelastic behaviour can be described by the complex modulus G^* defined as

$$G^* = \frac{\tau^*}{\gamma^*} = \frac{\hat{\tau}^*}{\hat{\gamma}^*} e^{i\delta} = G' + iG'', \tag{5.5}$$

where G' and G'' are the storage and the loss modulus, respectively. The storage modulus corresponds to the elastic portion of the viscoelastic behaviour and represents the stored deformation energy. The loss modulus corresponds to the viscous portion of the viscoelastic behaviour and represents the dissipated or lost deformation energy.
For estimating whether the elastic or viscous behaviour is dominating, the dissipation factor $\tan(\delta)$ is used. The dissipation factor is defined as the ratio between the storage and loss modulus

$$\tan(\delta) = \frac{G''}{G'}. \tag{5.6}$$

For $\tan(\delta) < 1$ elastic behaviour dominates and for $\tan(\delta) > 1$, the viscous behaviour dominates. In terms of the phase shift that means that $\delta = 0$ for an elastic solid, and $\delta = \pi/2$ for a purely viscous fluid.

An important concept in studying the relaxation behaviour is the relaxation spectrum $H(\lambda)$ given by

$$G(t) = \int_0^\infty H(\lambda)\, \mathrm{e}^{-t/\lambda}\, \frac{\mathrm{d}\lambda}{\lambda} = \int_{-\infty}^\infty H(\lambda)\, \mathrm{e}^{-t/\lambda}\, \mathrm{d}(\ln\lambda) \tag{5.7}$$

for continuously distributed relaxation times using the generalized Maxwell model (see [3], p. 285, [58], p. 60 and [15], p. 93). As noted in ([16], p. 161), in an ideal case of polymer solutions with linear polymers of the same length and the same molar mass, the relaxation behavior can be described using a single Maxwell model (3.41).

Combining and rewriting equations (5.4) and (5.5) results in

$$G^* = G' + iG'' = \int_0^\infty \omega\, G(s) \sin(\omega s)\, \mathrm{d}s + i \int_0^\infty \omega\, G(s) \cos(\omega s)\, \mathrm{d}s, \tag{5.8}$$

where $s = t - t'$ was introduced.
Inserting (5.7) in (5.8) and integrating with respect to s, one obtains

$$G'(\omega) = \int_0^\infty \frac{\omega^2\, \lambda^2\, H(\lambda)}{1 + \omega^2\, \lambda^2}\, \mathrm{d}(\ln\lambda) \tag{5.9}$$

and

$$G''(\omega) = \int_0^\infty \frac{\omega\, \lambda\, H(\lambda)}{1 + \omega^2\, \lambda^2}\, \mathrm{d}(\ln\lambda). \tag{5.10}$$

As noted further in ([15], p. 94), inversion of the measured data, that is, inversion of G' (5.9) and G'' (5.10), to obtain $H(\lambda)$ is an ill-conditioned problem.
From measured G' and G'' vs. ω, the linear relaxation modulus $G(t)$ and the relaxation spectrum $H(\lambda)$were obtained using the software provided by ANTON PAAR.

Results

In the oscillation experiments, G' and G'' vs. ω were measured. Because the formulations of G', G'', $G(t)$ and $H(\lambda)$ were made within the field of linear viscoelastic material behaviour, a test of linearity was conducted for each test liquid. The test of linearity was performed by means of an amplitude sweep by varying the amplitude $\hat{\gamma}$ at constant frequency of 1 Hz.

The measured loss and storage moduli are expected to remain constant in the linear viscoelastic regime.
The results of the linearity test are shown in figure 5.7. Similar results were obtained for all test liquids investigated. From the results of the amplitude sweeps it was concluded that the validity of the linear viscoelastic theory is limited to $\hat{\gamma} < 40$ %. Therefore, an amplitude of $\hat{\gamma} = 10$ % was set in order to ensure the linear viscoelastic behaviour of the test liquids.

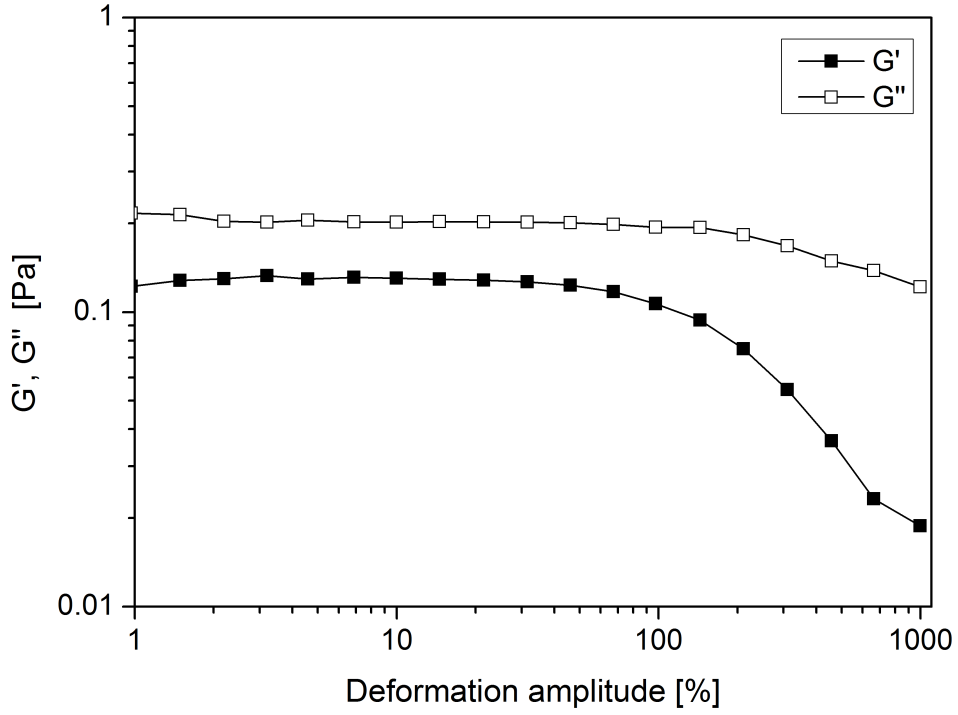

Figure 5.7: Results of the amplitude sweep test at the constant frequency of 1 Hz for the aqueous 0.5 *wt*.% Praestol 2500 solution.

The results of the oscillatory experiments for aqueous PRAESTOL 2500 and PRAESTOL 2540 solutions are shown in figures 5.8 and 5.9, where the plots of G' and G'' against ω are presented.
For aqueous PRAESTOL 2500 solutions with polymer mass fraction below 0.1 wt.% and aqueous PRAESTOL 2540 solutions with polymer mass fraction below 0.03 wt.% no reliable results were obtained, due to the low viscosity.

For low angular frequencies, the loss modulus exceeds the storage modulus

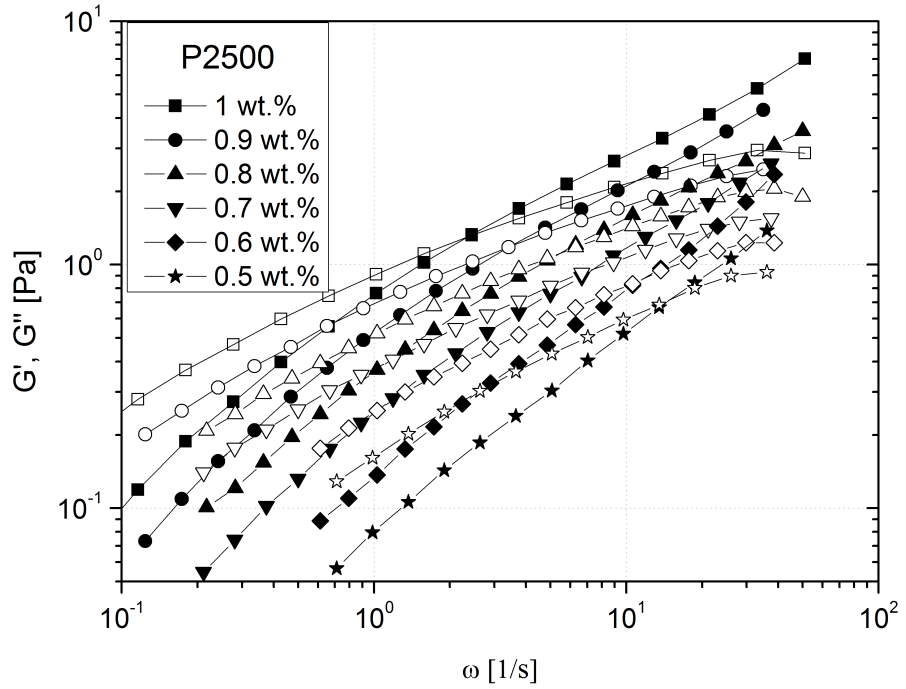

Figure 5.8: Storage G' (solid symbols) and loss moduli G'' (open symbols) of aqueous polymer solutions P2500 for different polymer concentrations against the angular frequency ω.

for both polymer solutions studied. At high angular angular frequencies, the storage modulus exceeds the loss modulus, which indicates that elasticity dominates over viscosity.

A crossover angular frequency ω_X exists where both moduli have the same value $G'(\omega_X) = G''(\omega_X)$. The crossover point moves to higher angular frequencies with decreasing polymer mass fraction. This trend is clearly visible in case of Praestol 2500 polymer solutions (figure 5.8), while for the Praestol 2540 polymer solutions (figure 5.9) this trend can be observed for higher polymer mass fractions (above 0.03 $wt.\%$).

When the fluid behaviour is described by the Maxwell model, that is by equations (5.9) and (5.10), the crossover frequency is often used to determine

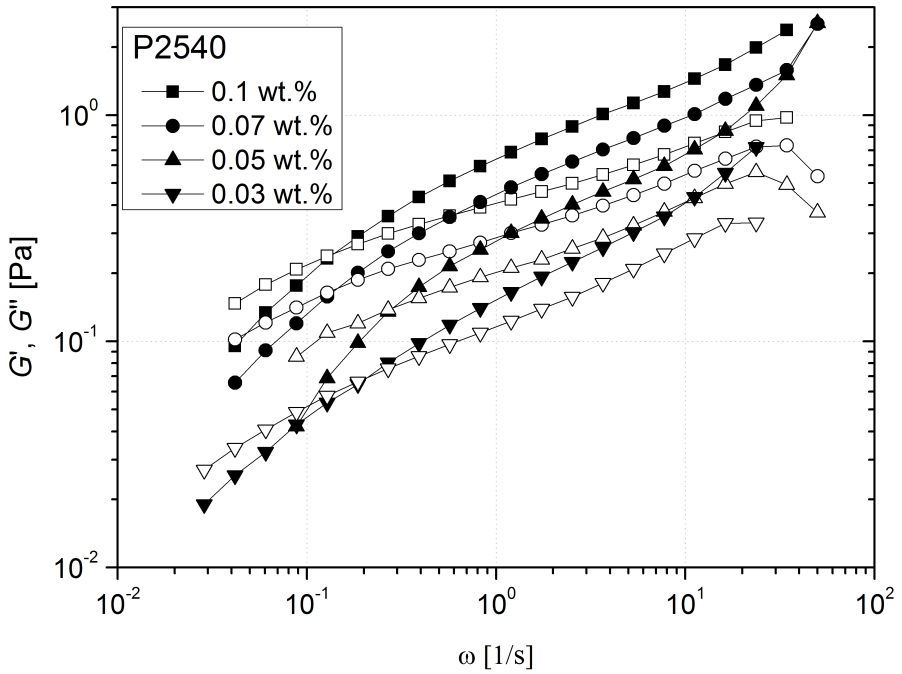

Figure 5.9: Storage G' (solid symbols) and loss moduli G'' (open symbols) of aqueous polymer solutions P2540 for different polymer concentrations against the angular frequency ω.

the longest relaxation time as

$$\lambda_{1,X} = \frac{1}{\omega_X}. \tag{5.11}$$

In the present case, however, this relaxation time $\lambda_{1,X}$ does not match with the relaxation time obtained by the elongational rheometer (see the next Section 5.3). This may indicate that the Maxwell model with a single stress relaxation time is not able to properly describe the measured data.

The relaxation time spectrum $H(\lambda)$ (5.7), calculated from the loss and storage moduli using the software from ANTON PAAR, is presented in figure 5.10.
As noted in Ferry ([58], p. 60), for liquids at long time scales, when steady-state flow is reached, $H(\lambda)$ should vanish. The relaxation time spectra of the solutions studied in the present work exhibit low values of $H(\lambda)$ for high

values of the relaxation time λ. At short time scales, $H(\lambda)$ should vanish, due to the nearly pure elastic material response on short time scales ([58], p. 60). This trend is also visible in the presented relaxation time spectra.
As noted in ([16], pp. 165-168), there is a correlation between the complex modulus G^* and the polymer molar mass distribution (MMD). Ferry ([58], pp. 198-200) discusses the effect of the polymer polydispersity on the components of the complex modulus G^*. For dilute solutions of linear polymers, at high frequencies, G' and G'' are independent of the molecular weight distribution, while at low frequencies the behavoiur of G' and G'' may be expressed in terms of molecular weight averages ([58], p. 198). When polymers with different molecular weights are mixed, the relaxation time of the lower molecular weight polymer tends to shift to longer times, while those of the higher molecular weights tends to shift to shorter times [58, 70]. The combined effect of the shift results in narrowing the relaxation time spectrum [70].
There are some methods for obtain the polymer molecular mass distribution (MMD) from measured relaxation time spectra [70, 71]. Regardless of the method used to relate the rheological properties to the MMD, this represents an ill-posed problem, because the molecular weight distribution is very sensitive to small variations in the rheological measurements [70]. Therefore, the relaxation time spectra, shown in figures 5.10(a) and 5.10(b), are not discussed any further.

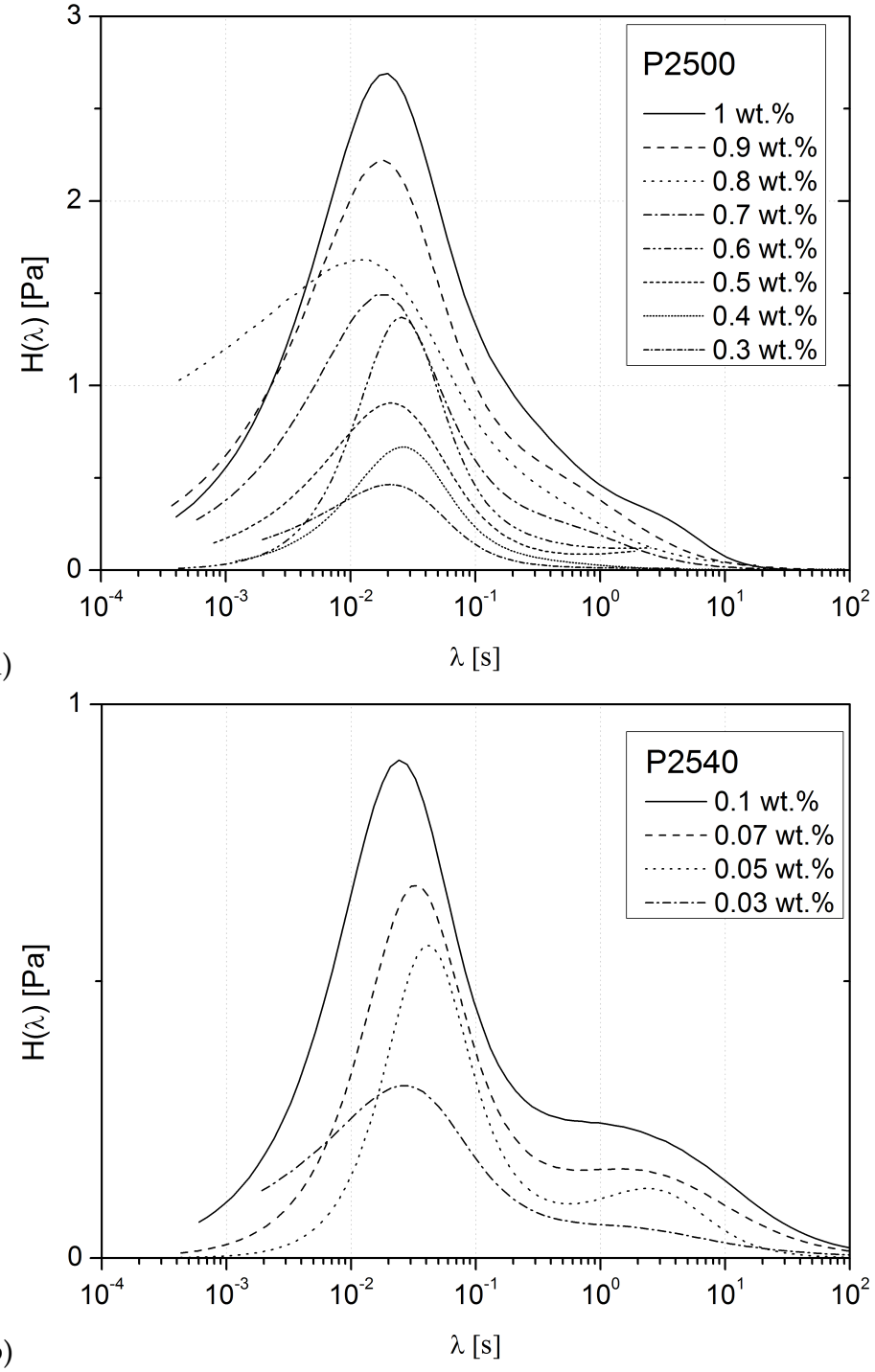

Figure 5.10: Relaxation time spectra of aqueous solutions (a) of Praestol 2500 and (b) Praestol 2540 for different polymer mass fractions.

5.3 Elongational rheometry

The stress relaxation time λ_1 of the liquids was measured with a non-commercial filament stretching elongational rheometer of the CaBER type [8, 9]. The basic experimental setup of the elongational rheometer is shown in Figure 5.11. The test liquid is loaded between two plates; the upper plate is movable, and the bottom plate is fixed. The upper plate is pulled up by an electromagnet in a short time. While the test liquid is stretched, it takes a cylindrical form with circular cross-section. Due to the capillary forces, self-thinning of the liquid filament occurs, that is, the diameter of the cylindrical filament decreases in time, which is monitored by an optical device. From the measured filament diameter as a function of time, the relaxation time λ_1 is calculated.

In the present work a non-commercial elongational rheometer was used. Therefore, basic assumptions and theoretical background are first presented.

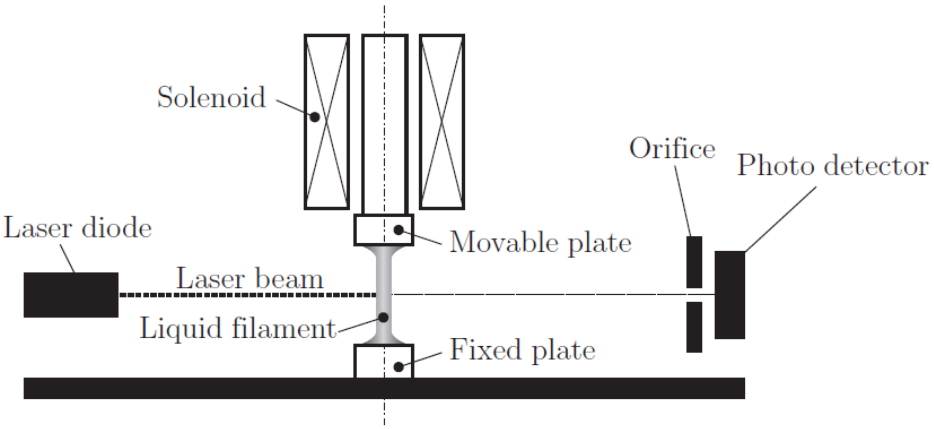

Figure 5.11: Experimental setup for elongational rheometry [72].

5.3.1 Theoretical background

Observing the self-thinning process of a cylindrical liquid filament, the following assumptions can be made. The filament in its main part, except for the end regions at the plates, remains in its cylindrical shape with a circular cross-section during the self-thinning process.Therefore, the filament diameter d_f is constant in the axial direction $\partial d_f / \partial z = 0$. And, because of the axisymmetry, one can set $\partial / \partial \varphi = 0$ and $u_\varphi = 0$. On the surface of the liquid thread no shear stress exists. The filament can be considered as long and thin, therefore the mass forces and inertia can be neglected in the momentum balance. The homogeneous flow field in the filament is governed only by capillary pressure, resulting in a uniaxial elongational flow towards both end regions of the liquid thread [3]. Stelter *et al.* [8, 9] derived the following linear momentum equation with boundary conditions

$$\tau_{zz} = \frac{4\sigma}{d_f} \tag{5.12}$$

assuming $\tau_{zz} >> \tau_{rr}$. The closure of (5.12) requires the rheological model for the tested viscoelastic liquid. Stelter *et al.* [9] implemented the upper convected Maxwell model (3.5). They identified two regimes of the filament self-thinning process of semi-dilute solutions. In the first part of the self thinning process the polymer solutions shows viscoelastic behaviour, and the filament diameter decreases exponentially with time as

$$d_f = d_{f,0} \exp\left(-\frac{t}{3\lambda_1}\right). \tag{5.13}$$

where λ_1 is the relaxation time and $d_{f,0}$ is the initial filament diameter. After the maximum possible polymer extension is reached, the polymer solution shows Newtonian-like behaviour. In this second regime, the filament diameter decreases linearly with time as

$$d_f = d'_{f,0} - \frac{\sigma}{\eta_{E,t}} t, \tag{5.14}$$

where $\eta_{E,t}$ is the steady terminal elongational viscosity, σ is the surface tension and $d'_{f,0}$ is the initial filament diameter at the onset of Newtonian behaviour.

5.3.2 Experiments and results

A small sample of the liquid with a volume of 10 µl is stretched between two plates in a short time ≤ 1 ms and the diameter relaxation with time of the filament formed by the stretching process is recorded by an optical shadow technique. The diameter evolution is governed by the stress relaxation time λ_1 of the liquid.
The liquid filament is positioned in the laser beam and the filament diameter as a function of time is measured by evaluating the power of light from the laser diode received by the photo detector. The voltage-time relationship at the photo detector during the filament thinning is recorded by an oscilloscope (TEKTRONIX TDS 220) and transferred to a computer. The relationship between the reduction of the light power, expressed in terms of voltage decay at the photo detector, and the filament diameter is linear and obtained by a calibration procedure. For determining the relaxation time, only the first regime of the diameter decrease is used and approximated by (5.13) using computer software MATHEMATICA. The exponent of the function obtained by a data fit determines the relaxation time.

Figure 5.12 shows the non-dimensional filament diameter as a function of time. Measurements repeated 10 times yielded mean values with standard deviations of about 10%. Figure 5.13 shows the results of the measurements with the elongational rheometer, where the stress relaxation time as a function of the polymer mass fraction for aqueous P2500 and P2540 polymer solutions is presented.
The dependency of the measured relaxation time on the polymer mass fraction w is approximated by the scaling law

$$\lambda_1 \propto w^s, \tag{5.15}$$

where $s = 0.86$ for the aqueous P2500 polymer solutions and $s = 0.79$ for the aqueous P2540 polymer solutions. Similar values for the exponent s were reported by Stelter *et al.* [8], for solutions of the same polymers. The aqueous solutions in [8] were prepared with the same polymer batches (Praestol), provided by the same manufacturer.

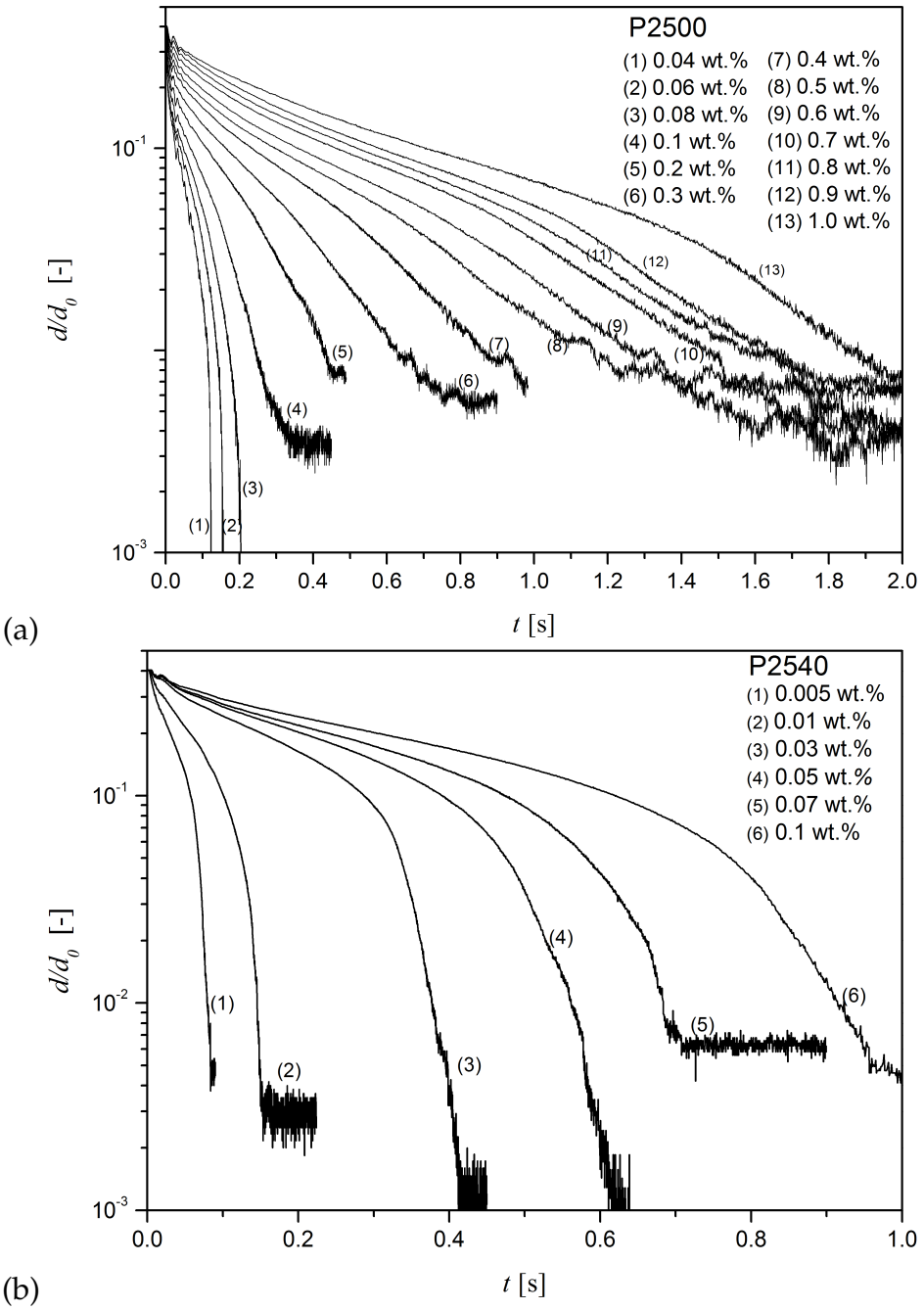

Figure 5.12: Elongational rheometry measurements. The non-dimensional filament diameter as a function of time for aqueous (a) P2500 and (b) P2540 polymer solutions.

From figure 5.13 is evident that the relaxation time of both aqueous polymer solutions increases with the polymer mass fraction. As noted in [8], this result is a clear indication that the aqueous polymer solutions studied cannot be considered as dilute. Further in [8], the polymer solutions should be treated as semidilute solutions, due to the manifestation of the effects of interactions between polymer macromolecules.

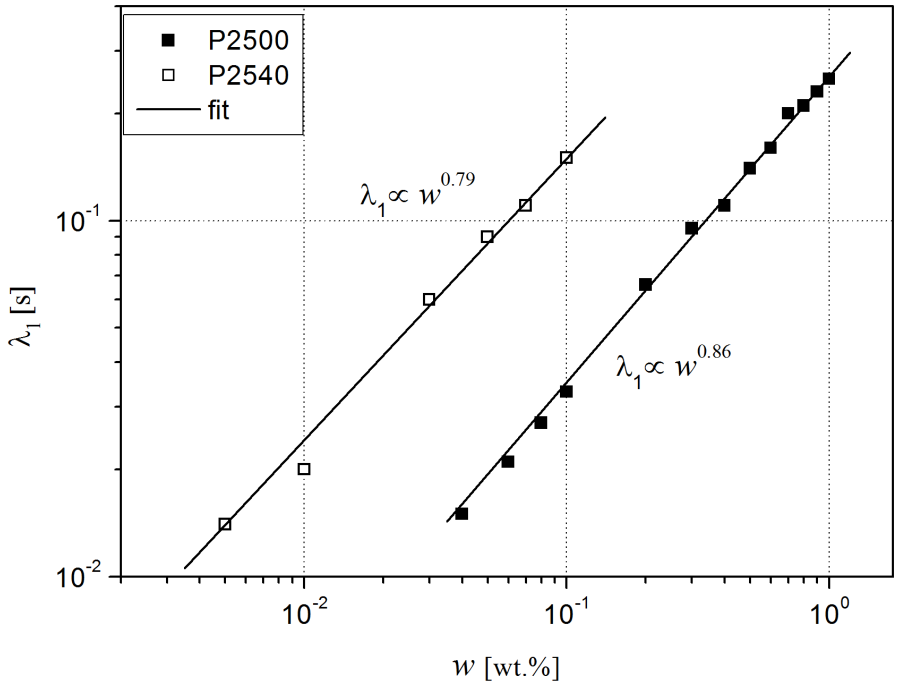

Figure 5.13: Elongational rheometry measurements. The stress relaxation time as a function of the polymer mass fraction for aqueous P2500 and P2540 polymer solutions.

5.4 Surface tension measurement

Another measured quantity, important in studying viscoelastic fluid behaviour in free surface flow is the surface tension. There exist many methods to measure the surface tension (e.g. sessile drop method, drop weight method, drop volume method, drop shape method [39, 73–75]).
In the present work, the surface tension σ was measured with the drop shape technique using a pendant-drop setup.

5.4.1 Pendant-drop method

In the present work, a non-commercial pendant drop tensiometer was used. The experimental setup for pendant-drop tensiometry, shown in figure 5.14, requires a needle, a light source and a camera.

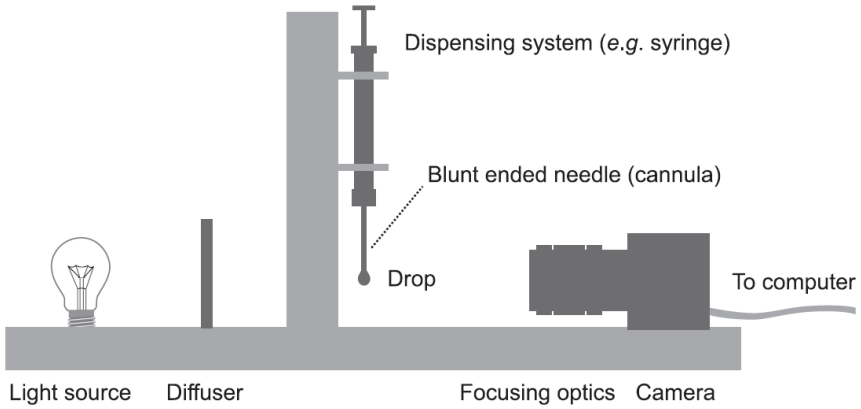

Figure 5.14: Experimental setup for pendant drop tensiometry [73].

The axisymmetric drop is formed at the end of a needle with known diameter. The pendant drop shape at equilibrium is influenced only by surface tension and gravity. Thus, any movement of the drop should be avoided or minimized, and the needle must be accurately vertically aligned. The restoring force of surface tension tends to minimize the surface area and pulls the drop into a spherical shape. On the other hand, the distorting gravitational force tends to stretch the drop. In equilibrium, both forces are

balanced. A pendant drop at equilibrium is described by the Young-Laplace equation

$$\sigma \left(\frac{1}{R_1} + \frac{1}{R_2} \right) = \Delta P \tag{5.16}$$

which relates the pressure difference across the interface ΔP (Laplace pressure) with the principal radii of curvature R_1 and R_2 of the drop surface and the surface tension σ [73, 76]. At the lowest point of the drop (drop apex), the principal radii of curvature are equal $R_1 = R_2 = R_0$. Therefore the reference plane is placed at this point. And, because of the axisymmetry, the cylindrical coordinates r,z, together with tangent angle φ were chosen, as shown in figure 5.15.
The Laplace pressure can be written in terms of the hydrostatic pressure $\rho g z$ inside the drop and the reference pressure ΔP_0 at $z = 0$

$$\Delta P = \Delta P_0 - \Delta \rho g z \tag{5.17}$$

where $\Delta\rho = \rho_d - \rho_m$ is the density difference between drop liquid density ρ_d and surrounding medium density ρ_m. Inserting (5.17) in (5.16) and evaluating the resulting equation for $z = 0$ results in

$$\Delta P_0 = \frac{2\sigma}{R_0}. \tag{5.18}$$

Introducing the parametrization using the arc length s measured from the lowest point of the drop $z = 0$, the radii of curvature can be written as

$$R_1 = \frac{\mathrm{d}s}{\mathrm{d}\varphi} \qquad \text{and} \qquad R_2 = \frac{r}{\sin\varphi}. \tag{5.19}$$

The above derivation results in a coupled set of first-order differential equations [73]:

$$\begin{aligned} \frac{\mathrm{d}\varphi}{\mathrm{d}\tilde{s}} &= 2 - \mathrm{Bo}\,\tilde{z} - \frac{\sin\varphi}{\tilde{r}} \\ \frac{\mathrm{d}\tilde{r}}{\mathrm{d}\tilde{s}} &= \cos\varphi \\ \frac{\mathrm{d}\tilde{z}}{\mathrm{d}\tilde{s}} &= \sin\varphi \end{aligned} \tag{5.20}$$

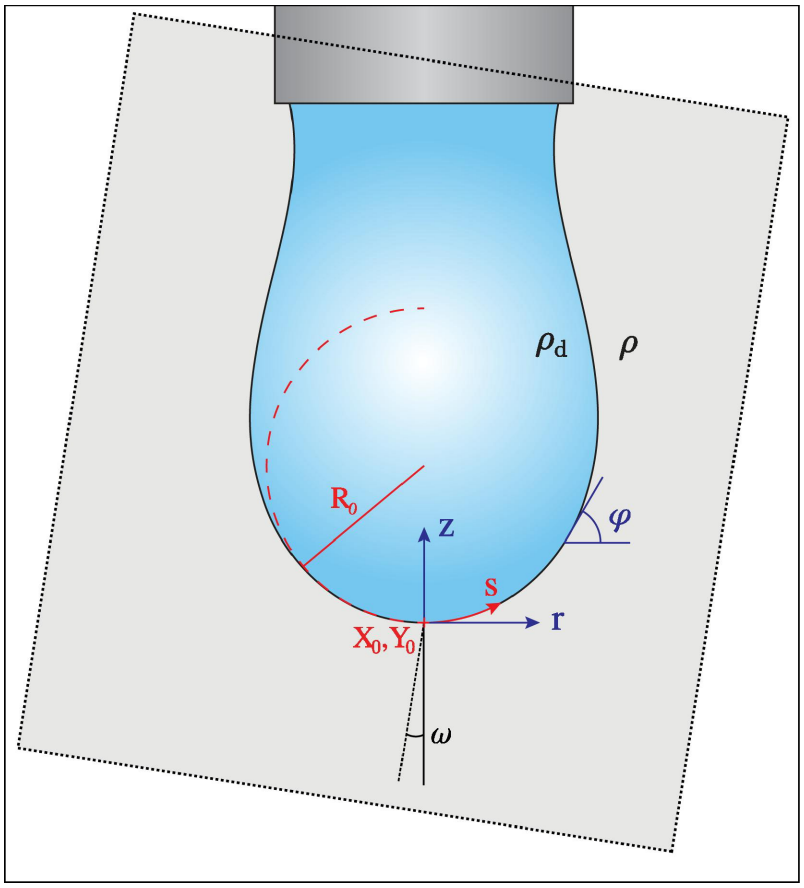

Figure 5.15: Schematic of a pendant drop with associated variables [73].

where $\tilde{s} = s/R_0$, $\tilde{r} = r/R_0$ and $\tilde{z} = z/R_0$ are the non-dimensional variables and Bo is the Bond number, defined as

$$\mathrm{Bo} = \frac{\Delta\rho\, g\, R_0^2}{\sigma}. \tag{5.21}$$

The above system of differential equations (5.20) is closed with boundary conditions at the drop apex $s = 0$:

$$r(s = 0) = z(s = 0) = \varphi(s = 0) = 0. \tag{5.22}$$

The pendant drop shape therefore depends only on one non-dimensional parameter Bo, the Bond number.

The pendant drop method for surface tension determination consists of the following steps. First, the test liquid is loaded in the syringe, and a liquid drop is slowly formed at the tip of the needle. An image of the pendant drop, including the tip of the needle, was recorded. The optical magnification is determined with known diameter of the needle. Then the drop surface profile is extracted from the image. Next, the Young-Laplace equation is solved numerically, iteratively adjusting parameters to find the best fit to the extracted shape of the drop. From the resulting Bond number Bo, the surface tension is calculated. The determination of the drop profile and solving the Young-Laplace equation is done with the computer software Matlab. The system of differential equations (5.20) was solved numerically by implementing the fourth order Runge-Kutta method [75, 76].

5.4.2 Results

The measured surface tension as a function of the polymer mass fraction for aqueous P2500 and P2540 polymer solutions is presented in figure 5.16.

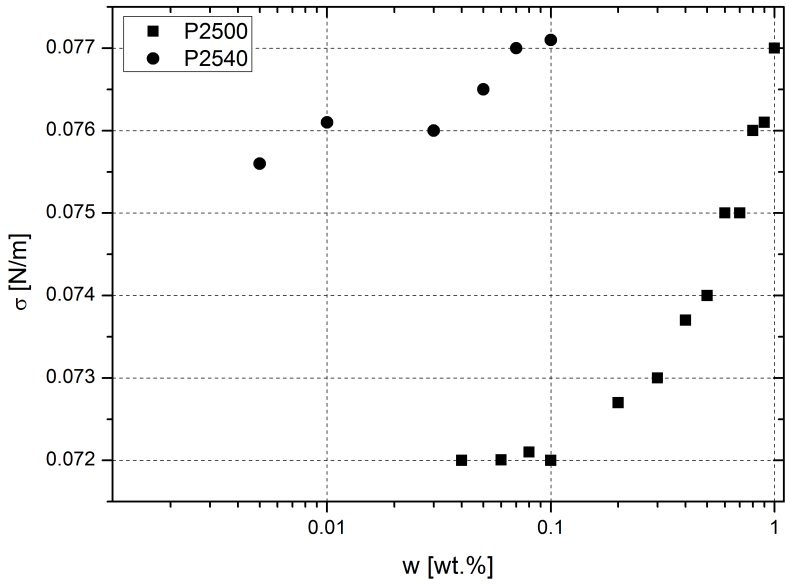

Figure 5.16: Pendant drop measurements. The surface tension as a function of the polymer mass fraction for aqueous P2500 and P2540 polymer solutions.

The value of the surface tension tends to increase with increasing polymer mass fraction for both polymer solutions, although the increase is small and of the order of the measurement error. The values of the surface tension for the aqueous solutions at the lowest and highest polymer mass fraction differ by about 5 $\mathrm{mN\,m^{-1}}$ for the P2500 polymer solutions and by about 2 $\mathrm{mN\,m^{-1}}$ for the P2540 polymer solutions.

Comparison of the measured surface tension with the corresponding measurements reported in Pilz and Brenn [72] and Brenn and Teichtmeister [13] using solutions of the same polymer batches shows good agreement.

5.5 Summary

The measured fluid properties are listed in the table 5.2. The densities of all aqueous polymer solutions were set equal to the solvent density of 1000 $\mathrm{kg\,m^{-3}}$, due to the small polymer mass fraction and hence a negligible influence on the solvent density, as in [13, 14, 72].

Polymer	w [wt.%]	η_0 [Pa s]	λ_1 [s]	σ [N m^{-1}]
Praestol 2500 (P2500)	0.04	0.007	0.015	0.0720
	0.06	0.009	0.021	0.0720
	0.08	0.013	0.027	0.0722
	0.1	0.017	0.033	0.0720
	0.2	0.051	0.066	0.0727
	0.3	0.089	0.095	0.0730
	0.4	0.17	0.11	0.0737
	0.5	0.35	0.14	0.0740
	0.6	0.55	0.16	0.0750
	0.7	0.94	0.20	0.0750
	0.8	1.53	0.21	0.0760
	0.9	2.24	0.23	0.0761
	1.0	2.97	0.25	0.0777
Praestol 2540	0.005	0.11	0.014	0.0756
	0.01	0.28	0.02	0.0761
	0.03	0.92	0.06	0.0760
	0.05	2.09	0.08	0.0765
	0.07	3.11	0.11	0.0770
	0.10	4.45	0.15	0.0771

Table 5.2: The material properties of the investigated aqueous polymer solutions at 22 °C. The density is 1000 kg m^{-3} for all the solutions to a good degree of accuracy.

6 Deformation retardation time measurements

In this chapter the experimental part of the proposed method for measuring the deformation retardation time is presented.
First, the experimental setup is described. Second, the method for measuring the complex angular drop frequency is explained. Next, the deformation retardation time of the viscoelastic liquid is determined. Then the uncertainty estimates are made. At the end, the results and the corresponding uncertainties with sensitivity analysis are presented and discussed.

6.1 Experimental setup

For investigating experimentally damped oscillations of individual drops of viscoelastic liquids, the technique of acoustic levitation was used [13, 14, 77]. The acoustic levitation of drops was achieved using an ultrasonic levitator. This device is an essential part of the present work. Hence, a thorough description of the acoustic levitator system is presented in the next section.

6.1.1 Ultrasonic levitator

An aoustic levitator is a device which uses an acoustic field for levitating fluid and solid particles. The device suspends the sample in a fixed position contactlessly and allows to investigate various physical processes (drying, heat transfer, mass transfer,...) without any influences from contacting mechanical parts [77, 78].
In the present work, an acoustic levitator system from tec5 AG with the

standard frequency (ν_L) of 58 kHz was used. A detailed description of the system can also be found on the homepage of tec5 AG [79]. The corresponding wavelength in ambient air (λ_L) at 22 °C is about 5.9 mm. The maximum sample diameter that can be levitated with the standard frequency is around 2.5 mm. The smallest drop diameter is about 15 µm. The device is designed for solid and liquid samples with densities between 0.5 and 2 g cm^{-3}.
The acoustic levitator system consists of a signal generator and the levitator. The basic parts of the levitator are the transducer (horn) and the reflector, as shown in figure 6.1(a). A piezoelectric crystal is attached to the transducer, producing an ultrasonic sound wave which is reflected by the reflector. The reflector has a concave curved surface to enhance the sound pressure level. The distance between transducer and reflector is adjusted by a micrometer screw. The generator operates at standard frequency and produces between 0.65 and 5 W power. An integrated potentiometer can be used for adjusting the transducer amplitude. The ultrasonic carrier wave can be modulated by an external signal generator connected to the ultrasonic generator.

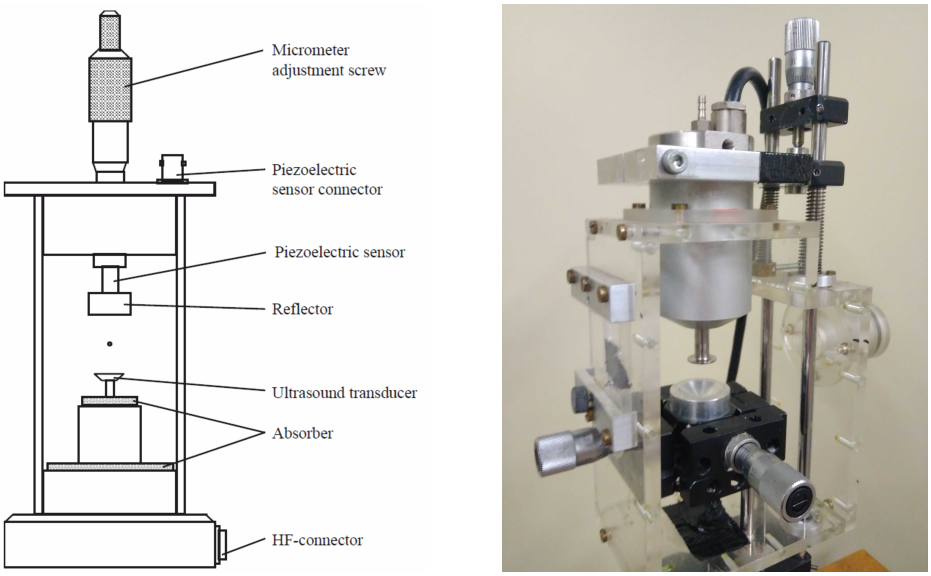

(a) (b)

Figure 6.1: (a) Basic parts of an acoustic levitator [79] and (b) a photo of the acoustic levitator used in the experiments.

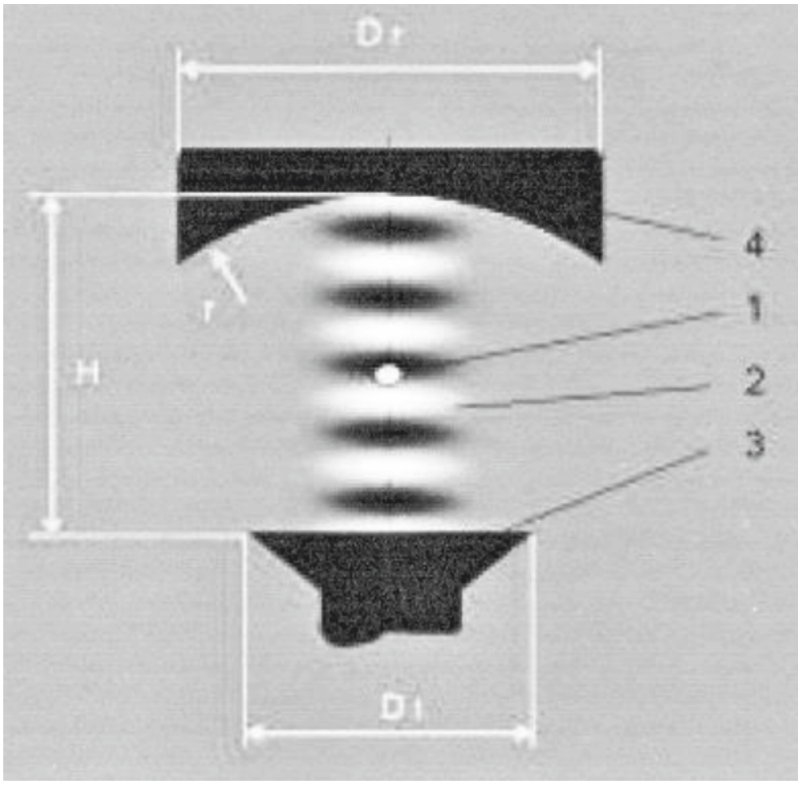

Figure 6.2: Levitated sample in a levitator [79].

The quasi-steady pressure field of the standing ultrasonic wave between the transducer and the reflector is formed if the distance between them is a multiple of the half wavelength of the ultrasound wave. At this distance, the transmitted and reflected sound waves superpose, forming regions of minimum pressure, called pressure nodes, and of maximum pressure, called pressure antinodes.
The distance between transducer and reflector was set to $5 \cdot \lambda_L/2$, which corresponds to around 15 mm. At this distance, 5 pressure nodes are formed, as shown in Figure 6.2. The pressure nodes can be visualized using fine water droplets, which will agglomerate at the pressure nodes. The optimal position for stable sample levitation is the area at the central pressure node. The outer nodes are not suitable for stable drop levitation because they are disturbed by the influences from the reflector and the transducer.

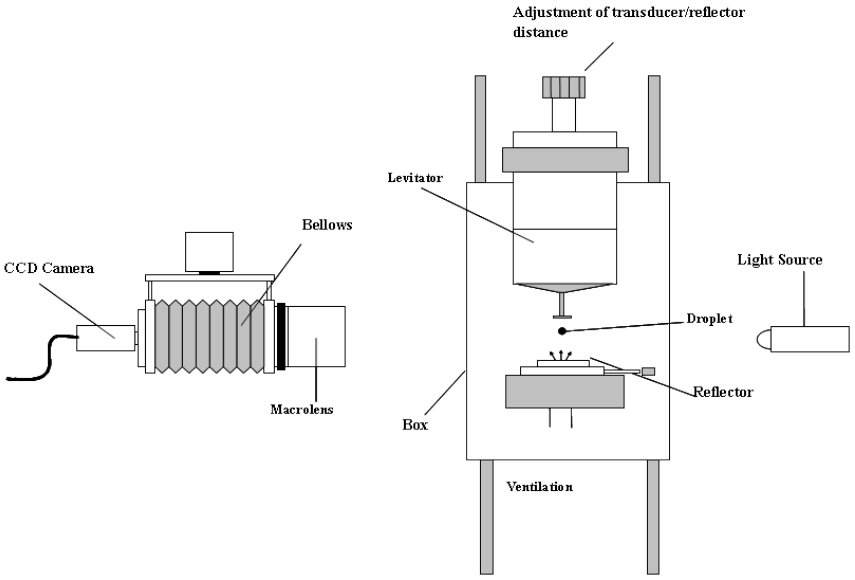

Figure 6.3: Setup for levitating single drops in an ultrasonic resonator and measuring the drop deformations in oscillations by means of image processing [13].

6.1.2 Acoustic levitation

Oscillations of the levitated object are excited by amplitude-modulating the ultrasound. Modulation frequencies up to 2 kHz are achievable with the equipment at hand. For further details, the reader is referred to [77].
A high-speed camera at a framing rate of 2 kHz under backlight illumination was used to record the images of the levitated drop. The high-speed camera was equipped with a macro lens and a tele-converter. The pixel length at a given magnification was determined from photographs of a micrometer. An uncertainty in the length measurement of ± 2 Pxls with the resolution of 300 Pxls/mm results in a sizing uncertainty of ± 6 µm, for a 1.9 mm drop, equivalent to ± 0.3 %. The resolution of 300 Pxls/mm was set for all oscillation measurements.

A syringe with a thin needle was used to produce the drops of the test liquids for the oscillation measurements. The diameters of the drops were in the range between 1 mm and 3 mm. The drop was injected into the sound field close to a pressure node of the acoustic levitator. At this time, the

amplitude modulation was switched off. Within at most 5 s after the drop has been injected in the acoustic levitator, a series of about 100 pictures of the levitated drop are recorded in order to have its initial shape. From the initial shape a equilibrium radius was first estimated and the Rayleigh frequency was calculated. The exact equilibrium radius a was calculated later in the post-processing of the recorded images. From the initial drop volume, where the evaporation of the solvent did not influence the solution concentration yet, the polymer concentration in the drop liquid at all later times can be determined.

The drop resonance frequency is then determined approximately by a modulation frequency sweep around the calculated Rayleigh frequency, revealing the drop deformations with the maximum amplitude. The drop is then excited near that resonance frequency. Then, at some time during the steady excitation, the modulation is switched off and the drop exhibited damped oscillations. During the experiments the carrier signal driving the acoustic transducer was always active.

The experiment yields both the angular frequency and the damping rate of the damped drop oscillations in a linear regime of the motion. These two values form the complex frequency α_m of the drop for the basic oscillation mode $m = 2$. Together with the calculated Rayleigh frequency $\alpha_{m,0}$ of the drop, the left-hand side of the characteristic equation (4.64) is known. This forms the basis for determining two material properties as solutions of the equation.

6.2 Complex frequency measurements

Figure 6.4 shows the late stage of the damped oscillation of a levitated 1.94 mm 0.3 wt.% Praestol 2500 aqueous solution drop. The drop was excited at 120 Hz before the modulation was switched off. From the recorded images, the frequency and damping rate in the late stage of the motion, starting at time $t = t_0$, were extracted. There the drop deformations are small, ensuring both the linear oscillation behaviour and that the influence of the shear-thinning of the polymer solution did not have any effect on the oscillation [13, 14].

6.2.1 Image processing

The recorded drop shape oscillations were processed with an image analyzing software ImageJ. Figure 6.4 shows a original image sequence of the recorded damped oscillations of a levitated 1.83 mm 0.3 wt.% Praestol 2500 aqueous solution drop. To evaluate the drop shape, the images were first binarized, and then the contour of the drop was detected. Figure 6.5 shows the processed images of the original image sequence shown in Figure 6.4. From the binarized images, the height and width of the drops as functions of time were determined.

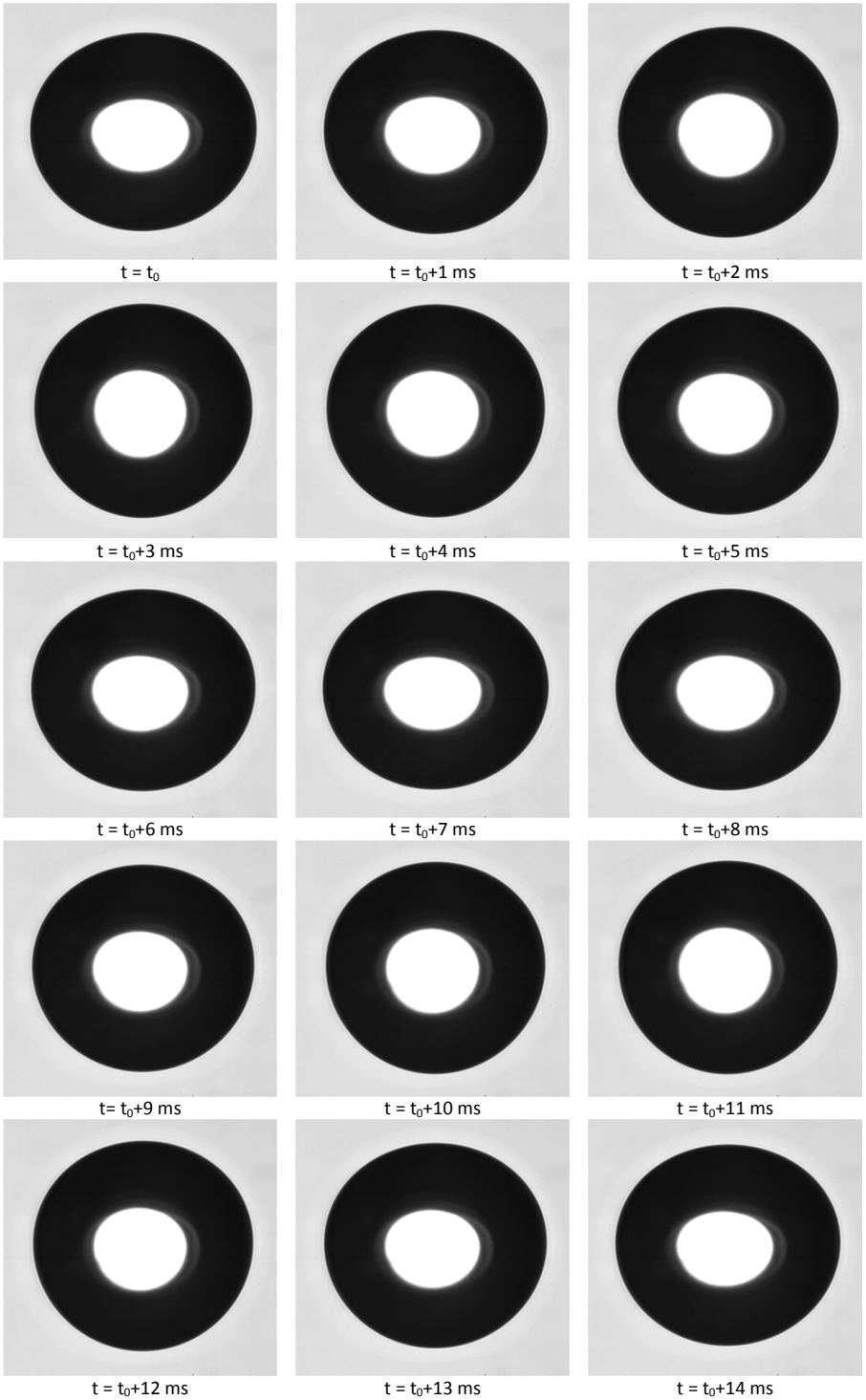

Figure 6.4: The late stage of the damped oscillations of a levitated 1.83 mm 0.3 wt.% Praestol 2500 aqueous solution drop.

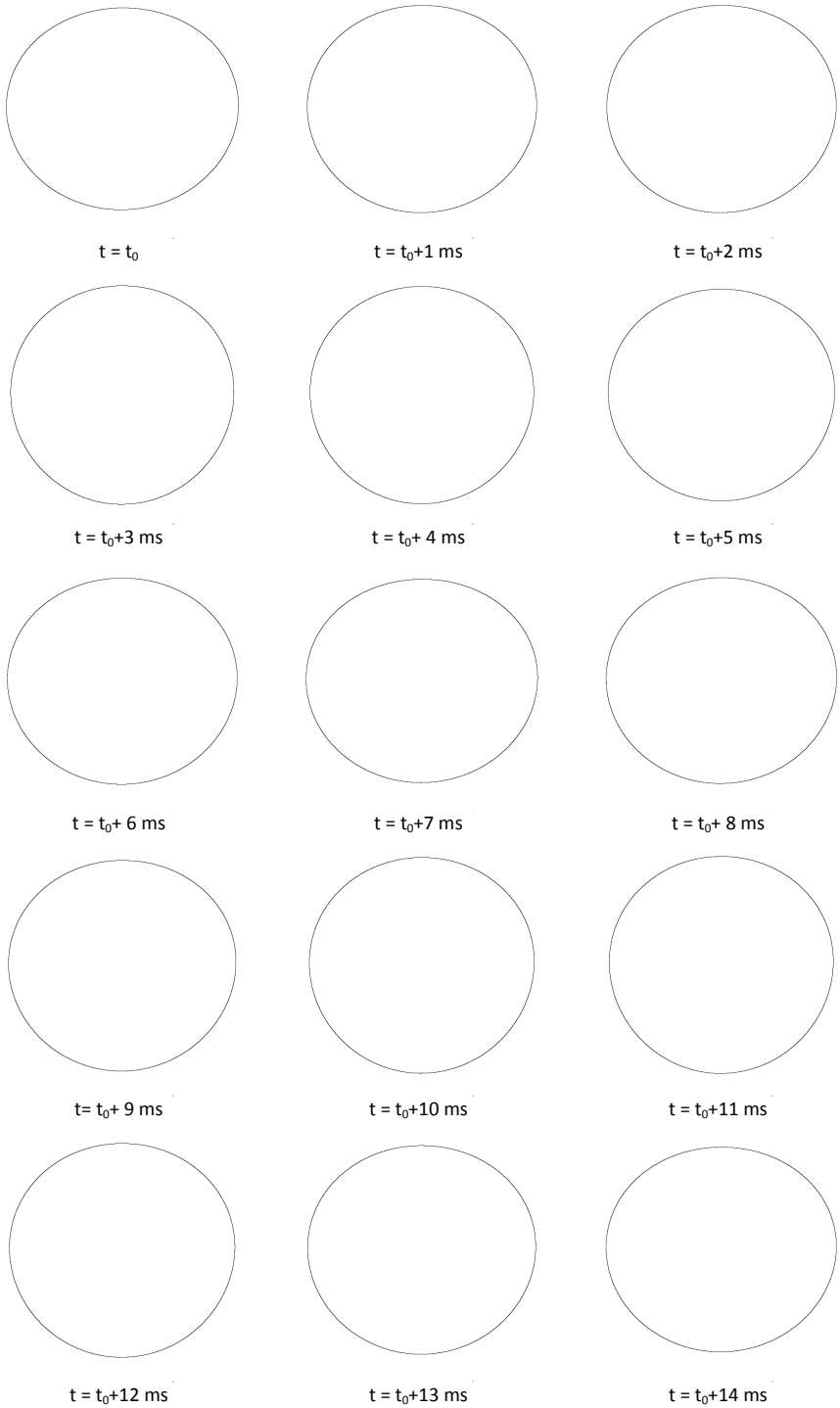

Figure 6.5: Binary images of the late stage of the damped oscillations of a levitated 1.83 mm 0.3 wt.% Praestol 2500 aqueous solution drop in Figure 6.4

6.2.2 Measurement data processing

The frequency and damping rate of the oscillating drop were determined from the last stage of the motion given by the data in figure 6.6. In the last

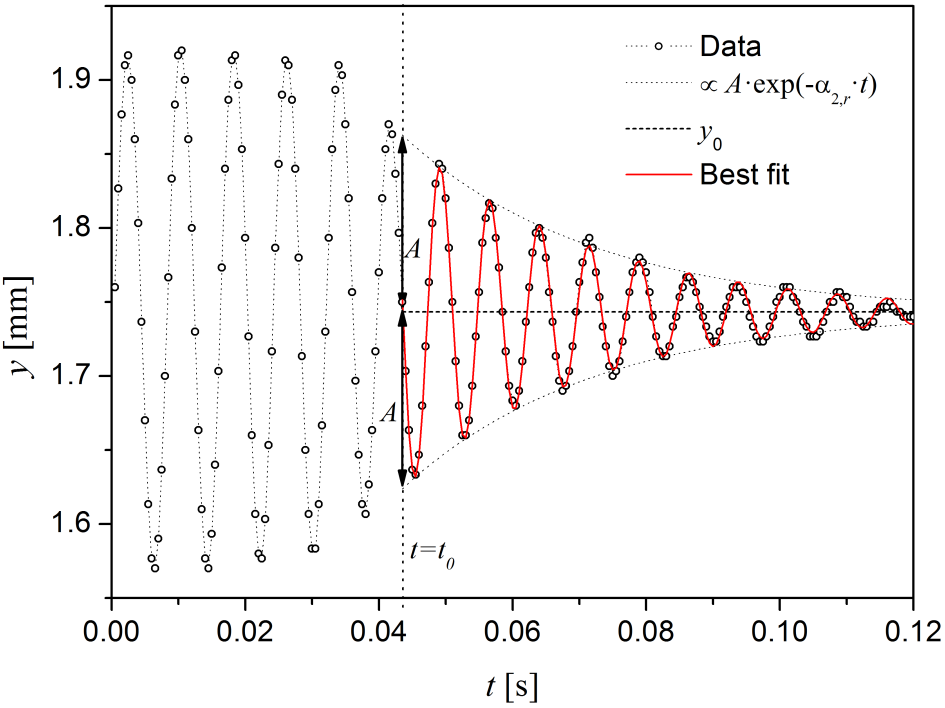

Figure 6.6: The height of a levitated 1.83 mm 0.3 *wt*% Praestol 2500 aqueous solution drop as a function of time in a damped oscillation. The time between two data points is 0.5 ms. The last part of the damped oscillation from $t_0 = 0.0435$ s on is represented by fitting the function (6.1) to the measured data.

part of motion, the linear oscillation behaviour was ensured and the shear-thinning of the polymer solution did not have any effect on the oscillation [13, 14]. The time-dependent distance $y(t)$ between the north and south poles of the drop, that is the height of the drop, and equivalently for the width of the drop, is represented by the function

$$y(t) = y_0 + A\cos\left(2\pi f \cdot t + \varphi_0\right) \cdot e^{-\alpha_{m,r}(t-t_0)} \tag{6.1}$$

which is a general description of a damped oscillation [14, 39]. In this function, y_0 is either the equilibrium height or the equilibrium width of the

drop, f is the oscillation frequency, t is time, A the oscillation amplitude at time $t = t_0$ from which on the data is modeled, and φ_0 is a reference phase angle. The least-squares method was employed to minimize the quantity $\chi^2 = \sum_i r_i^2$, where r_i are residuals giving the difference between each measured data point and its fitted value [14]. The fitting curve for the last stage of the motion of the oscillation is also shown in figure 6.6.

The fitting procedure was done on both oscillating directions, as shown in figure 6.7(a). As the result of the measurements, the average values for the frequency and the damping rate were taken. In the case of large discrepancies between the values obtained in the equatorial and polar directions, the measured results were rejected and not considered any further.
The volume-equivalent spherical radius was calculated (figure 6.7(b)) and compared to the initial radius in order to determine the correct polymer concentration. Typical variation of the volume-equivalent spherical radius during one oscillation measurement was less than 1% (figure 6.7(b)). In the case that the variations of the volume-equivalent spherical radius was larger than 1%, the measurement was rejected.
The oscillation frequency and the damping rate of the above specified drop determined by this procedure are $f = 134.2$ Hz and $\alpha_{2,r} = 36$ s^{-1}, respectively. The real and imaginary parts of the complex angular frequency $\alpha_2 = \alpha_{2,r} + i\alpha_{2,i} = \alpha_{2,r} + i2\pi f$ are therefore known.

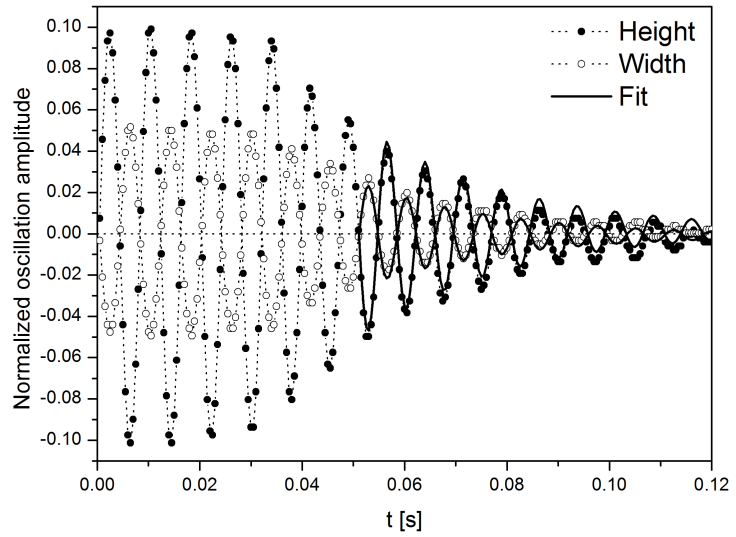

(a)

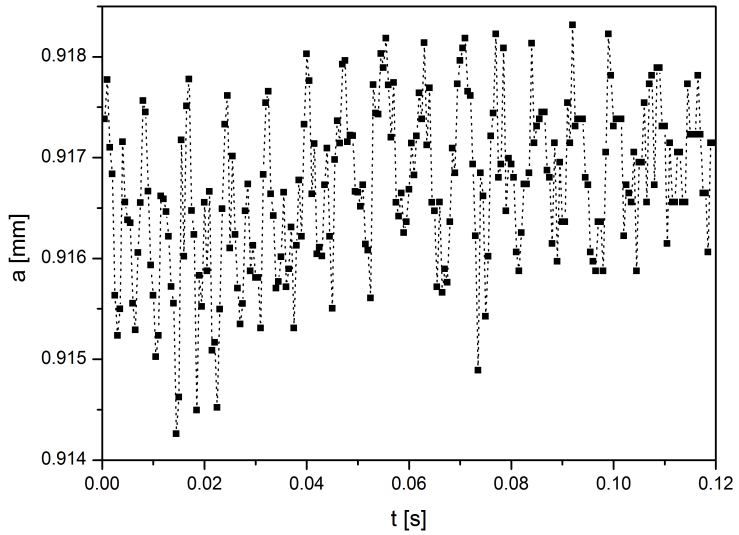

(b)

Figure 6.7: Damped oscillations of a levitated 1.83 mm 0.3 wt.% aqueous Praestol 2500 solution drop as a function of time. (a) Normalized oscillation amplitude and the fitting curve (solid line) in the last part of the motion. (b) Volume-equivalent spherical radius of the drop as a function of time, varying by no more than 0.3%.

The oscillation experiments with aqueous Praestol 2500 polymer solutions were successfully conducted with solutions with polymer mass fractions above 0.1 wt.%. For the aqueous solutions with Praestol 2500 polymer mass fractions below 0.1 wt.%, the complex frequency could not be accurately determined. Similar, for the aqueous solutions with Praestol 2540 polymer mass fractions below 0.05 wt.%, the frequency measurements did not provide consistent results. In both cases, the difference between the complex frequencies determined in the equatorial and polar directions was too large, such that their average value could not be considered as reliable.
The results of the complex frequency measurements are presented in figure 6.8. The measured non-dimensional oscillation frequencies of the drops as a function of the Ohnesorge number are shown in figure 6.8(a). For the drops with (nearly) the same Ohnesorge number, different oscillation frequencies are measured. This observation is in agreement with the results presented in figure 4.4(a). Figure 6.8(b) presents the measured non-dimensional damping rates as a function of the Ohnesorge number. Again, the measured damping rates of the drops with (nearly) the same Ohnesorge number have different values, which is in agreement with the results presented in figure 4.4(b).

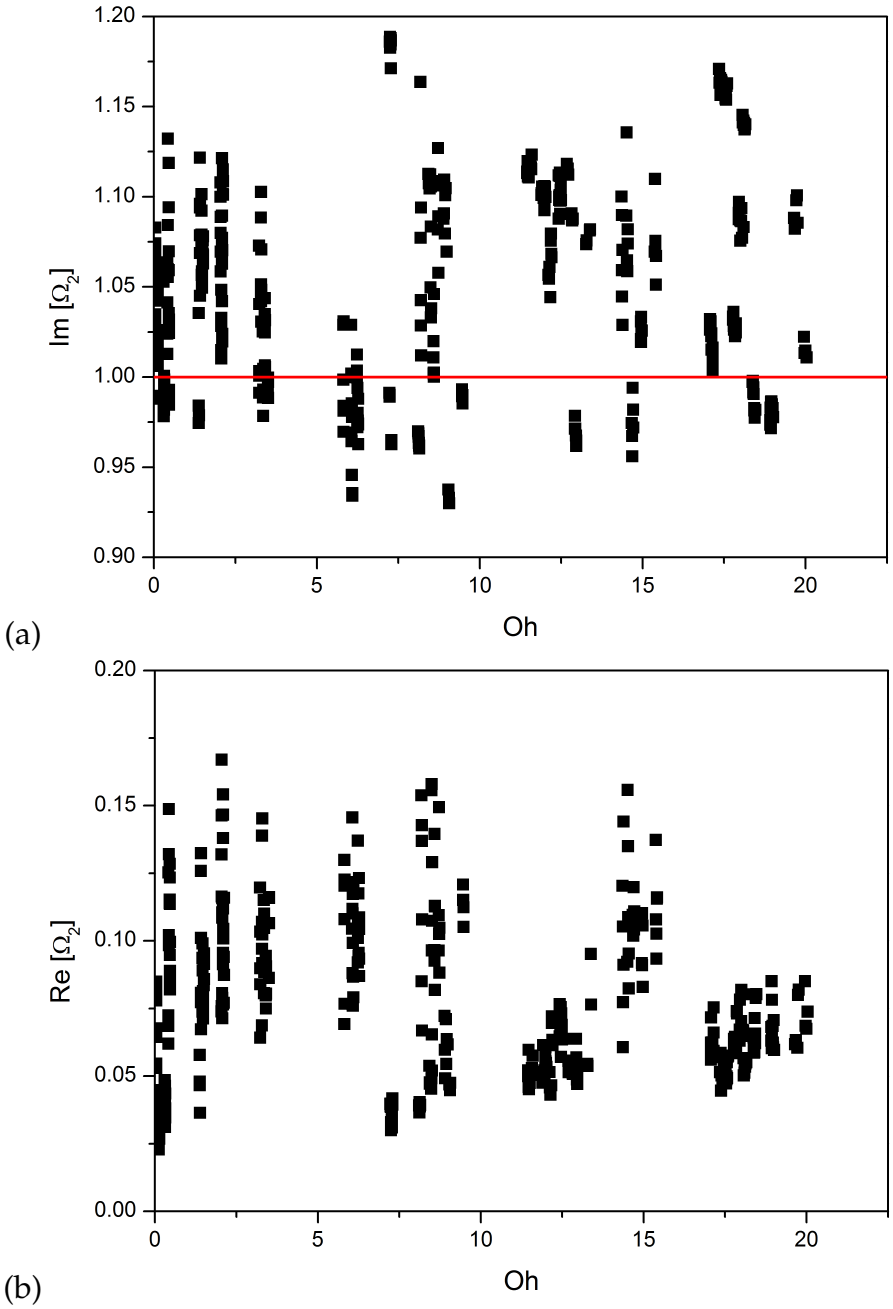

Figure 6.8: Measured non-dimensional (a) frequency and (b) damping rate as a function of the Ohnesorge number.

6.2.3 Effects on the complex frequency measurements

The presented experimental method for determining the deformation retardation time of viscoelastic liquids is based on precise measurements of the complex angular frequency of the oscillating drop. The frequency and damping rate may be potentially influenced by the acoustic levitation technique, the non-spherical static drop shape, the non-linear drop shape oscillations and the shear thinning behaviour of the liquid [13, 26, 39, 77, 80, 81].
In the levitated drop, an internal liquid circulation may be induced by the acoustic streaming of the unsteady boundary layer flow of the surrounding air [77]. This acoustically induced velocity field inside the levitated droplet may influence the measurements. As was shown in [13], the maximal acoustically induced angular velocity at the drop surface is two orders of magnitude lower than the oscillation-induced liquid velocity u_θ given by (4.49). Thus, the effect of the acoustic streaming is neglected in the present work.
The frequency and the damping rate of the oscillating drop may also be influenced by the non-spherical equilibrium drop shape and by the oscillation amplitude [13, 26, 39, 81]. In the present work, a spherical equilibrium drop shape is assumed. The sound pressure in the acoustic levitator may cause a deviation from the spherical shape of the drop. The non-spherical drop shape is characterized by the aspect-ratio, here defined as the ratio of the equatorial and polar radii of the drop in equilibrium. For viscous drops, Kremer *et al.* [39] investigated the effect of the aspect ratio on the shift of the resonance frequency and damping rate from the calculated values for the spherical drop. For aspect ratios up to 1.5, the shift in the resonance frequency was about 3 %, and the shift in the damping rate was about 6% [39]. Similar, though slightly higher values of about 8%, were reported by Trinh *et al.* [81], for drops in a liquid-liquid system. In the present work the static aspect ratios are between 1.1 and 1.2. Therefore, the influence of the oblate equilibrium drop shape on the resonance frequency and damping rate is negligible [13].
At sufficiently large amplitudes of oscillation, nonlinear effects influence the oscillation frequency and the damping rate [13]. Becker *et al.* [26] experimentally and theoretically investigated large-amplitude oscillations of liquid drops. They concluded that, if the amplitude of drop oscillation exceeds

approximately 10 % of the droplet radius, nonlinear effects are observed. Similar conclusions were made by Kremer *et al.* [39], where they recommend that the oscillation amplitude should be between 5% and 15%. Therefore, in the presented experiments the oscillation amplitudes of drops were always kept below 10 % in order to avoid nonlinear effects.
The theoretical framework of linear drop shape oscillations requires small oscillation-induced shear rates to avoid shear thinning behaviour of the test liquids. The onset of the shear thinning behaviour can be seen in figures 5.5 and **??**, where the flow curves for aqueous P2500 and P2540 polymer solutions are presented. In the case of aqueous P2540 solutions, the onset of shear thinning is $O(0.1\ \mathrm{s}^{-1})$ and for the aqueous P2500 solutions, the onset of shear thinning lies between 0.1 s^{-1} and 1 s^{-1}, depending on the polymer mass fraction. Brenn and Teichtmeister [13] calculated the time and volume averaged shear rate in the drop of aqueous solutions prepared with the same polymer batches as used in the present work. They calculated the averaged shear rate of $O(15\ \mathrm{s}^{-1})$ which lies in the shear thinning region. However, as remarked in [13], the averaged shear rate values do not correspond to the experimental observations that the measurements may yield correct results.

6.3 Determination of the polymeric time scales

The characteristic equation (4.64) is transcendental in the argument of the spherical Bessel functions involved and must therefore be solved numerically [13, 14]. The method for determining pairs (η_0, λ_2) or (λ_1, λ_2) was presented in the previous section. As a prerequisite, the complex frequency α_2 must be accurately measured in the experiment, and the radius of the drop as well as the density, stress relaxation time and surface tension of the liquid in contact with the ambient air must be known [14]. The accuracy requirements to these input parameters are addressed in the section below.

As explained in detail in section 4.3.2, the first step to determine the deformation retardation time is to solve the characteristic equation for the complex argument qa. Next, from the set of solutions qa the corresponding pairs (η_0, λ_2) and/or (λ_1, λ_2) are calculated. Finally, the identification of the

Argument qa	Zero-shear viscosity η_0 [Pa s]	Retardation time λ_2 [10^{-4} s]	Relaxation time λ_1 [s]	Retardation time λ_2 [10^{-4} s]
4.948 + 0.088i	2.360	1.29	0.0036	-2.448
5.824 + 7.846i	0.0006	2243	3969	$281 \cdot 10^4$
8.757 + 0.055i	0.754	1.018	0.011	-0.073
12.113 + 0.0361i	0.394	0.94	0.022	0.440
15.363 + 0.0228i	0.245	0.904	0.035	0.650
18.57 + 0.0147i	0.168	0.888	0.051	0.760
21.755 + 0.0098i	0.122	0.880	0.07	0.827
24.928 + 0.0068i	0.093	0.876	0.092	0.871
28.094 + 0.0049i	0.073	0.873	0.117	0.901
31.254 + 0.0036i	0.059	0.872	0.144	0.923
34.411 + 0.0027i	0.049	0.871	0.175	0.939
37.565 + 0.0021i	0.041	0.870	0.208	0.951

Table 6.1: Positive roots qa of the characteristic equation (4.64) and corresponding calculated pairs (η_0, λ_2) and (λ_1, λ_2) for a 0.3 wt.% aqueous Praestol 2500 solution drop with equilibrium radius $a = 0.917$ mm. The highlighted row represents the correct solutions.

correct solution follows from comparison of the calculated values η_0 or λ_1 with the values of η_0^* or λ_1^*, respectively.
For a 0.3 wt.% aqueous Praestol 2500 solution drop with equilibrium radius $a = 0.917$ mm and measured complex frequency $\alpha_2 = 36.24\ \mathrm{s}^{-1} + i2\pi \cdot 134.2$ Hz, described in the previous section, the solutions qa of the characteristic equation and the corresponding calculated pairs (η_0, λ_2) and (λ_1, λ_2) are listed in Table 6.1.
The result for the zero-shear dynamic viscosity η_0 obtained for this liquid is 0.093 Pa s, which deviates from the value of η_0^* of 0.089 Pa s measured by rotational rheometer by no more than 5%. The corresponding deformation retardation time is $0.88 \cdot 10^{-4}$ s. Similar, the calculated stress relaxation time λ_1 is 0.092 s which deviates from the value of λ_1^* of 0.095 s revealed by elongational rheometry by no more than 3%. The corresponding deformation retardation time is $0.87 \cdot 10^{-4}$ s.

7 Results and discussion

7.1 Uncertainty and sensitivity analysis

In this section the sensitivity of the calculated pairs (η_0, λ_2) and (λ_1, λ_2) to uncertainties of the parameters entering the characteristic equation (4.64) is analyzed.

The complex roots qa of the characteristic equation (4.64) are calculated to machine accuracy with the computer software MATHEMATICA [14].
For the input parameters the normal (Gaussian) distribution is assumed, and their estimated uncertainties are as follows. The measured zero-shear viscosity η_0^* and the stress relaxation time λ_1^* have an uncertainty of $\pm$ 10%. The Rayleigh frequency is calculated as $\alpha_{m,0} = \sqrt{m(m-1)(m+2)}\sqrt{\sigma/\rho a^3}$, where the uncertainty of the measured radius a is below $\pm$1 %, the uncertainty in the density is below $\pm$0.05 %, and the uncertainty in the surface tension is around $\pm$10 %. This results in the uncertainty of about $\pm$5 % for the Rayleigh frequency $\alpha_{2,0}$ of the mode $m = 2$. The measured complex frequency $\alpha_2 = \alpha_{2,r} + i\alpha_{2,i} = \alpha_{2,r} + i2\pi f$ has an uncertainty of $\pm$ 10% in the damping rate $\alpha_{2,r}$ and an uncertainty of $\pm$1% in the oscillation frequency f. This follows from the analysis of the fitting results of the function in equation (6.1) to the measured data.

The uncertainties of (η_0, λ_2) and (λ_1, λ_2) were determined by variation of the input parameters. This was achieved with a MATHEMATICA routine which solved the characteristic equation (4.64) 5000 times, randomly selecting the normal distributed input parameters. The solutions were first searched near the correct solution qa. For the case of the 0.3 wt.% Praestol 2500 solution drop detailed in the previous sections, the correct solution was identified at $qa = 24.928 + 0.0068i$. However, it is reasonable to expect that

the correct solution could correspond to a different qa, for example, in the case of large uncertainties. For this reason the neighboring solutions of $qa = 24.928 + 0.0068i$ at $qa = 21.755 + 0.0098i$ and $qa = 28.094 + 0.0049i$ (Table 6.1) were also analyzed. The results of the present sensitivity analysis are the mean values and the corresponding probability density functions of η_0, λ_1 and λ_2 obtained from the pairs (η_0, λ_2) and (λ_1, λ_2) calculated near the three different values of the complex argument qa, as shown in figures 7.1 and 7.2. The real part of these three arguments, $\mathrm{Re}(qa) \approx 21.7$, $\mathrm{Re}(qa) \approx 24.9$ and $\mathrm{Re}(qa) \approx 28.0$ are used as an identifier to distinguish the results obtained for different solutions qa. The results of the sensitivity analysis are also listed in table 7.1.

First we consider the results obtained by solving the characteristic equation (4.64) for the pair (η_0, λ_2). Figure 7.1(a) shows the probability density function of the normally distributed η_0 calculated at $\mathrm{Re}(qa) \approx 21.7$, $\mathrm{Re}(qa) \approx 24.9$ and $\mathrm{Re}(qa) \approx 28.0$. The corresponding values are $\eta_0 = 0.12(1 \pm 11\%)$ Pa s, $\eta_0 = 0.09(1 \pm 10\%)$ Pa s and $\eta_0 = 0.07(1 \pm 10\%)$ Pa s, respectively. The zero-shear-rate viscosity η_0 obtained near $\mathrm{Re}(qa) \approx 24.9$ is in excellent agreement with the value $\eta_0^* = 0.089$ Pa s from shear rheometry. On the other hand, the mean values of η_0 calculated at $\mathrm{Re}(qa) \approx 21.7$ and $\mathrm{Re}(qa) \approx 28.0$ are more than one standard deviation away from the value η_0^*. The results show that η_0 depends strongly on the solution qa of the characteristic equation. This observation is in accordance with equation (4.74).
Figure 7.1(b) shows the probability density function of the normally distributed λ_2 calculated at $\mathrm{Re}(qa) \approx 21.7$, $\mathrm{Re}(qa) \approx 24.9$ and $\mathrm{Re}(qa) \approx 28.0$. The corresponding values are $\lambda_2 = 0.91 \cdot 10^{-4}(1 \pm 13\%)$ s, $\lambda_2 = 0.90 \cdot 10^{-4}(1 \pm 13\%)$ s and $\lambda_2 = 0.90 \cdot 10^{-4}(1 \pm 14\%)$ s, respectively. It is evident that nearly the same result for λ_2 is obtained at different values of the solution qa. This weak dependence of λ_2 on the solution qa is in accordance with equation (4.73).

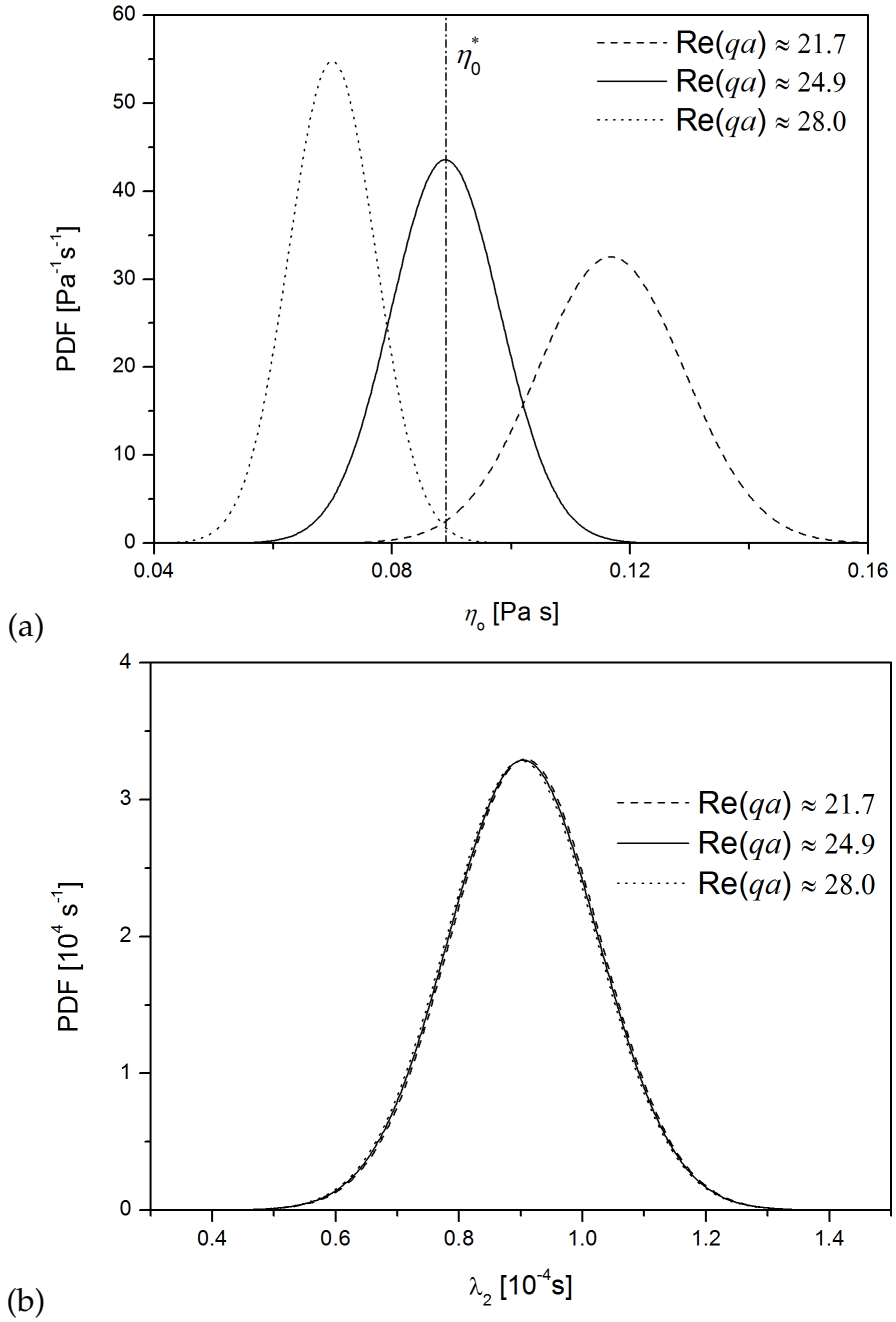

Figure 7.1: The uncertainties of the calculated pair (η_0, λ_2). The probability density function of the normally distributed (a) zero-shear-rate viscosity η_0 and (b) the deformation retardation time λ_2, calculated for three different values of qa.

Next we consider the results obtained by solving the characteristic equation (4.64) for the pair (λ_1, λ_2). Figure 7.2(a) shows the probability density function of the normally distributed λ_1 calculated at $\mathrm{Re}(qa) \approx 21.7$, $\mathrm{Re}(qa) \approx 24.9$ and $\mathrm{Re}(qa) \approx 28.0$. The corresponding values are $\lambda_1 = 0.072(1 \pm 10\%)$ s, $\lambda_1 = 0.095(1 \pm 10\%)$ s and $\lambda_1 = 0.12(1 \pm 10\%)$ s, respectively. The mean value of the stress relaxation time λ_1 obtained near $\mathrm{Re}(qa) \approx 24.9$ is in excellent agreement with the value $\lambda_1^* = 0.095$ s from elongational rheometry. Figure 7.2(b) shows the probability density function of the normally distributed λ_2 calculated at $\mathrm{Re}(qa) \approx 21.7$, $\mathrm{Re}(qa) \approx 24.9$ and $\mathrm{Re}(qa) \approx 28.0$. The corresponding values are $\lambda_2 = 0.85 \cdot 10^{-4}(1 \pm 13\%)$ s, $\lambda_2 = 0.90 \cdot 10^{-4}(1 \pm 12\%)$ s and $\lambda_2 = 0.93 \cdot 10^{-4}(1 \pm 12\%)$ s, respectively. Although the results show a rather weak dependence of λ_2 on the solution qa, the deviation between the calculated mean values is less than 10%.

	(η_0, λ_2)		(λ_1, λ_2)	
$\mathrm{Re}(qa)$	η_0 [Pa s]	λ_2 [10^{-4} s]	λ_1 [s]	λ_2 [10^{-4} s]
≈ 21.7	$0.12\ (1 \pm 11\%)$	$0.91(1 \pm 13\%)$	$0.072(1 \pm 10\%)$	$0.85(1 \pm 13\%)$
≈ 24.9	$0.090\ (1 \pm 10\%)$	$0.90(1 \pm 13\%)$	$0.095(1 \pm 10\%)$	$0.90(1 \pm 12\%)$
≈ 28.0	$0.070\ (1 \pm 10\%)$	$0.90(1 \pm 14\%)$	$0.12(1 \pm 10\%)$	$0.93(1 \pm 12\%)$

Table 7.1: Results of the sensitivity analysis obtained by variation of the input parameters. Pairs of (η_0, λ_2) and (λ_1, λ_2) calculated near three different solutions qa for the case of the investigated aqueous 0.3 wt.% Praestol 2500 solution drop. The highlighted row represents the correct solutions.

The presented error analysis yields similar results for all the aqueous polymer solutions studied here. The main motivation of this thesis is to develop a reliable and precise experimental method to measure the deformation retardation time λ_2 of polymer solutions. From the presented uncertainty analysis follows that λ_2 can be accurately measured even if the right solution qa of the characteristic equation cannot unambiguously be identified [14]. This is due to the rather weak dependency of λ_2 on the solution qa of the characteristic equation (4.64). On the other hand, in order to accurately determine the zero-shear-rate viscosity η_0 or the stress relaxation time λ_1, accurate and precise measurements of all the input parameters are required [14].

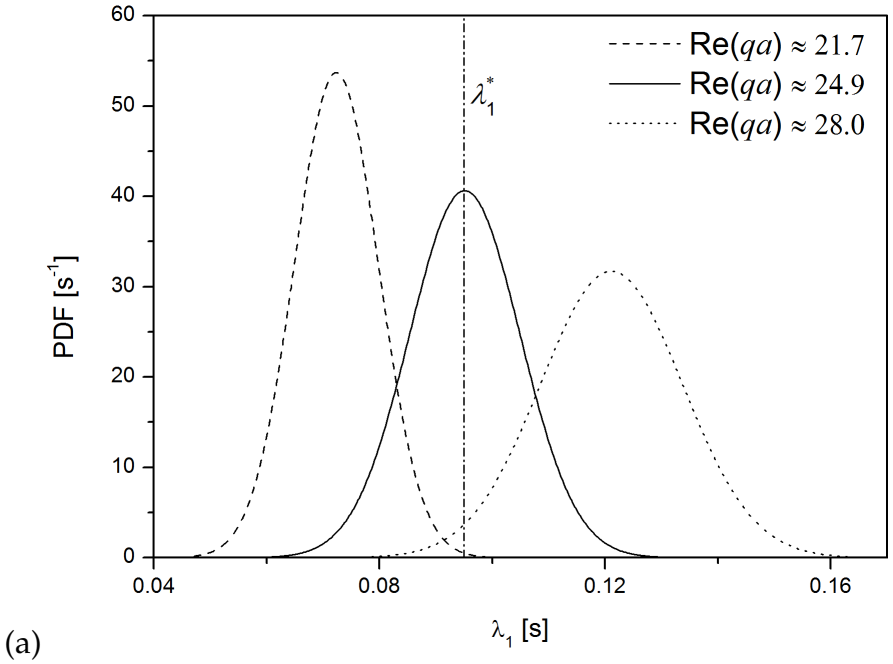

(a)

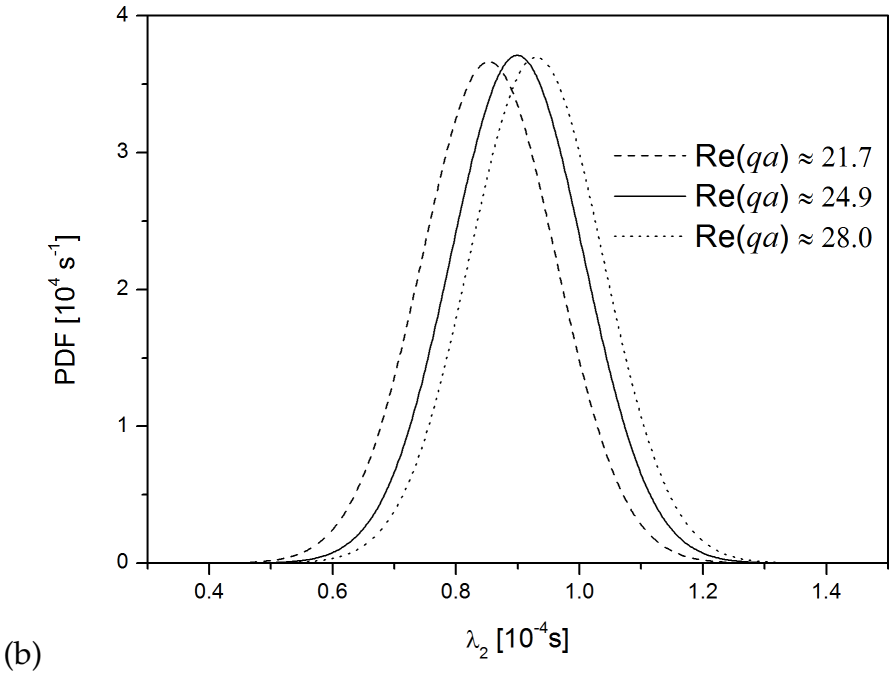

(b)

Figure 7.2: The uncertainties of the calculated pair (λ_1, λ_2) . The probability density function of the normally distributed (a) stress relaxation time λ_1 and (b) the deformation retardation time λ_2, calculated for three different values of qa.

7.2 Results and discussion

With each of the aqueous polymer solutions, a set of at least 30 oscillation experiments were performed. The polymer solutions were contained in 250 ml plastic bottles, from which the test liquid was sampled by a syringe. At least five different samples were taken from each polymer solution. From each sample, one or two drops were levitated. With a single drop a series of oscillation measurements in immediate succession were performed, varying the excitation frequency. In case that the polymer mass fraction in the drop liquid is more than 10 % higher than the nominal polymer mass fraction, due to the solvent evaporation, the corresponding oscillation measurement was rejected.

Aqueous Praestol 2500 solutions

The results of the drop oscillation experiments with aqueous Praestol 2500 solutions are presented in figures 7.3-7.5 and listed in tables 7.2 and 7.3.

First, the values of zero-shear-rate viscosity and stress relaxation time obtained from the drop oscillation experiments are presented. Pairs of (η_0, λ_2) and (λ_1, λ_2) of the investigated aqueous P2500 solutions obtained by the oscillating drop method are listed in table 7.2. Both pairs provide similar values of λ_2 which differ by no more than 5%.
Figure 7.3(a) shows the values of zero-shear-rate viscosity obtained from the drop oscillation experiments (η_0) and from the shear rheometry (η_0^*) against the Praestol 2500 polymer mass fraction. The results show excellent agreement within $\pm 10\%$ between the two methods, except in the case of high polymer mass fractions (0.9 wt.% and 1 wt.%).
Figure 7.3(b) shows the values of stress relaxation time λ_1 as measured by drop oscillations and λ_1^* from elongational rheometry against the Praestol 2500 polymer mass fraction. Again, the results show excellent agreement within $\pm 10\%$ between the two methods, except in the case of high polymer mass fractions (0.9 wt.% and 1 wt.%).
The discrepancy between the methods at high polymer mass fractions could be due to the experimental error of the complex angular frequency measurements and due to the uncertainty of the measured liquid properties.

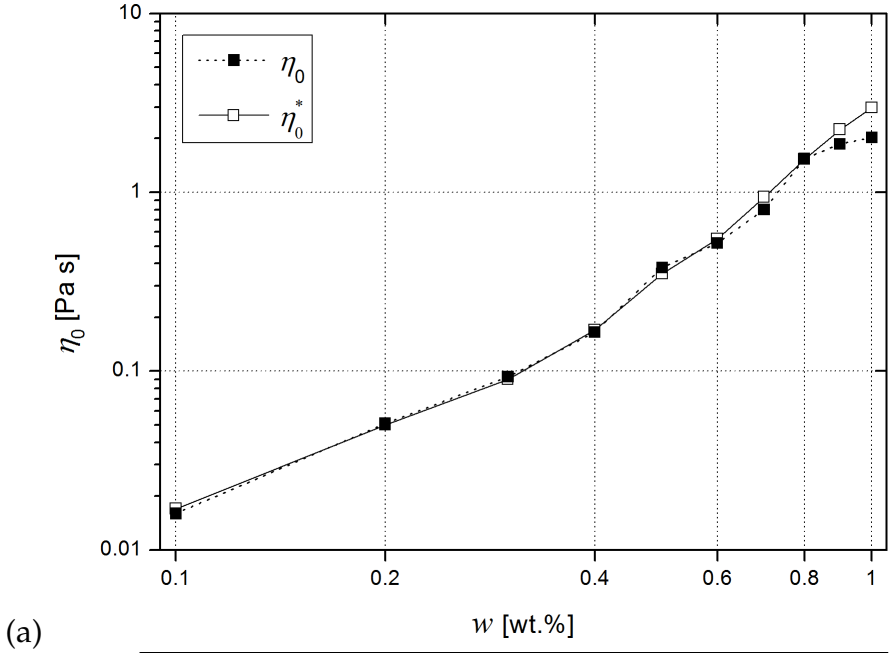

(a)

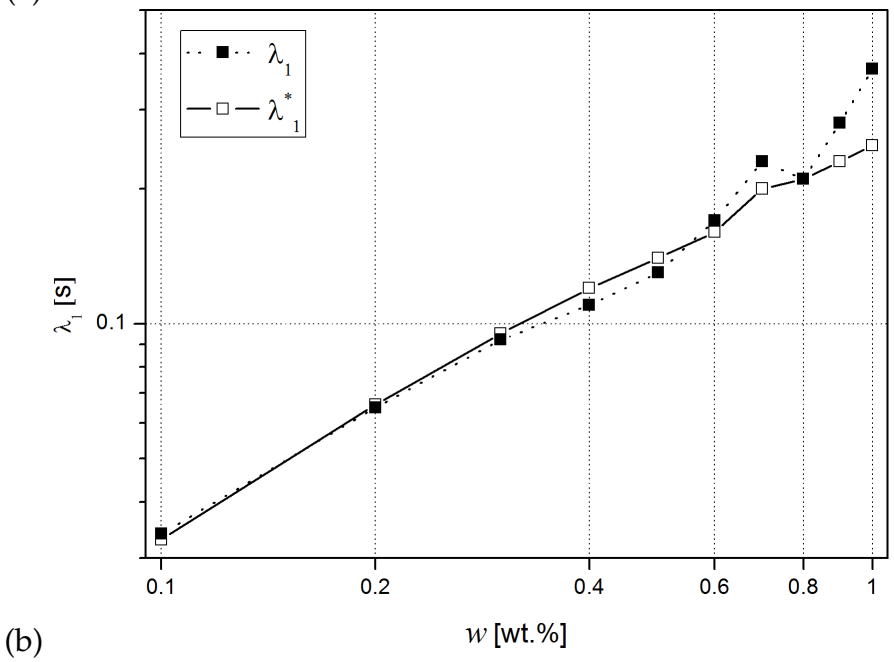

(b)

Figure 7.3: (a) Zero-shear-rate viscosity η_0 as measured by drop oscillations and η_0^* from shear rheometry and (b) stress relaxation time λ_1 as measured by drop oscillations and λ_1^* from elongational rheometry against the Praestol 2500 mass fraction w.

w [wt.%]	η_0^* [Pa s]	λ_1^* [s]	η_0 [Pa s]	λ_2 [10^{-4} s]	λ_1 [s]	λ_2 [10^{-4} s]
0.1	0.017	0.033	0.016	0.4	0.034	0.4
0.2	0.051	0.066	0.051	0.5	0.065	0.5
0.3	0.089	0.095	0.093	0.9	0.092	0.9
0.4	0.17	0.11	0.165	2.2	0.11	2.3
0.5	0.35	0.14	0.38	2.0	0.13	1.9
0.6	0.55	0.16	0.52	2.5	0.17	2.5
0.7	0.94	0.20	0.8	2.6	0.23	2.6
0.8	1.53	0.21	1.54	2.8	0.21	2.8
0.9	2.24	0.23	1.86	2.9	0.28	2.9
1.0	2.97	0.25	2.03	2.7	0.37	2.8

Table 7.2: Pairs of (η_0, λ_2) and (λ_1, λ_2) of the investigated aqueous P2500 solutions at 22 °C obtained by the oscillating drop method. Values of η_0^* and λ_1^* are added for comparison.

The deformation retardation time λ_2 is determined from the measured pairs of (η_0, λ_2) or (λ_1, λ_2) (see table 7.2). Both pairs provide similar values of λ_2 ($\pm 5\%$). Measured deformation retardation time λ_2 and calculated $\lambda_{2,EVSS}$ of the investigated aqueous P2500 solutions are presented in figure 7.4 and listed in table 7.3.

Figure 7.4 shows the measured λ_2 and calculated $\lambda_{2,EVSS}$ (3.36) against the Praestol 2500 mass fraction. The λ_2 obtained by the oscillating drop method is of the order of 10^{-4} s and increases monotonically with the polymer mass fraction w. In contrast, the deformation retardation time obtained by the stress-splitting approach $\lambda_{2,EVSS}$ shows a different trend, namely, a decrease with increasing polymer mass fraction. There is a narrow range of polymer mass fractions around 0.7 wt.% where the measured values of the deformation retardation time λ_2 agree with the calculated ones $\lambda_{2,EVSS}$. This is rather by a coincidence [14].

w [wt.%]	λ_2 [10^{-4} s]	$\lambda_{2,EVSS}$ [10^{-4} s]	λ_2/λ_1^*	$\lambda_{2,EVSS}/\lambda_1^*$
0.1	0.4	19.4	0.0012	0.059
0.2	0.5	13.2	0.0008	0.02
0.3	0.9	10.6	0.0009	0.011
0.4	2.3	6.5	0.0021	0.0059
0.5	1.9	4.0	0.0013	0.0029
0.6	2.5	2.9	0.0015	0.0018
0.7	2.6	2.1	0.0013	0.0011
0.8	2.8	1.4	0.0013	0.0007
0.9	2.9	1.0	0.0013	0.0004
1.0	2.7	0.84	0.0011	0.0003

Table 7.3: Measured deformation retardation time λ_2 and calculated $\lambda_{2,EVSS}$ of the investigated aqueous P2500 solutions.

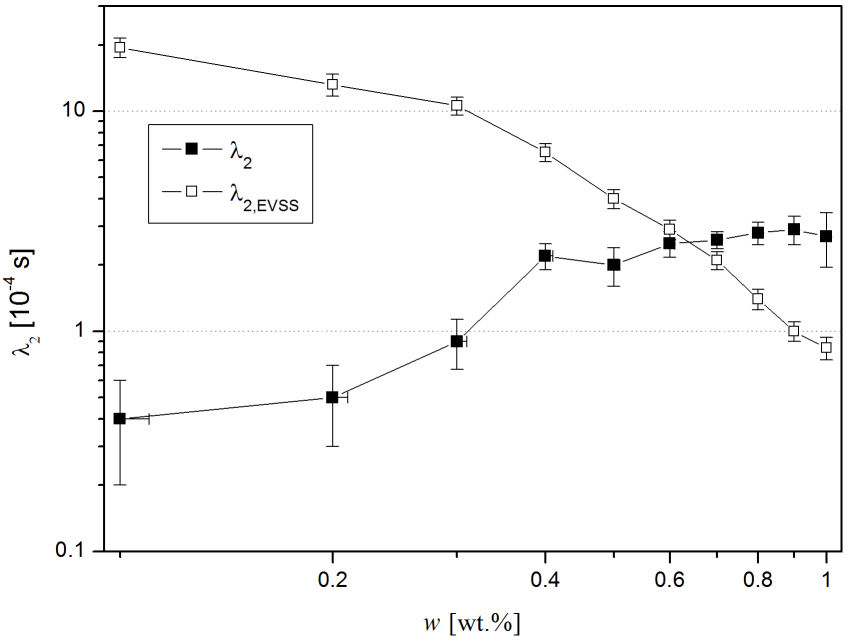

Figure 7.4: Measured deformation retardation time λ_2 and calculated $\lambda_{2,EVSS}$ against polymer mass fraction for aqueous P2500 solutions.

In simulations of viscoelastic fluid flow, the ratio of the deformation retardation time to the stress relaxation time is often set to $\lambda_2/\lambda_1 = 0.1$ [10]. In the present study, however, the values of λ_2/λ_1 are found to be of the order of 10^{-3}. Figure 7.5 shows the values of λ_2/λ_1 against the Praestol 2500 mass fraction, where the stress relaxation time from elongational rheometry was used (λ_1^*). For the values λ_2 of the deformation retardation time obtained from the oscillation experiments, the ratio λ_2/λ_1^* is nearly constant with a mean value of about $1.3 \cdot 10^{-3}$. For the calculated values of the deformation retardation time $\lambda_{2,EVSS}$, the ratio $\lambda_{2,EVSS}/\lambda_1^*$ monotonically decreases with increasing polymer mass fraction from about $6 \cdot 10^{-2}$ for the lowest polymer mass fraction to $3 \cdot 10^{-4}$ for the highest polymer mass fraction.

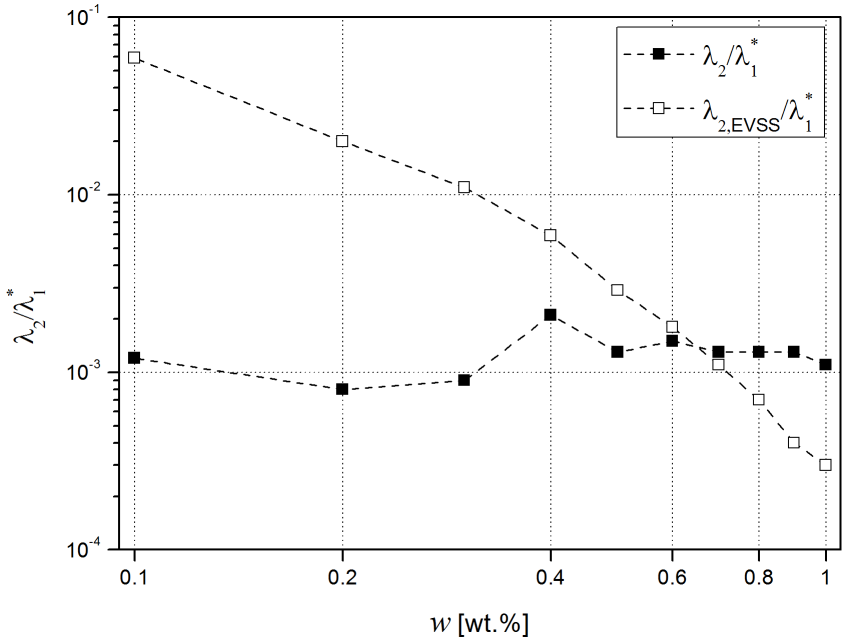

Figure 7.5: Values of λ_2/λ_1^* and $\lambda_{2,EVSS}/\lambda_1^*$ against polymer mass fraction for aqueous P2500 solutions.

The excellent agreement between η_0 and η_0^* (figure 7.3(a)), and between λ_1 and λ_1^* (figure 7.3(b)), and the fact that the pairs (η_0, λ_2) and (λ_1, λ_2) provide the same value of λ_2, leads to the conclusion, that the proposed method provides a reliable tool for measuring different material properties of viscoelastic solutions of flexible polymers.

Aqueous Praestol 2540 solutions

The results of the drop oscillation experiments with aqueous Praestol 2540 solutions are presented in figures 7.6-7.8 and tables 7.4 and 7.5. Only the aqueous solutions with Praestol 2540 polymer mass fractions above 0.03 wt.% are considered, for reasons explained in the previous section.
Pairs of (η_0, λ_2) and (λ_1, λ_2) of the investigated aqueous P2540 solutions obtained by the oscillating drop method are listed in table 7.4. Figure 7.6(a) shows the values of the zero-shear-rate viscosity obtained from the drop oscillation experiments (η_0) and from shear rheometry (η_0^*) against the polymer mass fraction. Considering all the uncertainties of the input parameters, the agreement between the two methods is good. In the case of the 0.07 wt.% P2540 mass fraction, the agreement is within 1%, while for the 0.05 wt.% polymer mass fraction the agreement is within 17%. For the 0.1 wt.% P2540 mass fraction, the deviation between the methods is about 5%.
Figure 7.6(b) shows the values of stress relaxation time λ_1 as measured by drop oscillations and λ_1^* from elongational rheometry against the Praestol 2540 polymer mass fraction. Again, the results show excellent agreement within $\pm$10% between the two methods. In the case of the 0.1 wt.% P2540 mass fraction the agreement is within 1%.

w [wt.%]	η_0^* [Pa s]	λ_1^* [s]	η_0 [Pa s]	λ_2 [10^{-4} s]	λ_1 [s]	λ_2 [10^{-4} s]
0.05	2.09	0.08	2.45	1.3	0.07	1.3
0.07	3.11	0.11	3.14	1.7	0.10	1.7
0.10	4.45	0.15	4.65	1.8	0.15	1.8

Table 7.4: Pairs of (η_0, λ_2) and (λ_1, λ_2) of the investigated aqueous P2540 solutions at 22 °C obtained by the oscillating drop method. Values of η_0^* and λ_1^* are added for comparison.

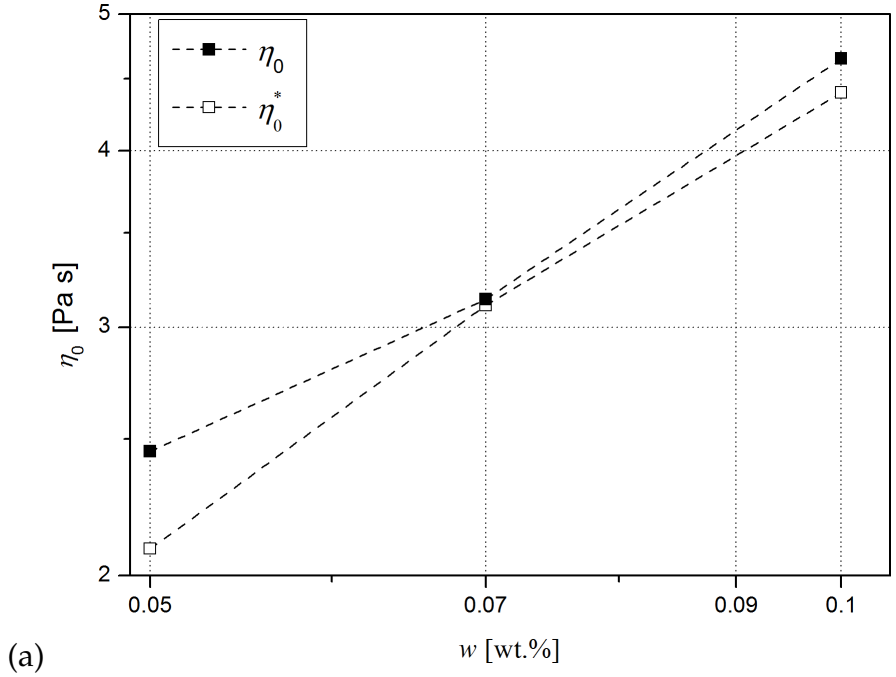

(a)

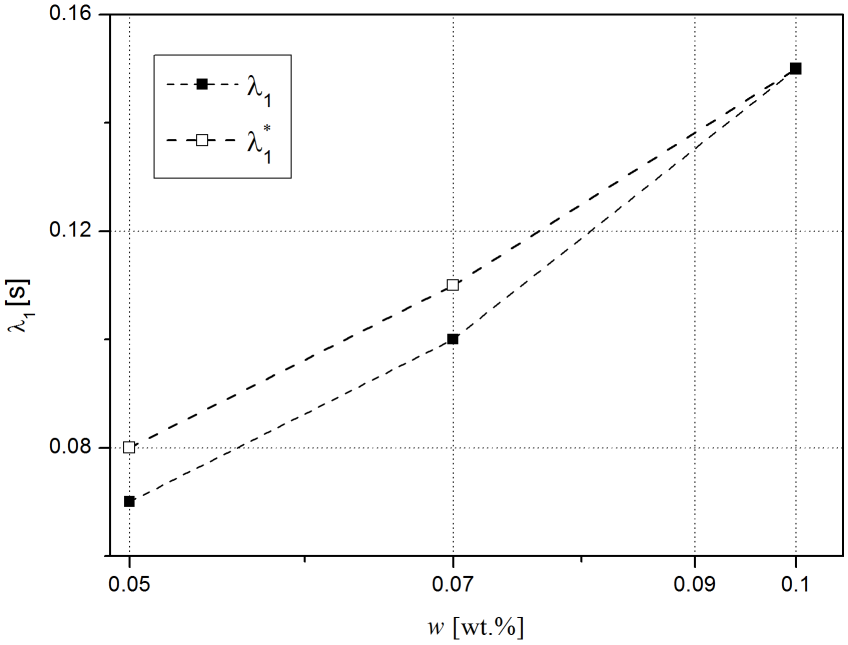

(b)

Figure 7.6: (a) Zero-shear-rate viscosity η_0 as measured by drop oscillations and η_0^* from shear rheometry and (b) stress relaxation time λ_1 as measured by drop oscillations and λ_1^* from elongational rheometry against the Praestol 2540 mass fraction w.

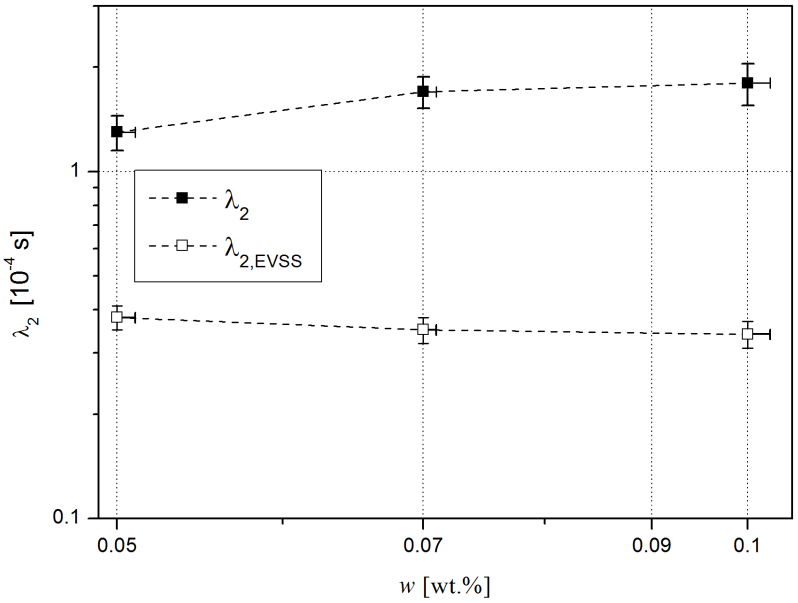

Figure 7.7: Measured deformation retardation time λ_2 and calculated $\lambda_{2,EVSS}$ against polymer mass fraction for aqueous P2540 solutions.

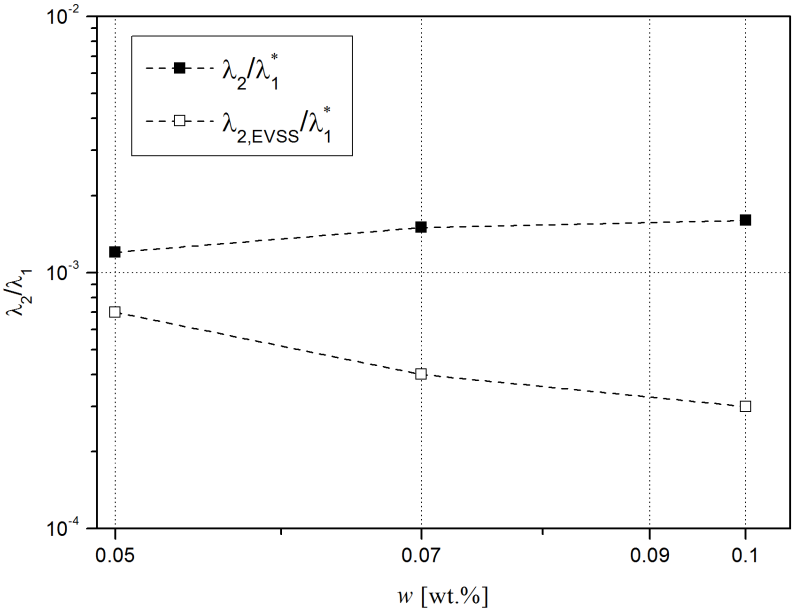

Figure 7.8: Values of λ_2/λ_1^* and $\lambda_{2,EVSS}/\lambda_1^*$ against polymer mass fraction for aqueous P2540 solutions.

The deformation retardation time λ_2 is determined from the measured pairs of (η_0, λ_2) or (λ_1, λ_2) (see table 7.4). Both pairs provide similar values of λ_2. Measured deformation retardation time λ_2 and calculated $\lambda_{2,EVSS}$ of the investigated aqueous P2540 solutions are presented in figure 7.7 and listed in table 7.5.

w [wt.%]	λ_2 [10^{-4} s]	$\lambda_{2,EVSS}$ [10^{-4} s]	λ_2/λ_1^*	$\lambda_{2,EVSS}/\lambda_1^*$
0.05	1.3	0.41	0.0012	0.0007
0.07	1.7	0.47	0.0015	0.0004
0.1	1.8	0.55	0.0016	0.0003

Table 7.5: Measured deformation retardation time λ_2 and calculated $\lambda_{2,EVSS}$ of the investigated aqueous P2540 solutions.

Figure 7.7 shows the measured λ_2 and calculated $\lambda_{2,EVSS}$ (3.36) against the Praestol 2540 mass fraction. Similar conclusions can be drawn as for the aqueous P2500 solutions. Again, the λ_2 obtained by the oscillating drop method is of the order of 10^{-4} s and increases monotonically with the polymer mass fraction w, while the values of the deformation retardation time obtained by the stress-splitting approach $\lambda_{2,EVSS}$ decrease with increasing polymer mass fraction. Contrary to the aqueous P2500 solutions (7.3(b)), there is no region of polymer mass fractions where agreement between λ_2 and $\lambda_{2,EVSS}$ could be observed. Also, for the rigid, rod-like polymer P2540, the values $\lambda_{2,EVSS}$ are always less than λ_2, in contrast to the flexible P2500 data, where for some range of polymer mass fractions the opposite was found.

Figure 7.8 shows the values λ_2/λ_1^* against the Praestol 2540 mass fraction. For the values of the deformation retardation time obtained from the oscillation experiments λ_2, the ratio λ_2/λ_1^* is nearly constant with a mean value of about $1.4 \cdot 10^{-3}$. For the calculated values of the deformation retardation time $\lambda_{2,EVSS}$ (3.36), the ratio $\lambda_{2,EVSS}/\lambda_1^*$ slowly decreases with increasing polymer mass fraction from about $7 \cdot 10^{-4}$ for the lowest polymer mass fraction to $3 \cdot 10^{-4}$ for the highest polymer mass fraction.

7.3 Validation of the experimental method

In order to validate the experimental method for measuring the deformation retardation time and to confirm the correctness of the measured values λ_2, the theoretical predictions of the linear theory are compared with the experimental results. Further comparison is made regarding the stress splitting approach.

As a test case, the 0.3 wt.% Praestol 2500 solution drop with an equilibrium radius of 0.9167 mm is considered. The material properties are listed in table 5.2. For this polymer solution, the corresponding value of the measured deformation retardation time is $\lambda_2 = 0.9 \cdot 10^{-4}$ s and, for comparison, the deformation retardation time obtained from the stress splitting approach is $\lambda_{2,EVSS} = 10.67 \cdot 10^{-4}$ s.
The calculated Rayleigh frequency (1.9) for $m = 2$ is $\alpha_{2,0} = 2\pi \cdot 139.1$ Hz, and the measured complex angular frequency for this drop is $\alpha_2^* = 36.24\ \mathrm{s}^{-1} + i2\pi \cdot 134.2$ Hz. Solving the characteristic equation (4.64) for the complex frequency by inserting the measured λ_2 and all the other material properties of the liquid, a discrete set of solutions is obtained, as shown in table 7.6. The correct solution is identified by comparison with either the measured complex frequency α_2^* or with the calculated Rayleigh frequency $\alpha_{2,0}$. In the present test case, the correct solution is $\alpha_2 = 36.31\ \mathrm{s}^{-1} + i2\pi \cdot 132.34$ Hz.

α_2
...
$22.57\ \mathrm{s}^{-1} + i2\pi \cdot 98.66$ Hz
$28.99\ \mathrm{s}^{-1} + i2\pi \cdot 115.53$ Hz
$36.31\ \mathrm{s}^{-1} + i2\pi \cdot 132.34$ Hz
$44.81\ \mathrm{s}^{-1} + i2\pi \cdot 149.15$ Hz
$54.27\ \mathrm{s}^{-1} + i2\pi \cdot 165.88$ Hz
$64.67\ \mathrm{s}^{-1} + i2\pi \cdot 182.58$ Hz

Table 7.6: A set of solutions α_2 of the characteristic equation for the 0.9167 mm 0.3 wt.% Praestol 2500 solution drop. The value $\lambda_2 = 0.9 \cdot 10^{-4}$ s was used in the calculations. The highlighted value indicates the correct solution.

By inserting the calculated $\lambda_{2,EVSS}$ into the characteristic equation (4.64) and solving it for the complex angular frequency, only one solution is obtained, namely $\alpha_{2,EVSS} = 6.19\ \mathrm{s}^{-1} + i2\pi \cdot 139.51$ Hz.
Comparison of the calculated α_2 and $\alpha_{2,EVSS}$ shows that both calculations yield similar oscillation frequencies, while the difference in the calculated damping rates is significant. Further, by comparing α_2 and $\alpha_{2,EVSS}$ to the measured value α_2^*, it is evident that α_2 matches the measured complex frequency perfectly, while $\alpha_{2,EVSS}$ does not.
Similar results are obtained for other aqueous polymer solutions studied. These observations confirm the correctness of the presented experimental method and cast doubt on the validity of the stress splitting approach.

Next, for the present test case, the calculated time evolution of the drop shape is compared to the experimental results. The time evolutions of the equatorial and polar radii of the drop are calculated by numerically integrating the velocity components $u_r(t)$ and $u_\theta(t)$, given by the equations (4.48) and (4.49), respectively. Due to the fact that the velocity component $u_\theta(t)$ is zero for $\theta = 0$ and $\theta = \pi/2$, the calculations were performed for $\theta = 0.05$ and $\theta = 0.995 \cdot \pi/2$ in order to observe the influence of both velocity components. The numerical integration was done with the computer software MATHEMATICA by using the fourth-order Runge-Kutta method.
The relevant parameters entering the numerical calculations, among those listed in table 5.2 for the corresponding polymer solution, are the calculated complex angular frequency α_2, the equilibrium radius and the initial oscillation amplitude ϵ_0.
It is important to note, however, that the initial oscillation amplitude and the equilibrium radius obtained experimentally have different values for the oscillations in the equatorial and polar directions, due to the oblate shape of the levitated drop. For this reason two cases are considered. For the first case, the equilibrium polar and equatorial radii of the oscillating drop and the corresponding initial oscillation amplitudes in the equatorial and polar directions were taken from the corresponding drop oscillation measurement. For the second case, the drop is considered spherical with the prescribed equilibrium radius a, and the oscillation amplitude set as $\epsilon_0 = 0.05 \cdot a$.
The results for these two cases are presented in figures 7.9 and 7.10.

The comparison between the calculated and the measured drop shapes as functions of time is presented in figure 7.9, where the exact initial positions

and the oscillation amplitudes for the calculations were taken from the experimental data. The results of the numerical calculations obtained with the deformation retardation time λ_2 from oscillation measurements show very good agreement with the experimental data. The especially good agreement in the first part of the oscillation is due to the fact that the initial values for the numerical calculations were obtained from the experimental data. For the later times, a phase shift can be observed, which is due to the difference between the calculated α_2 and the measured oscillation frequency α_2^*.

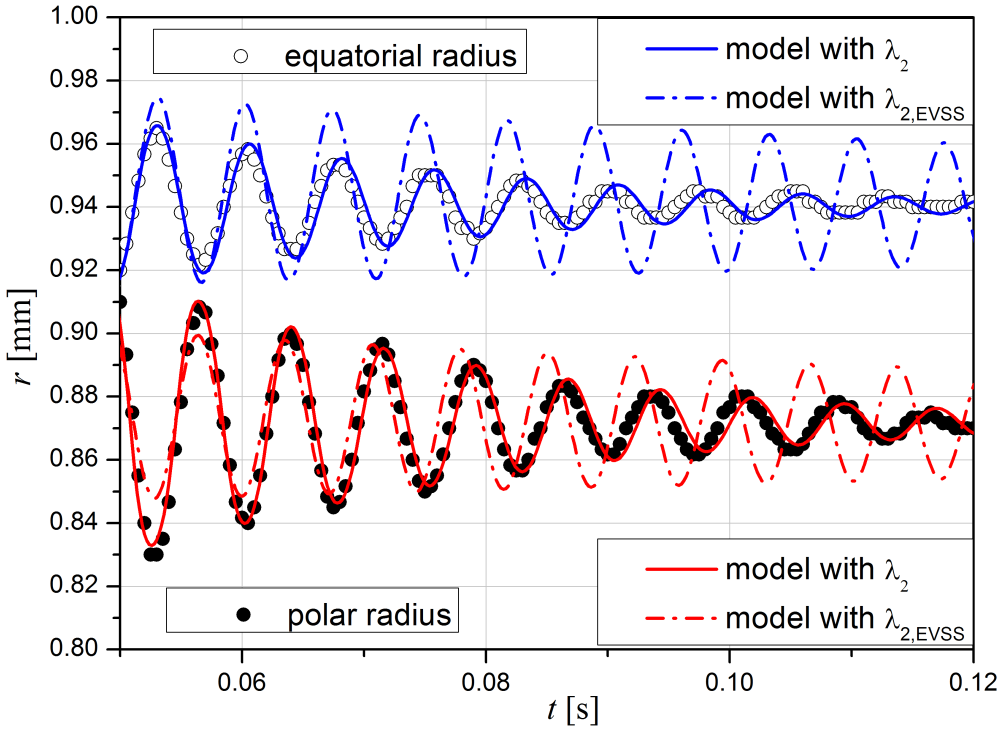

Figure 7.9: Temporal evolution of the polar and equatorial radii of the oscillating drop. Comparison between the measurements (symbols) and the numerical calculations performed using the measured λ_2 (solid line) and the calculated $\lambda_{2,EVSS}$ (dashed line). The exact initial positions and the oscillation amplitudes were obtained from the experimental data.

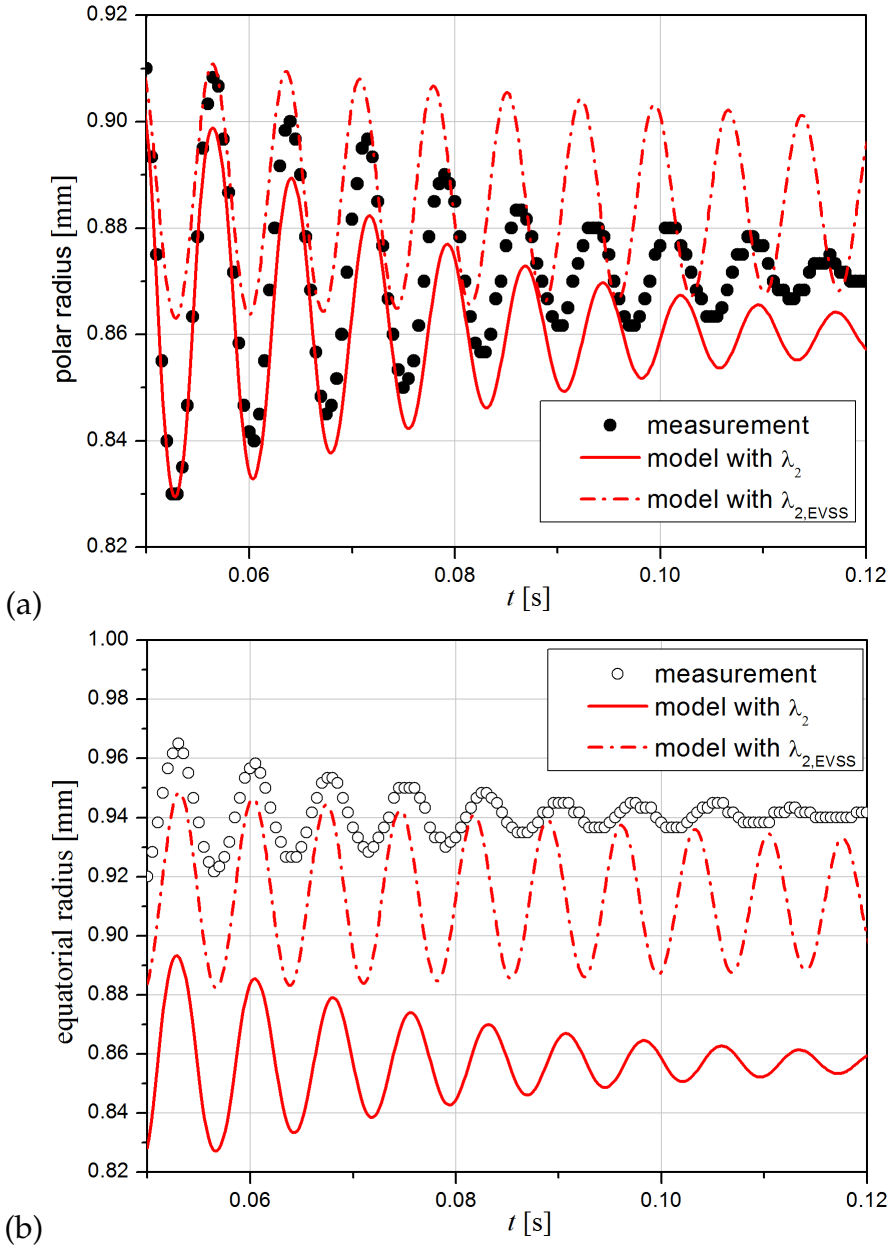

Figure 7.10: Temporal evolution of the (a) polar and (b) equatorial radii of the oscillating drop. Comparison between the measurements (symbols) and the numerical calculations performed using the measured λ_2 (solid line) and the calculated $\lambda_{2,EVSS}$ (dashed line). The calculations were performed for spherical drop shape with the equilibrium radius a and prescribed initial oscillation amplitude $\epsilon_0 = 0.05 \cdot a$.

On the contrary, the results of the numerical calculations obtained with the calculated deformation retardation time $\lambda_{2,EVSS}$ show a disagreement with the experimental data. The discrepancy is found both in the oscillation frequency and damping rate. This result is a direct consequence of the calculated complex angular frequency $\alpha_{2,EVSS}$, which does not match the measured frequency α_2^*.

These results for the depicted test case (figure 7.9) are a strong indication for the validity of the proposed experimental method for measuring the deformation retardation time.

Figure 7.10 shows the results of the numerical calculations where a spherical drop shape is assumed. Again, two numerical models, constructed with different deformation retardation times λ_2 and $\lambda_{2,EVSS}$, are considered. As expected, both models fail to correctly describe the experimental data, due to the assumption of the spherical drop shape.
Numerical calculation with the measured deformation retardation time λ_2 provides good results regarding the oscillation frequency and damping rate, due to the calculated α_2 which matches the measured frequency α_2^*. On the other hand, the calculated polar (figure 7.10(a)) and equatorial radii (figure 7.10(b)) differ from the measured ones, due to the incorrect initial conditions.
Numerical calculation with the calculated deformation retardation time $\lambda_{2,EVSS}$ does not match the experimental data for obvious reasons. The reasons are the incorrect angular frequency $\lambda_{2,EVSS}$ and the incorrect initial conditions.

7.4 Flow curves from the Jeffreys model

Finally, a comparison between the flow curves obtained by shear rheometry and the flow curves calculated from the Jeffreys model is presented. The flow curves $\eta(\dot{\gamma})$ from the rotational experiments are described using the Carreau model (see section 5.2.1).

The flow curves from the oscillation experiments (section 5.2.2) have to be calculated. The complex viscosity is introduced as

$$\eta^* = \eta' - i\eta'' = \int_0^\infty G(s)e^{-i\omega s}\mathrm{d}s \tag{7.1}$$

where ω is the oscillation angular frequency, $G(s)$ is the linear relaxation modulus, η' represents the viscous and η'' the elastic behaviour. The real and imaginary parts of the complex viscosity, η' and η'', are defined as [3, 16]

$$\eta'(\omega) = \frac{G''}{\omega} \quad \text{and} \quad \eta''(\omega) = \frac{G'}{\omega}. \tag{7.2}$$

where G' and G'' are the storage and loss moduli, respectively.

From the measured storage and loss moduli G' and G'', the linear relaxation modulus $G(t)$ is obtained using the software from ANTON PAAR. Further, with known $G(t)$, the complex viscosity $\eta^*(\omega)$ as a function of the oscillation frequency ω is determined.
The next step is to relate the shear rate to the imposed oscillation frequency. The oscillation experiments (see section 5.2.2) were performed using the cone-and-plate geometry (figure 5.3) at the constant deformation amplitude $\hat{\gamma} = 10\%$. The frequency-dependent mean shear rate is calculated as

$$\bar{\dot{\gamma}} = \hat{\gamma}\frac{2\omega}{\pi\tan(\beta_{cp})} \tag{7.3}$$

where $\beta_{cp} = 2^\circ$ is the cone angle [16]. Hence, by using equation (7.3), the complex dynamic viscosity $\eta^*(\bar{\dot{\gamma}})$ as a function of the (mean) shear rate can now be presented.

The time dependency of motion in the oscillation experiments (section 5.2.2) can be described by an exponential function of time (equation (5.3)). This

leads, together with the Jeffreys model (equation (3.49)), to an expression for the frequency-dependent dynamic viscosity of the Jeffreys model (equation (3.63)) given as

$$\eta_B^*(\omega) = \eta_0 \frac{1 - i\omega\lambda_2}{1 - i\omega\lambda_1} = \eta_0 \frac{1 + \lambda_1\lambda_2\omega^2 + i(\lambda_1 - \lambda_2)\omega}{1 + \omega^2\lambda_1^2} \tag{7.4}$$

where ω is the oscillation angular frequency. The real and imaginary parts of the complex viscosity η_B are given as

$$\eta_B' = \mathrm{Re}\left(\eta_B^*(\omega)\right) = \eta_0 \frac{1 + \lambda_1\lambda_2\omega^2}{1 + \omega^2\lambda_1^2} \tag{7.5}$$

and

$$\eta_B'' = \mathrm{Im}\left(\eta_B^*(\omega)\right) = \eta_0 \frac{(\lambda_1 - \lambda_2)\omega}{1 + \omega^2\lambda_1^2}. \tag{7.6}$$

By using relation (7.3), the complex viscosity η_B^* as a function of the (mean) shear rate can be presented.

Figure 7.11 presents the dynamic viscosity as a function of the shear rate for the 0.8 wt.% Praestol 2500 solution. The flow curves in figure 7.11 are obtained from the steady and oscillatory experiments, and calculated from the linear relaxation modulus $G(t)$ and from the Jeffreys model. For the comparison, only the real parts $\eta_B'(\dot{\gamma})$ and $\eta'(\dot{\gamma})$ of the complex dynamic viscosities are used.
Good agreement between the viscosities measured by the steady and oscillatory experiments can be observed. The agreement is weaker for higher shear rates.
The flow curve $\eta'(\dot{\gamma})$ calculated from the linear relaxation modulus $G(t)$ is in good agreement with $\eta(\dot{\gamma})$ from shear rheometry up to shear rates of approximately 10 s^{-1}. The first Newtonian plateau and the shear thinning behaviour are correctly described. For shear rates above 10 s^{-1}, the good agreement is lost and the discrepancy increases with the shear rate.
The flow curve $\eta_B'(\dot{\gamma})$ obtained from the Jeffreys model correctly reproduces the first Newtonian plateau, but fails to describe the viscosity at higher shear rates. Although the curve $\eta_B'(\dot{\gamma})$ shows the shear thinning behaviour, it fails to capture both the onset of shear thinning behaviour and the slope of

the curve. The explanation for this discrepancy may lie in the fact that $\eta'_B(\dot{\gamma})$ obtained from the Jeffreys model has only three free parameters, which is apparently not sufficient to correctly describe the behaviour of the measured flow curves.

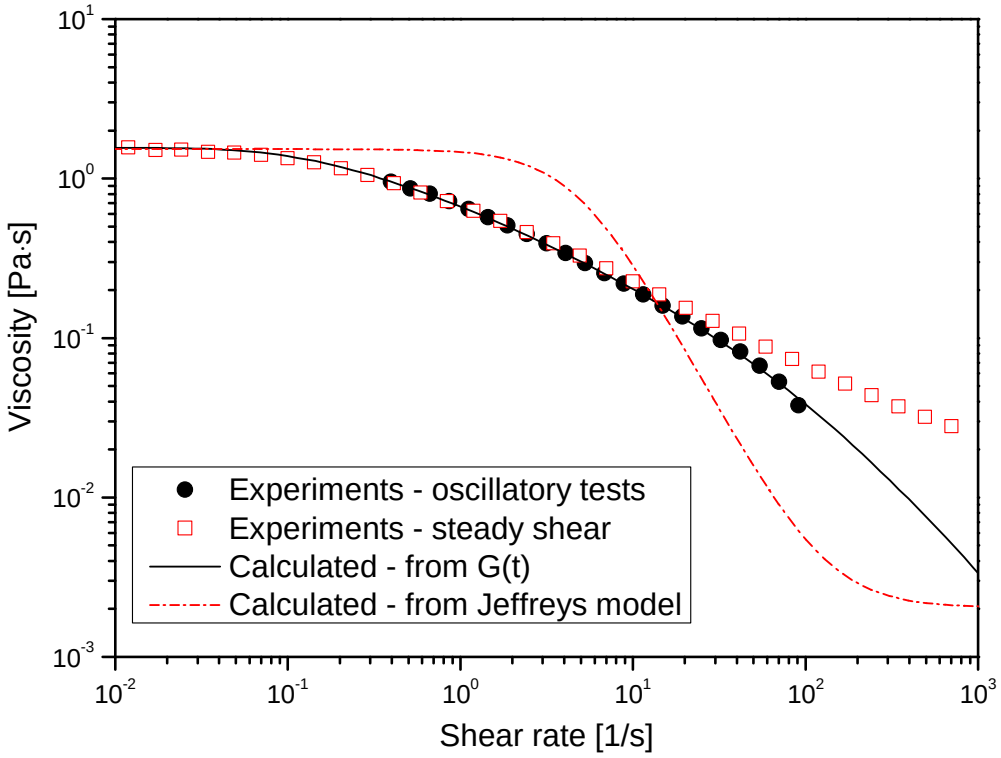

Figure 7.11: Flow curves of the 0.8 wt.% Praestol 2500 solution obtained by different methods.

In contrast, for example, the Carreau model given by the equation (5.2) has four free parameters, which accurately describe the measured flow curves. This leads to the conclusion that the reason for the discrepancy between $\eta'_B(\dot{\gamma})$ and $\eta(\dot{\gamma})$ at high shear rates lies in the linear Jeffreys model rather than in the accuracy of the measured λ_1 and λ_2. In the present work, however, the linear theory of small deformations and shear rates is considered, for which the linear Jeffreys model holds, as demonstrated in figure 7.11. Similar results and conclusions were obtained for all test liquids investigated.

8 Conclusions

In the present thesis, the dynamic behaviour of viscoelastic drops undergoing small-amplitude oscillations was investigated. The experimental investigations based on acoustic drop levitation were carried out with aqueous solutions of different polymers at varying polymer concentration. The main focus was on the measurements of the polymeric time scales appearing in the constitutive equation of linear viscoelasticity. The constitutive equation employed was the linearized Oldroyd-B model, also known as the Jeffreys model, which contains three parameters. Two of the parameters, namely the zero-shear-rate viscosity η_0 and the stress relaxation time λ_1, can be determined by well established rheological methods. For the third parameter, the deformation retardation time λ_2, no such method existed. The aim of the work was to develop a method for measuring the deformation retardation time and to provide a complete and consistent set of material properties relevant for the linear Oldroyd-B model.
Several reasons can be given to explain the lack of experimental methods for measuring the deformation retardation time. The first reason is the fact that, for the majority of theoretical works dealing with Oldroyd-B type models, the retardation time represents a free parameter. For example, in studies of viscoelastic fluid flow, the fluid behaviour for different values of λ_2 is examined, or in viscoelastic fluid flow simulations λ_2 is adjusted to achieve a faster convergence of numerical simulations. A second reason is the fact that alternative derivations of the Oldroyd-B model lead to an explicit expression for the deformation retardation time, relating it to other material properties. That means that λ_2 can be calculated, and there seemed to be no apparent need to develop a method to measure it.

In this study we use linear damped shape oscillations of drops for measuring the deformation retardation time and either the zero-shear viscosity or the stress relaxation time of viscoelastic polymeric drop liquids. The solution of

the linearized equations of change governing the drop shape oscillations yields the characteristic equation for the complex oscillation frequency of the drop which is used for determining the material properties. For a given drop, the oscillation frequency and the damping rate are measured in an experiment using acoustic drop levitation. Liquid material properties relevant for the oscillations, such as liquid density, surface tension and stress relaxation time, are measured by appropriate standard methods. The deformation retardation time and either the zero-shear viscosity or the stress relaxation time of the liquid are obtained as solutions of the characteristic equation of the oscillating drop. Values of the liquid dynamic viscosity are close to those from shear rheometry, and the values of the stress relaxation time are close to those from elongational experiments. They allow the correct solution of the characteristic equation to be identified from a manifold and support the correctness of the deformation retardation time determined. The uncertainty analysis shows, however, that the deformation retardation time λ_2 can be accurately measured even in cases where the correct solution *qa* of the characteristic equation cannot undoubtedly be identified.

The deformation retardation time measured with the proposed method is of the order of 10^{-4} s and increases with the polymer mass fraction. This result was obtained for both polymers examined. On the other hand, the deformation retardation time $\lambda_{2,EVSS}$ calculated by the equation obtained from the stress splitting approach decreases with increasing polymer mass fraction.
The value of λ_2/λ_1 is of the order of 10^{-3} and is nearly the same for all of the polymer solutions studied. This value strongly deviates from the value $\lambda_2/\lambda_1 = 0.1$ which is often used in viscoelastic fluid flow simulations.
For the aqueous Praestol 2500 solutions there exists a range of concentrations where the measured values of the deformation retardation time agree with the calculated ones, but this rather by coincidence. For the most diluted Praestol 2500 solution studied, the measured and calculated values of λ_2 strongly deviate from each other. The values of the zero-shear dynamic viscosity η_0 agree with the values from η_0^* shear rheometry to within ± 10 %, except in the case of high polymer mass fractions. For the 0.9 wt.% solution, the deviation is around 18 %, and in the case of the 1.0 wt.% solution the deviation is around 32 %. Similar, the values of the stress relaxation time λ_1 agree with the values λ_1^* from elongational rheometry to within ± 10 %,

except in the case of high polymer mass fractions. This disagreement could be due to experimental error, that is, the measurement error of the input parameters is too large.
In the case of aqueous solutions of rigid rod-like polymers Praestol 2540, only three polymer mass fractions were considered. The oscillating drop experiments provide similar results as in the case of solutions of flexible polymers. The results show good agreement between η_0 and η_0^*, and between λ_1 and λ_1^*. The measured and calculated values of λ_2, however, strongly deviate from each other.

The experimental method was validated by comparing the predictions of the underlying linear theory with the experimental results. The calculated complex angular frequency obtained using the measured deformation retardation time is in excellent agreement with the measured one. On the contrary, the calculation using the deformation retardation time $\lambda_{2,EVSS}$ from the stress splitting approach provides an undoubtedly false damping rate, while the calculated oscillation frequency is near the measured one.
Further, the calculated time evolution of the drop shape was compared to the experimental results. The numerical calculations obtained with the deformation retardation time λ_2 from the oscillation measurements show very good agreement with the experimental data, while the calculation with $\lambda_{2,EVSS}$ fails to correctly describe the time evolution of the drop shape.

The results of the deformation retardation time measurements, together with the presented sensitivity analysis and validity check, are a strong indication for the validity of the proposed experimental method for measuring the deformation retardation time and cast doubt on the validity of the stress splitting approach.

Bibliography

[1] J.G. Oldroyd. On the formulation of rheological equations of state. *Proc. R. Soc. Lond. Ser. A, Math. Phys. Sci.*, 200:523–541, 1950.

[2] J.G. Oldroyd. Non-newtonian effects in steady motion of some idealized elasto-viscous liquids. *Proc. R. Soc. Lond. Ser. A, Math. Phys. Sci.*, 245:278–297, 1958.

[3] R.B. Bird, R.C. Armstrong, and O. Hassager. *Dynamics of polymeric liquids*, volume 1. John Wiley & Sons New York, 1987.

[4] D.D. Joseph. *Fluid dynamics of viscoelastic liquids*. Springer, 1990.

[5] J.G. Oldroyd, D.J. Strawbridge, and B.A. Toms. A coaxial-cylinder elastoviscometer. *Proc. Phys. Soc. B*, 64:44–57, 1951.

[6] V.M. Entov and A.L. Yarin. The dynamics of thin liquid jets in air. *J. Fluid Mech.*, 140:91–111, 1984.

[7] V.M. Entov and A. L. Yarin. Influence of elastic stresses on the capillary breakup of jets of dilute polymer solutions. *Fluid Dyn. Res.*, 19:21–29, 1984.

[8] M. Stelter, G. Brenn, A.L. Yarin, R.P. Singh, and F. Durst. Validation and application of a novel elongational device for polymer solutions. *J. Rheology*, 44:595 – 616, 2000.

[9] M. Stelter, G. Brenn, A. Yarin, R. Singh, and Durst. Investigation of the elongational behavior of polymer solutions by means of an elongational rheometer. *J. Rheology*, 46:507–527, 2002.

[10] P.Y. Huang, H.H. Hu, and D.D. Joseph. Direct simulation of the sedimentation of elliptic particles in Oldroyd-B fluids. *J. Fluid Mech.*, 362:297–325, 1998.

[11] P.J. Oliveira. Alternative derivation of differential constitutive equations of the Oldroyd-B type. *J. Non-Newton. Fluid Mech.*, 160:40–46, 2009.

[12] L.J. Amoreira and P.J. Oliveira. Comparison of different formulations for the numerical calculations of unsteady incompressible viscoelastic fluid flow. *Adv. Appl. Mat. Mech.*, 2:483–502, 2010.

[13] G. Brenn and S. Teichtmeister. Linear shape oscillations and polymeric time scales of viscoelastic drops. *J. Fluid Mech.*, 733:504–527, 2013.

[14] G. Brenn and G. Plohl. The oscillating drop method for measuring the deformation retardation time of viscoelastic liquids. *J. Non-Newton. Fluid Mech.*, 223:88–97, 2015.

[15] N. Phan-Thien. *Understanding Viscoelasticity: An Introduction to Rheology*. Graduate Texts in Physics. Springer, 2. edition, 2012.

[16] T. G. Mezger. *The Rheology Handbook*. Vincentz Network Hanover, 3., rev.ed. edition, 2011.

[17] C. W. Macosko. *Rheology: Principles, Measurements, and Applications*. Wiley-VCH, New York, 1994.

[18] R.J. Poole. The Deborah and Weissenberg numbers. *Rheol. Bull.*, 53(2):32–39, 2012.

[19] V.M. Entov and J. Hinch. Effect of a spectrum of relaxation times on the capillary thinning of a filament of elastic liquid. *J. Non-Newtonian Fluid Mech.*, 72:31–53, 1997.

[20] J.G. Oldroyd. The motion of an elastico-viscous liquid contained between coaxial cylinders I. *Q. J. Mech. Appl. Math.*, 4(3):271–282, 1951.

[21] B.A. Toms and D.J. Strawbridge. Elastic and viscous properties of dilute solutions of polymethyl methacrylate in organic liquids. *Trans. Faraday Soc.*, 49:1225–1232, 1953.

[22] R.E. Chapman Jr., L.C. Klotz, D.S. Thompson, and B.H. Zimm. An instrument for measuring retardation times of desoxyribonucleic acid solutions. *Macromolecules*, 2:637–643, 1969.

[23] J. Kaschta and F. Schwarzl. Calculation of discrete retardation spectra from creep data I. Method. *Rheologica Acta*, 33:517–529, 1994.

[24] J. Kaschta and F. Schwarzl. Calculation of discrete retardation spectra from creep data II. Analysis of measured creep curves. *Rheologica Acta*, 33:530–541, 1994.

[25] Lord Rayleigh. On the capillary phenomena of jets. *Proc. R. Soc. London A*, 29:71–97, 1879.

[26] E. Becker, W.J. Hiller, and T.A. Kowalewski. Experimental and theoretical investigation of large amplitude oscillations of liquid droplets. *J.Fluid Mech.*, 231:189–210, 1991.

[27] H. Lamb. On the oscillations of a viscous spheroid. *Proc. London Math. Soc.*, 13:51–66, 1881.

[28] H. Lamb. *Hydrodynamics, 6th edn*. Cambridge University Press, 1932.

[29] C.A. Miller and L.E. Scriven. The oscillations of a fluid droplet immersed in another fluid. *J. Fluid Mech.*, 32:417–435, 1968.

[30] V. Vandaele, P. Lambert, and A. Delchambre. Non-contact handling in microassembly: Acoustical levitation. *Precis. Eng.*, 29(4):491–505, 2005.

[31] D. Zang, Y. Yu, Z. Chen, X. Li, H. Wu, and X. Geng. Acoustic levitation of liquid drops: Dynamics, manipulation and phase transitions. *Adv. Colloid. Interface Sci.*, 243:77 – 85, 2017.

[32] C.J. Hsu and R.E. Apfel. A technique for measuring interfacial tension by quadrupole oscillation of drops. *J. Colloid Interface Sci.*, 107:467–476, 1985.

[33] W.J. Hiller and T.A. Kowalewski. Surface tension measurements by the oscillating droplet method. *PCH PhysicoChemical Hydrodynamics*, 11:103–112, 1989.

[34] I. Egry, G. Lohöfer, I. Seyhan, S. Schneider, and B. Feuerbacher. Viscosity of the eutectic $Pd_{78}Cu_6Si_{16}$ measured by the oscillating drop technique in microgravity. *Appl. Phys. Letters*, 73:462–463, 1998.

[35] M. Perez, L. Salvo, M. Suéry, Y. Bréchet, and M. Papoular. Contactless viscosity measurement by oscillations of gas-levitated drops. *Phys. Rev. E*, 61:2669–2675, 2000.

[36] Y.R. Tian, R.G. Holt, and R.E. Apfel. Investigations of liquid surface rheology of surfactant solutions by droplet shape oscillations: Theory. *Phys. Fluids*, 7:2938–2949, 1995.

[37] R.E. Apfel, Y.R. Tian, J. Jankovsky, T. Shi, X. Chen, R.G. Holt, E. Trinh, A. Croonquist, K.C. Thornton, A. Sacco Jr., C. Coleman, F.W. Leslie, and D.H. Matthiesen. Free oscillations and surfactant studies of superdeformed drops in microgravity. *Phys. Rev. Letters*, 78:1912–1915, 1997.

[38] D. Mobius and R. Miller (eds.). *Novel methods to study interfacial layers*, chapter Kovalchuk, V.I. and Kragel, J. and Aksenenko, E.V. and Loglio, G. and Liggieri, L., Oscillating bubble and drop techniques, pages 485–516. Elsevier, Amsterdam, 2001.

[39] J. Kremer, A. Kilzer, and M. Petermann. Simultaneous measurement of surface tension and viscosity using freely decaying oscillations of acoustically levitated droplets. *Rev. Sci. Instrum.*, 89(1):015109, 2018.

[40] M. Lai, E. Krempl, and D. Ruben. *Introduction to Continuum Mechanics*. Elsevier, 2. edition, 2010.

[41] M.N.L Narasimhan. *Principles of Continuum Mechanics*. John Wiley & Sons New York, 1993.

[42] J.W. Rudnicki. *Fundamentals of continuum mechanics*. John Wiley & Sons, New York, 2015.

[43] R.G. Larson. *Constitutive equations for polymer melts and solutions*. Butterworths, Boston, 1988.

[44] R.G. Larson. *The Structure and Rheology of Complex Fluids*. Oxford University Press, New York, 1999.

[45] R.R. Huilgol and N. Phan-Thien. *Fluid Mechanics of Viscoelasticity*. Rheology Series, 6. Elsevier, 1997.

[46] T. Osswald and N. Rudolph. *Polymer Rheology: Fundamentals and Applications*. Carl Hanser Verlag, 2015.

[47] M. Doi and S.F. Edwards. *The Theory of Polymer Dynamics*. Oxford University Press, New York, 1986.

[48] C.D. Han. *Rheology and Processing of Polymeric Materials:Volume 1: Polymer Rheology*. Oxford University Press, New York, 2007.

[49] R.B. Bird, O. Hassager, and S. I. Abdel-Khalik. Co-rotational rheological models and the Goddard expansion. *AlChe J.*, 20:1041–1066, 1974.

[50] A.J. Giacomin, R.B. Bird, L. M. Johnson, and A.W. Mix. Large-amplitude oscillatory shear flow from the corotational Maxwell model. *J. Non-Newton. Fluid.*, 166:1081–1099, 2011.

[51] D.V. Boger. A highly elastic constant-viscosity fluid. *J. Non-Newton. Fluid Mech.*, 3:87–91, 1977/1978.

[52] R.B. Bird and J.M. Wiest. Constitutive equations for polymeric liquids. *Annu. Rev. Fluid Mech*, 27:169–193, 1995.

[53] H.W. Giesekus. *Phänomenologische Rheologie - Eine Einführung (Phenomenological Rheology - An Introduction, in German)*. Springer, Berlin, Heidelberg, 1994.

[54] R.B. Bird, R.C. Armstrong, and O. Hassager. *Dynamics of polymeric liquids*, volume 2. John Wiley & Sons New York, 1987.

[55] D. Rajagopalan, R.C. Armstrong, and R.A. Brown. Finite element methods for calculation of steady, viscoelastic flow using constitutive equations with a Newtonian viscosity. *J. Non-Newton. Fluid.*, 36:159–199, 1990.

[56] J. Sun, N. Phan-Thien, and R.I. Tanner. An adaptive viscoelastic stress splitting scheme and its applications: AVSS/SI and AVSS/SUPG. *J. Non-Newton. Fluid.*, 65:76–91, 1996.

[57] M.G.N. Perera and K. Walters. Long-range memory effects in flows involving abrupt changes in geometry: Part I: flows associated with i-shaped and t-shaped geometries. *J. Non-Newton. Fluid Mech.*, 2(1):49–81, 1977.

[58] J.D. Ferry. *Viscoelastic Properties of Polymers*. John Wiley & Sons, New York, 1980.

[59] H.A. Barnes, J.F. Hutton, and K. K. Walters. *An Introduction to Rheology*. Elsevier, Amsterdam, 1989.

[60] G. Brenn. *Analytical Solutions for Transport Processes*. Springer, Berlin, Heidelberg, 2016.

[61] D. B. Khismatullin and A. Nadim. Shape oscillations of a viscoelastic drop. *Phys. Rev. E*, 63:061508, 2001.

[62] S. Chandrasekhar. The oscillations of a viscous liquid globe. *Proc. London Math. Soc.*, 9:141–149, 1959.

[63] A. Prosperetti. Free oscillations of drops and bubbles: the initial-value problem. *J. Fluid Mech.*, 100:333–347, 1980.

[64] L. Yang, B.K. Kazmierski, S.D. Hoath, S. Jung, W.-K. Hsiao, Y. Wang, A. Berson, O. Harlen, N. Kapur, and C.D. Bain. Determination of dynamic surface tension and viscosity of non-Newtonian fluids from drop oscillations. *Phys. Fluids*, 26:113103, 2014.

[65] S. Tomotika. On the instability of a cylindrical thread of a viscous liquid surrounded by another viscous fluid. *Proc. R. Soc. London A*, 150:322–337, 1935.

[66] M. Nikkhah-Bahrami and R. Oftadeh. An effective iterative method for computing real and complex roots of systems of nonlinear equations. *Appl. Math. Comput.*, 215:1813–1820, 2009.

[67] R. Oftadeh, M. Nikkhah-Bahrami, and A. Najafi. A novel cubically convergent iterative method for computing complex roots of nonlinear equations. *Appl. Math. Comput.*, 217:2608–2618, 2010.

[68] W. Nagashiro and T. Tsunoda. Degradation of polyacrylamide molecules in aqueous solutions by high-speed stirring. *J. Appl. Polym. Sci.*, 21:1149 – 1153, 1977.

[69] L.H.O. Hellström, M.A. Samaha, K.M. Wang, A.J. Smits, and M. Hultmark. Errors in parallel-plate and cone-plate rheometer measurements due to sample underfill. *Meas. Sci. Technol.*, 26:015301, 2015.

[70] M. R. Nobile and F. Cocchini. A generalized relation between MMD and relaxation time spectrum. *Rheol. Acta*, 47:509–519, 2008.

[71] C. Friedrich, R. J. Loy, and R. S. Anderssen. Relaxation time spectrum molecular weight distribution relationships. *Rheol. Acta*, 48:151–162, 2009.

[72] C. Pilz and G. Brenn. On the critical bubble volume at the rise velocity jump discontinuity in viscoelastic liquids. *J. Non-Newtonian Fluid Mech.*, 145:124–138, 2007.

[73] J.D. Berry, M.J. Neeson, R.R. Dagastine, D.Y.C. Chan, and R.F Tabor. Measurement of surface and interfacial tension using pendant drop tensiometry. *J. Colloid Interface Sci.*, 452:226–237, 2015.

[74] G. L. Gaines Jr. Surface and interfacial tension of polymer liquids –a review. *Polym. Eng. Sci.*, 12, 1972.

[75] R. Miller and L. Liggieri, editors. *Bubble and Drop Interfaces*. Progress in Colloid and Interface Science, Vol. 2. Brill, Leiden, 2011.

[76] E. Yakhshi-Tafti, R. Kumar, and H.J. Cho. Measurement of surface interfacial tension as a function of temperature using pendant drop images. *Int. J. Optomechatroni.*, 5:393–403, 2011.

[77] A.L. Yarin, G. Brenn, O. Kastner, D. Rensink, and C. Tropea. Evaporation of acoustically levitated droplets. *J. Fluid Mech.*, 399:151–204, 1999.

[78] M. Kreimer, I. Aigner, S. Sacher, M. Krumme, T. Mannschott, P. van der Wel, A. Kaptein, H. Schroettner, G. Brenn, and J.G. Khinast. Mechanical strength of microspheres produced by drying of acoustically levitated suspension droplets. *Powder Technol.*, 325:247–260, 2018.

[79] tec5 AG. Ultrasonic levitator - User manual, 2009 (accessed February 3, 2018). URL:`https://www.tec5.com`.

[80] E.H. Trinh, P.L. Marston, and J.L. Robey. Acoustic measurement of the surface tension of levitated drops. *J. Colloid Interface Sci.*, 124:453 – 474, 1988.

[81] E. Trinh, A. Zwern, and T.G. Wang. An experimental study of small-amplitude drop oscillations in immiscible liquid systems. *J. Fluid Mech.*, 115:453 – 474, 1982.